**Title**

Proteomic Analysis and Engineering of Erythrocyte-Derived Optical Particles for Biomedical Application

**Permalink**

https://escholarship.org/uc/item/7kc2f02v

**Author**

Lee, Chi-Hua

**Publication Date**

2022

**Supplemental Material**

https://escholarship.org/uc/item/7kc2f02v#supplemental

UNIVERSITY OF CALIFORNIA
RIVERSIDE


Proteomic Analysis and Engineering of Erythrocyte-Derived Optical Particles for
Biomedical Application


A Dissertation submitted in partial satisfaction
of the requirements for the degree of


Doctor of Philosophy

in

Biochemistry and Molecular Biology

by

Chi-Hua Lee


December 2022


Dissertation  Committee:
        Dr. Bahman Anvari, Chairperson
        Dr. Seán O'Leary
        Dr. Joshua Morgan

The Dissertation of Chi-Hua Lee is approved:

_____

_____

_____

Committee Chairperson

University of California, Riverside

# ACKNOWLEDGEMENTS

Lastly, I would like to my parents, Hwa-Teng and Chih-Fong, for their unconditional love and support; my husband, George, for his devotion, patience and belief in me; my siblings, Chi-Ko and Chi-Ting, for always being by my side. Without having such great family, I would not have made it this far.

ABSTRACT OF THE DISSERTATION


Proteomic Analysis and Engineering of Erythrocyte-Derived Optical Particles for
Biomedical Application

by


Chi-Hua Lee

Doctor of Philosophy, Graduate Program in Biochemistry and Molecular Biology
University of California, Riverside, December 2022
Dr. Bahman Anvari, Chairperson




Erythrocyte-derived platforms are garnering increasing attention as delivery vehicles due
to their advantages in biocompatibility, low immunogenicity, tunable size and naturally
long circulation. Erythrocyte carriers can be used to deliver various diagnostic and
therapeutic cargos for clinical application such as tumor or vascular imaging. We have
developed erythrocyte-derived optical particles loaded with the near-infrared (NIR)
chromophore, such as FDA-approved indocyanine green (ICG). We refer to these
constructs as <u>N</u>IR <u>e</u>rythrocyte-derived <u>t</u>ransducers (NETs). They can generate heat, emit
fluorescence, and mediate the production of reactive oxygen species(ROS) once being
photoexcited by NIR light.

We analyzed the proteomes of micro- and nano-sized erythrocyte-derived particles
as compared to their native erythrocytes. Next, we demonstrated that enriching membrane
cholesterol on NETs reduces phosphatidylserine (PS) exposure, which serves as a signal

for phagocytic removal once PS externalized to outer leaflet of plasma membrane, and thus prolong their longevity in vivo to up to 24hr post-injection. Further, we investigated the effectiveness of enriching the membrane cholesterol content and folate-functionalizing of nano-sized NETs (nNETs) on biodistribution of these particles in organs and tumors of immunodeficient mice implanted with intraperitoneal ovarian cancer cells. Our results suggest that cholesterol enrichment of nNETs in combination with folate functionalization can result in greater accumulation of particles in tumors, providing a potential approach for enhanced NIR imaging of tumors.

We also evaluated the capability of micro-sized NETs (μNETs) in mediating photothermal destruction of cutaneous vasculature in the rabbit earlobe as a model system for port wine stain (PWS). We successfully demonstrated that pulsed 755 nm laser irradiation at reduced radiant exposure in conjunction with administration of these μNETs results in a complete blood flow cessation in rabbit earlobe vasculature, indicating a potentially promising method to treat PWS.

Finally, toward developing a novel carrier with dual-modality that can be used in both NIR and magnetic resonance (MR) imaging of tumors, we demonstrated the engineering and characterization of erythrocyte-derived particles that can be dually loaded with NIR brominated cyanine dye and gadobenate dimeglumine (Gd) agent.

# Table of Contents

**Chapter 4:** Cholesterol-Enriched and Folate-Functionalized Erythrocyte-Derived Optical

Nanoparticles for NIR Fluorescence Imaging of Intraperitoneal Ovarian Tumors in Mice

**Chapter 5:** Erythrocyte-Derived Optical Microparticles for NIR Photocoagulation of

Cutaneous Vasculature

**Chapter 6:** Optical Characteristics of Dual MRI and NIR dyes loaded Erythrocyte-

derived Nanoparticles

# List of Figures

# List of Tables

**Chapter 1: Introduction**

Erythrocytes (red blood cells; RBCs)-derived delivery platforms are gaining in popularity to shuttle various payloads such as imaging or therapeutic agent due to their advantages of biocompatibility, low immunogenicity and naturally long systemic circulation[1-3]. As such, they have been extensively utilized in a number of different biomedical applications including diagnosis[4-5], treatment of disease[5-6], or as vehicle of vaccine[7-8]. In particular, our lab has engineered erythrocyte-derived constructs that are doped with FDA-approved near-infrared (NIR) chromophore, indocyanine green (ICG)[9]. We refer to these constructs as NIR erythrocyte-derived transducers (NETs) since they are capable of transducing the absorbed light to emit fluorescence or generate heat upon photoactivated by NIR excitation.

One key feature of NETs is their tunable size ranging from micro- to nano-scale (μNETs and nNETs, respectively) which can be useful in various applications. For instance, μNETs may be applied in photothermal therapy of vascular malformation such as port wine stain (PWS)[10] while nNETs have potential in cancer treatment[6, 11-12]. While we have previously proven the presence of CD47, a self-protective marker on the surface of RBCs that inhibits phagocytosis[13], on both μNETs and nNETs[14] and studied the membrane mechanical properties of micro-sized erythrocyte ghosts(EGs) and μNETs[15], we have not yet looked further into the protein compositions of these constructs. As some key transmembrane and cytoskeletal proteins, responsible for immune-modulatory effects and mechanical integrity of the particles, are relevance to the biodistribution and pharmacokinetics of these particles[16]. In chapter 2, we examined the proteomes of both

μEGs[+ICG] and nEGs[+ICG] and highlighted the importance of methods in fabricating erythrocyte-derived particles with appropriate proteomes.

In chapter 3, with an aim to develop an effective RBC-derived carriers with ideal longevity in circulation, we demonstrated that enriching the membrane cholesterol content of the particles can effectively decrease the outward display of phosphatidylserine(PS), one of the major membrane phospholipids which is normally confined to inner leaflet of RBC membrane. Externalization of PS occurs during the fabrication process which will then serve as a recognition signal for phagocytic removal of the particles with surface-exposed PS[17]. Our in vitro result first showed that cholesterol enriched μNETs(C[+]-μNETs) had significantly lower uptake by murine macrophages as compared to μNETs. We then verified via in vivo study that C[+]-μNETs had longer circulation to up to 24 hr post-injection as compared to μNETs. These results indicate the membrane cholesterol enrichment as an effective method to reduce PS exposure and can prolong their circulation in blood. Further, in fourth chapter, we demonstrated the successful functionalization of nNETs with folate and enrichment with membrane cholesterol (F-C[+]nNETs) which results in significantly greater accumulation of the particles in tumors than other particles. These findings imply that cholesterol enrichment of nNETs combined with folate targeting can improve the tumor accumulation of particles, offering a potentially promising capability for enhance NIR imaging of tumors.

Next, in chapter 5, we evaluated the capability of NETs in mediating photothermal destruction of cutaneous vasculature in the rabbit earlobe as a model system for PWS. Particularly, we used laser speckle contrast imaging to characterize the blood flow

dynamics immediately and up to 24 hrs following laser irradiation, and histological analysis to evaluate the thermal damages. We showed that laser irradiation in conjunction with NETs injection results in reduced blood perfusion immediately after irradiation and a complete halt in blood flow one day later. The histological analysis also showed the photothermal damages on blood vessel. This indicates a promising method for treatment of PWS.

Finally, we expand the use of RBC-derived carriers in chapter 6. We investigated whether NIR and magnetic resonance imaging (MRI) dyes can be dually loaded into human RBC-derived nanoparticles so that they can be utilized in visualizing tumors via MR and NIR imaging. As the use of NIR lights provides relatively deeper penetration and high-resolution in biomedical optical imaging than visible light[18]. MRI has be extensively used in clinical applications for its great soft tissue contrast between normal tissues and lesions[19-20]. Combining the strengths of both, this dual-modal nanoparticles may achieve the purpose of developing an great tool in obtaining the non-invasive image with high-contrast intrinsic properties of tumor lesions in clinical applications. Thus, we demonstrated the successful fabrication of RBC-derived nanoparticles containing both NIR (BrCy) and MRI (Gadobenate dimeglumine; Gd) dyes and investigated the optical characteristics of the particles. While we suggest that this dual-modal nanoparticles may have potential, more studies are needed to further expand their use in clinical applications.

**Chapter 2: Proteomes of Micro- and Nano-Sized Carriers Engineered from Red Blood Cells**

**2.1 Abstract**

Erythrocyte-derived delivery systems offer a potential platform for delivery of various biomedical cargos. Although the importance of specific proteins in relation to biodistribution and pharmacokinetics of these particles has been recognized, it has yet to be explored whether some of the key transmembrane and cytoskeletal proteins, responsible for immune-modulatory effects and mechanical integrity of the particles are retained. Herein, using sodium dodecyl sulfate–polyacrylamide gel electrophoresis, and quantitative Tandem Mass Tag mass spectrometry in conjunction with bioinformatics analysis, we have examined the proteomes of micro- and nano-sized erythrocyte ghosts doped with the near-infrared agent, indocyanine green, and compared them with those of the native red blood cells (RBCs). We have identified a total of 884 proteins in each set of RBCs, micro-sized, and nano-sized particles, of which 8 and 45 proteins were found to be expressed at significantly different abundances when comparing the micro-sized particles vs RBCs, and nano-sized particles vs RBCs, respectively. Most of these proteins are involved in enzymatic activity. Some of the proteins with altered relative abundances in the nano-sized particles, such as equilibrative nucleoside transporter 1 and urea transporter 1, serve as transporters. Additionally, we found greater differences in the relative abundances of some of the mechano-modulatory proteins such as band 3 and protein 4.2, and immune-modulatory proteins such as CD47, CD55, and CD44 in the nano-sized particles as compared to RBCs. Our results indicate that the mechanical extrusion process used in

fabrication of the nano-sized particles induces substantial effects on their proteomics. Our findings suggest the importance of the engineering methods in fabrication of erythrocyte-based delivery systems with appropriate proteomics for ultimate clinical applications.

## 2.2 Introduction

Cell-based platforms have gained increasing attention for the delivery of various therapeutic, diagnostic, and imaging cargos. In particular, red blood cells (RBCs) are promising candidates due to their expected biocompatibility and non-toxicity, especially if derived from autologous blood[21-25]. An important issue related to the effectiveness of RBC-derived delivery vehicles in clinical application is their circulation time. To accumulate at sufficient therapeutic or diagnostic quantities within the target site, a sufficiently long circulation time is necessary before the particles are removed by the reticuloendothelial system.

One of the key determinants in the longevity of RBC-derived carriers within circulation is the presence of specific proteins on the surface of their membranes that interact with the immune cells. For example, transmembrane glycoprotein CD47 prevents RBCs from being phagocytosed by macrophages[13], and the decay-accelerating factor (CD55) and CD59 prevent the complement system from activating and forming membrane-attack complexes (MACs) against RBCs[26]. The presence of these cell surface proteins (among others) is needed for prolonging the circulation time of RBC-derived vehicles.

Another important factor in determining the circulation time of RBC-derived carriers is their mechanical deformability. Healthy RBCs repeatedly squeeze through narrow capillaries that have diameters similar to those of RBCs ($\sim 8\ \mu$m), and through the

endothelial slits of spleen (~ 200-400 nm)[27], the filtration organ involved in sequestering and disassembly of senescent RBCs. In addition to the mechanical properties of membrane bilayer itself, the deformability of RBCs is attributed to the proteins that link the membrane to the cytoskeleton as well as a network of cytoskeletal proteins[28-30].

Towards development of RBC-derived carriers for clinical use, it is important to gain a better understanding of their proteome, particularly those proteins involved in modulating the immune response and the mechanical characteristics of the carriers as they are related to the circulation time of the particles. While the proteomes of RBCs have been extensively investigated[31-32], this is the first evaluation of the proteome of RBC-derived carriers for their use as delivery vehicles. In particular, we have used sodium dodecyl sulphate-polyacrylamide gel electrophoresis (SDS-PAGE), and quantitative tandem mass tag (TMT)-based mass spectrometry (MS) in combination with bioinformatics analysis to characterize the proteomes of micro- and nano-sized RBC-derived particles. These particles are doped with the FDA-approved near-infrared chromophore, indocyanine green (ICG), which has a long history in clinical applications ranging from ophthalmic angiography[33-34] to tumor imaging[35-37] and laser therapy[38-39]. The nano-sized RBC-carriers have relevance to tumor optical imaging and laser-based therapeutics[6, 11, 40-44], while the micro-sized RBC-derived carriers may be useful for laser treatment of cutaneous hypervascular lesions such as port wine stains[10, 45].

Herein, we demonstrate that the protein composition of micro-sized erythrocyte ghosts (EGs) doped with ICG ($\mu$EGs[+]ICG) was generally similar to that of RBCs, but there were still 8 proteins with significantly different relative abundance in $\mu$EGs[+]ICG as

compared to RBCs. The proteomic profiles of nano-sized EGs (nEGs) doped with ICG (nEGs+ICG) showed lower relative abundance levels of some structural proteins ($\alpha$-/$\beta$-Adducin, dematin) and additional differences in their protein compositions, including immunomodulatory surface proteins like CD47, CD44, and complement C4B as compared to those of RBCs and $\mu$EGs+ICG. Our findings highlight the importance of methods in engineering RBC-derived carrier systems with appropriate proteomes for clinical translation.

## 2.3 Material and Methods

### 2.3.1 Fabrication Procedures

RBCs were isolated from human whole blood (Innovative Research Inc., Novi, MI) via centrifugation (1600g for 10 min at 4°C). The supernatant containing the plasma and buffy coat were removed and the erythrocyte pellets were washed twice with ~ 320 mOsm phosphate buffered saline (PBS) (referred to as 1×PBS, pH=8) (Fisher Scientific, Hampton, NH). The supernatant was discarded after each wash. The washed erythrocytes were then subjected to hypotonic treatment in 0.25×PBS (~ 80 mOsm, pH=8) for 30 min followed by centrifugation (20,000g for 20 min at 4°C). The supernatant containing hemoglobin was discarded, and the hypotonic treatment was repeated until a white pellet containing the micro-sized erythrocyte ghosts ($\mu$EGs) was obtained. The $\mu$EGs were then resuspended in 1×PBS.

To form nEGs, 1 ml of $\mu$EGs was first diluted 10-fold in 1×PBS and then extruded sequentially through 800-, 400-, and 200-nm diameter polyester porous membranes (Sterlitech Corp., Kent, WA) using a 10 ml LIPEX® extruder (TRANSFERRA

Nanosciences Inc., Burnaby, B.C.). µEGs were passed through each membrane size at least three times. The pellet containing the nEGs was isolated by centrifugation (100,000g for 1 hour at 4°C), and then resuspended in the original 1 ml of 1×PBS.

To load ICG (MP Biomedicals, Santa Ana, CA) into µEGs and nEGs, particles were incubated in a hypotonic solution made of 1:1:1 volume ratio of particles, Sørenson's phosphate buffer ($Na_2HPO_4$ / $NaH_2PO_4$, 140 mOsm, pH = 8), and ICG solution for 30 min at 4 °C in the dark. Concentration of ICG in the loading buffer solution was 25 µM. This process results in formation of µEGs and nEGs doped with ICG, which we refer to as µEGs[+ICG] and nEGs[+ICG], respectively. To obtain the µEGs[+ICG] and nEGs[+ICG] pellets, 3 ml of suspensions were then centrifuged and washed twice with 1×PBS (20,000g for 20 min at 4°C, and 100,000g for 1 hour at 4°C for µEGs[+ICG] and nEGs[+ICG], respectively). The resulting pellets of µEGs[+ICG] and nEGs[+ICG] were then resuspended in their original 1 ml of 1×PBS to restore tonicity. The absorption spectra of the particles were obtained using a spectrophotometer (Jasco-V670, JASCO, Easton, MD, USA).

### 2.3.2 Size Profiling of Particles

Dynamic light scattering (DLS) (Zetasizer Nanoseries, NanoZS90, Malvern Instruments Ltd, Westborough, MA) was used to estimate the hydrodynamic diameters of the particles suspended in 1×PBS in a polystyrene cuvette with a 1 cm pathlength. Three measurements were collected for each sample. The mean peak diameter ± standard deviation (SD), based on lognormal fits to the DLS-based measurements, were 4,149±200 nm and 140.87±0.848 nm for µEGs[+ICG] and nEGs[+ICG], respectively.

We also used the Zetasizer to quantify the zeta potentials of the particles in 1×PBS. The mean±SD values of zeta potentials for µEGs$^{+ICG}$ and nEGs$^{+ICG}$ were -13.02 ± 0.85 mV and -14.4 ± 0.88 mV, respectively.

### 2.3.3 SDS-PAGE

Samples, consisting of RBCs (control), µEGs$^{+ICG}$ or nEGs$^{+ICG}$, were thoroughly mixed in Laemmli buffer (6X; 375mM Tris-HCl, 6% SDS, 4.8% Glycerol, 9% 2-mercaptoethanol, 0.03% Bromophenol blue) followed by heating at 95 °C for 5 minutes to denature the proteins. To quantify the total protein amount in each sample, the Bradford assay (Thermo-Fisher Scientific Inc., Rockford) in conjunction with standard curves was used. The peak absorption of the Bradford reagent (Coomassie blue G-250) changes from 470 nm to 595 nm when it binds to proteins, which is then measured spectroscopically. After binding, we compared the 595 nm absorbance value to a standard curve that relates the absorbance values to various concentrations of protein, and quantified the amount of the protein in each sample.

We then loaded the samples into a precast, gradient 12% polyacrylamide gel and electrophoretically separated the protein at 100V for 2 hours. The gel was fixed and stained in staining buffer (0.25 g Coomassie blue R-250, 40 mL methanol, 50 mL dH$_2$O, 10 mL acetic acid) overnight to visualize the protein migration. The stained gel was then washed in de-staining buffer (40% methanol, 10% acetic acid in dH2O) overnight to clear the background dye. Visualization of the gel band was obtained using the BioSpectrum Imaging System (UVP system, Anaytik Jena, Upland, CA). To estimate the molecular weight (MW) of unknown proteins, the gel image was then analyzed to determine the

relative migration distance ($R_f$ value) of the protein standard marker and the unknown protein:

$$Rf = \frac{\text{Migration distance of the band}}{\text{Migration distance of the dye at front}}. \tag{1}$$

Finally, a plot of the logarithm of the MW of the protein standards against their $R_f$ values was constructed as the standard curve to determine the MW of various unknown proteins[46-47]. The protein identity was predicted by comparing the estimated MWs to those of known proteins in literature[31, 48-49].

**2.3.4 TMT-MS Analysis**

**Sample Preparation.** Samples were prepared in triplicates. Following the manufacturer's instructions (TMT Mass Tag Labeling Kit, Thermo Fisher Scientific), each sample type was lysed to isolate the protein extracts, which were then reduced, alkylated and digested to obtain the peptides. The TMT reagents were added to label the peptides from each sample. All samples were then mixed together, followed by fractionation prior to MS analysis. Specifically, cell suspensions were first lysed in lysis buffer (0.25% sodium deoxycholate, 1% NP-40, 50mM triethylammonium bicarbonate (TEAB) (Millipore Sigma), 1mM phenylmethylsulfonyl fluoride) on ice for 1 hr, and then adjusted to 500 µL in 50 mM TEAB. To minimize protein degradation and reduce the activity of proteases and the contaminants in each sample, acetone precipitations prior to digestion and labeling process was performed. The proteins derived from lysed cells of each sample were precipitated in equal volumes of trichloroacetic acid and incubated on ice for 1 hr. The supernatant was discarded, and the pellet was rinsed twice with 500 µL of cold acetone which was then removed using a vacuum concentrator (SpeedVac, Thermo Fisher

Scientific). The resulting dried pellet was resuspended in 50 µL of 50 mM TEAB and subsequently reduced by incubating it with 1 µL of 500 mM Tris (2-carboxyethyl) phosphine (Thermo Fisher Scientific, Rockford, IL) at 37 °C for 1 hr. Each sample was then added to 3 µL of 500 mM iodoacetamide (Millipore Sigma) and incubated in the dark at room temperature for 1 hr.

Next, the digestion of the proteins was performed per manufacturer's instructions (Thermo Fisher Scientific). Specifically, proteins of each sample were incubated with 500 µL of 50 mM TEAB and 10 µL (2 µg) of trypsin/lysC mix (Promega, Madison, WI) at 37 °C overnight (16 hrs). After digestion, the concentrations of peptides from each sample were measured using a colorimetric assay (Thermo Fisher Scientific). The assay was performed following the manufacturer's instructions using a 96-well microplate which involves protein peptide-copper chelation and detection of the reduced copper. Briefly, the amide backbone of peptides in the sample causes the copper to be reduced under alkaline conditions to form a bright red complex, which can be detected at 480 nm. The peptide concentration of each sample was determined by comparing the absorbance at 480 nm to that of a peptide standard curve.

Lastly, TMT labeling was performed according to manufacturer's instruction (10-plex Tandem Mass Tag labeling, Thermo Fisher Scientific). From each sample, 50 µg was mixed with TMT Label Reagent using a 1:1 mass ratio of reagent to peptide and incubated at room temperature for 1 hr, followed by quenching with 8 µL of 5% hydroxylamine for 15 mins. The labelled aliquots were combined into one sample, and then dried in a vacuum concentrator in preparation for high-pH fractions. The Pierce high-pH fraction kit (Thermo

11

Fisher Scientific) was used to separate the peptides by hydrophobicity to increase the number of proteins from the complex sample identified by liquid chromatography-mass spectrometry (LC-MS) analysis.

**LC-MS Analysis.** Liquid chromatography was performed on an EASY-nLC1200 liquid chromatography system (Thermo Fisher Scientific) in single-pump trapping mode with a PepMap RSLC C18 EASY-spray column (2 μm, 100Å, 75 μm × 25 cm) and a Pepmap C18 trap column (3 μm, 100 Å, 75 μm × 20 mm). Samples were separated at 300 nL/min with a 260 min linear gradient (3-85% solvent containing 80% acetonitrile with 0.1% formic acid) and data were acquired on an Orbitrap Fusion mass spectrometer (Thermo Fisher Scientific) in data-dependent mode. A full scan was conducted using 60k resolution in the Orbitrap in positive mode. Precursors for mass spectrometry 2 (MS2) were filtered by monoisotopic peak determination for peptides. Intensity threshold was set to $5.0 \times 10^3$, charge states 2-7 were selected, and dynamic exclusion was set to 60 seconds after one analysis with a mass tolerance of 10 ppm. Collisionally-induced dissociation spectra were collected in ion trap MS2 at 35% energy and isolation window 1.6 m/z. Synchronous Precursor Selection MS3 was utilized for TMT ratio determination at higher-energy C-trap dissociation (HCD) energy. The sequence of steps for TMT analysis are shown in Figure 2.1.

**Bioinformatics and Data Analysis.** All data obtained were searched individually in Proteome Discover 2.2 (Thermo Fisher Scientific) against the universal protein resource (UniProt) FASTA database for Homo sapiens. The precursor mass tolerance was set to 10 ppm and fragment mass tolerance to 0.6 Da. Fixed modifications were carbamidomethyl

(Cys +57.021 Da), TMT 6plex (Lys, N-terminus +229.163 Da), and dynamic modifications included methionine oxidation (+15.995 Da) N-terminal acetylation (+42.011 Da). Results were filtered to a strict 1% false discovery rate.

Volcano plots[50-51]were generated in Excel 2011 to illustrate the differentially expressed proteins between any two of the three sample types. Specifically, we calculated the $\log_2$ fold change of each identified protein from any two sample types and its corresponding -$\log_{10}p$-value. We used Protein Analysis Through Evolutionary Relationships (PANTHER)[52-53] to categorize the proteins that had significantly different relative abundances between any of the two samples according to molecular function, biological process, and protein class.
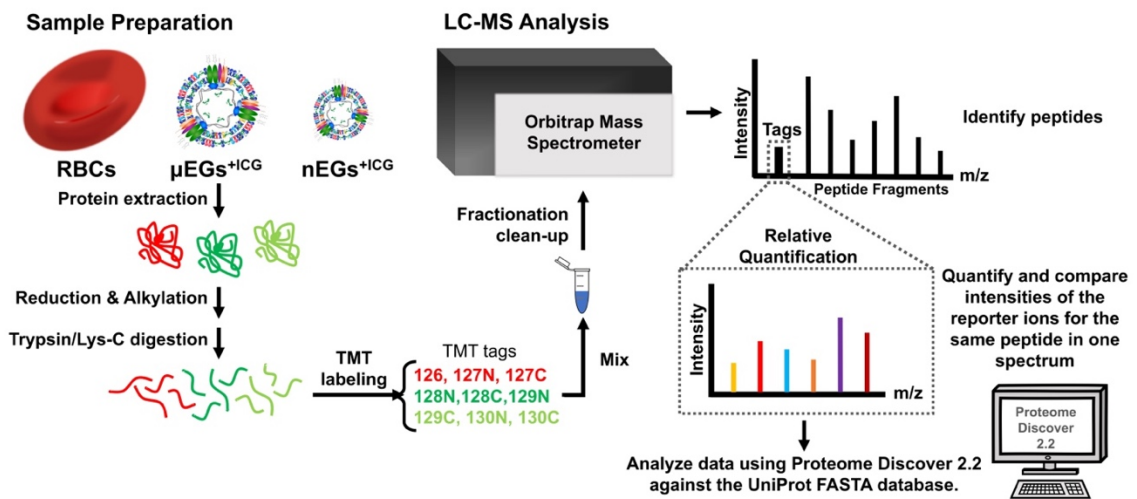


**Figure 2.1.** Sequence of steps for TMT experiments. Proteins from each sample type was extracted, followed by reduction, alkylation, and digestion of the proteins prior to specific TMT isobaric tag labeling. Next, all the samples were combined and fractionated prior to LC-MS analysis. Data analysis and quantification were achieved by Proteome Discover 2.2 against the UniProt FASTA database.

**2.4 Results and Discussion**

**2.4.1 SDS-PAGE**

SDS-PAGE analysis revealed that the membrane protein band 3, and other cytoskeletal proteins consisting of α-spectrin (240 kDa), β-spectrin (220 kDa), protein 4.1R (80 kDa) and protein 4.2 (72 kDa)[54-56] were retained in μEGs and μEGs[+ICG] (Figure 2.2). Based on their MWs, as determined by the comparison of their $R_f$ values with the ladder as well as the known MW of each proteins reported in the published literature[49], we expect that the remaining label bands in Figure 2 correspond to dematin (~ 48 kDa), tropomodulin (~ 43 kDa), tropomyosin (~ 27 kDa), and protein 8 (~23 kDa)[49, 57].[49, 57] These proteins were also retained in μEGs and μEGs[+ICG] (Figure 2.2).
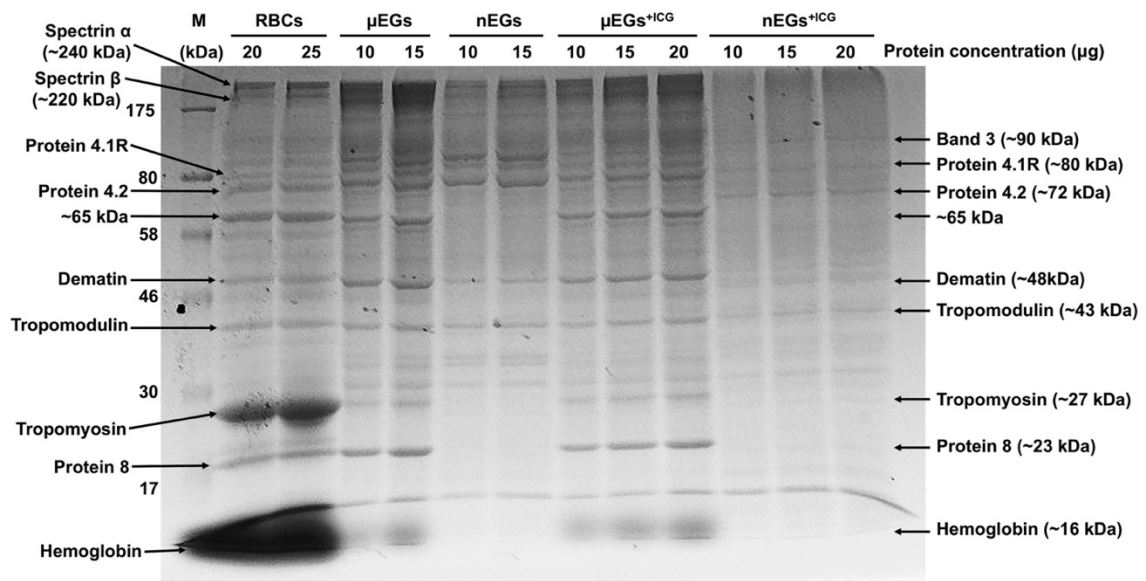


**Figure 2.2.** SDS-PAGE analysis of protein expressions in RBCs, μEGs, nEGs μEGs[+ICG], and nEGs[+ICG]. Each sample was loaded into the gel at different protein concentration ranging between 10-25 μg for electrophoretic running. The nEGs[+ICG] were formed by sequential mechanical extrusion of μEGs through 800, 400, and 200 nm polyester porous membrane three times. M: Protein ladder.

The RBCs membrane is anchored to the underlying network of cytoskeletal proteins via ankyrin- and protein 4.1R (actin junctional complex)-based protein complexes[58-59]. These complexes have vital roles in maintaining the structural integrity of normal RBCs by serving as a system of vertical linkages that connect the membrane bilayer to the cytoskeleton. Band 3 is one of the main transmembrane proteins that links the bilayer to ankyrin. The principal protein constituents of the RBC cytoskeleton are α- and β-spectrin, actin protofilament, dematin, tropomyosin, and tropomodulin[59-60]. These proteins are part of the actin junctional complex and involved in maintaining the membrane mechanical stability of RBCs[61-64]. Other studies have indicated that dematin maintains the integrity of the membrane skeleton by reinforcing the lateral interaction between actin filament and spectrin tetramers[65], and its depletion destabilizes the association of the cytoskeleton to plasma membrane[60].

Our findings suggest that hypotonic treatment and ICG loading had little to no marked effect on the presence of these proteins in μEGs and μEGs[+ICG] (Figure 2.2). Nevertheless, it should be recognized that the linkages between the membrane and cytoskeleton may be disrupted, resulting in changes to the membrane mechanical properties and deformability of these RBC-like particles[15]. Weakened vertical linkages between the membrane and cytoskeleton can lead to dissociation of the spectrin tetramers into dimers[45, 66]. Furthermore, hypotonic treatment is associated with clustering and re-arrangement of band 3[67-68].

Hypotonic treatment did not result in complete depletion of hemoglobin in μEGs and μEGs[+ICG]. These results are consistent with the absorption spectrum (Figure 2.3)

showing spectral peaks at 412, 542, and 575 nm, respectively corresponding to the Soret, fundamental ($Q_0$) and its vibronic tone ($Q_v$) associated with oxyhemoglobin[69], as well as quantitative optical phase images demonstrating the presence of residual oxyhemoglobin in µEGs and µEGs[+ICG].[15]
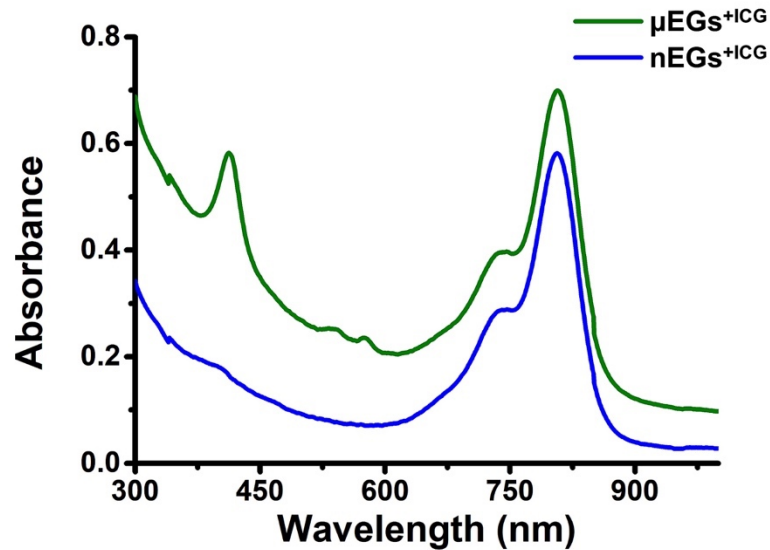


**Figure 2.3**. Absorption spectra of µEGs[+ICG] and nEGs[+ICG]. Constructs were suspended in 1xPBS for the recordings. Each displayed absorption spectra is an averaged measurement of triplicate samples.

The nano-sized particles (nEGs and nEGs[+ICG]), fabricated by mechanical extrusion of the micro-sized particles, had several faint and missing protein bands as compared to non-extruded micro-sized particles (µEGs and µEGs[+ICG]) and RBCs (Figure 2.2). During the extrusion process, the cells are passed through cylindrical pores with nano-sized diameters, resulting in cell lysis and re-assembly of membrane lipids to from nano-sized vesicles (e.g., nEGs)[70]. We attribute the loss or reductions in expression levels of specific proteins such as dematin and tropomyosin to the extrusion process.

To further observe the effects of the extrusion process, we performed the SDS-PAGE analysis after the extruding the particles through progressively smaller pores (800, 400, and 200 nm), with each extrusion through each pore size repeated three times. Specifically, we centrifuged the nano-sized particles formed following the extrusion through each of the pore sizes and collected both the pellet and supernatant for SDS-PAGE analysis to identify some of the proteins that were removed from the particles and released into the supernatant as a result of each extrusion. We quantified the relative expression of each band to the band of RBCs using ImageJ.

Two bands associated with the pellets and corresponding to dematin and tropomodulin became progressively fainter after each extrusion, whereas the bands corresponding to tropomyosin, and protein 8, which have lower molecular weights, became faint immediately after the first extrusion of the μEGs through the 800 nm pore diameter (Figure 2.4A). The bands associated with these four proteins were detected in the supernatants (Figure 2.4B), suggesting that they were removed from the RBC ghosts during the extrusion process. In addition, we observed two prominent bands in the supernatants. Based on our proteomic data, we suggest that they may correspond to entries 151-152 (~ 74 kDa) and entries 183-188 (~ 65 kDa) in Table S2.1 in Supporting Information. These are cytoskeletal proteins such as keratin and part of the actin junctional complex, which mediates binding of protein 4.1R to spectrin[58]. Since the aforementioned proteins are involved in maintaining the mechanical stability of normal RBCs, we anticipate that their removal will compromise the mechanical characteristics of the nano-sized particles formed

from RBCs. Changes in mechanical properties and deformability are thought to modulate

the cellular uptake and biodistribution of nanoparticles[71-73].
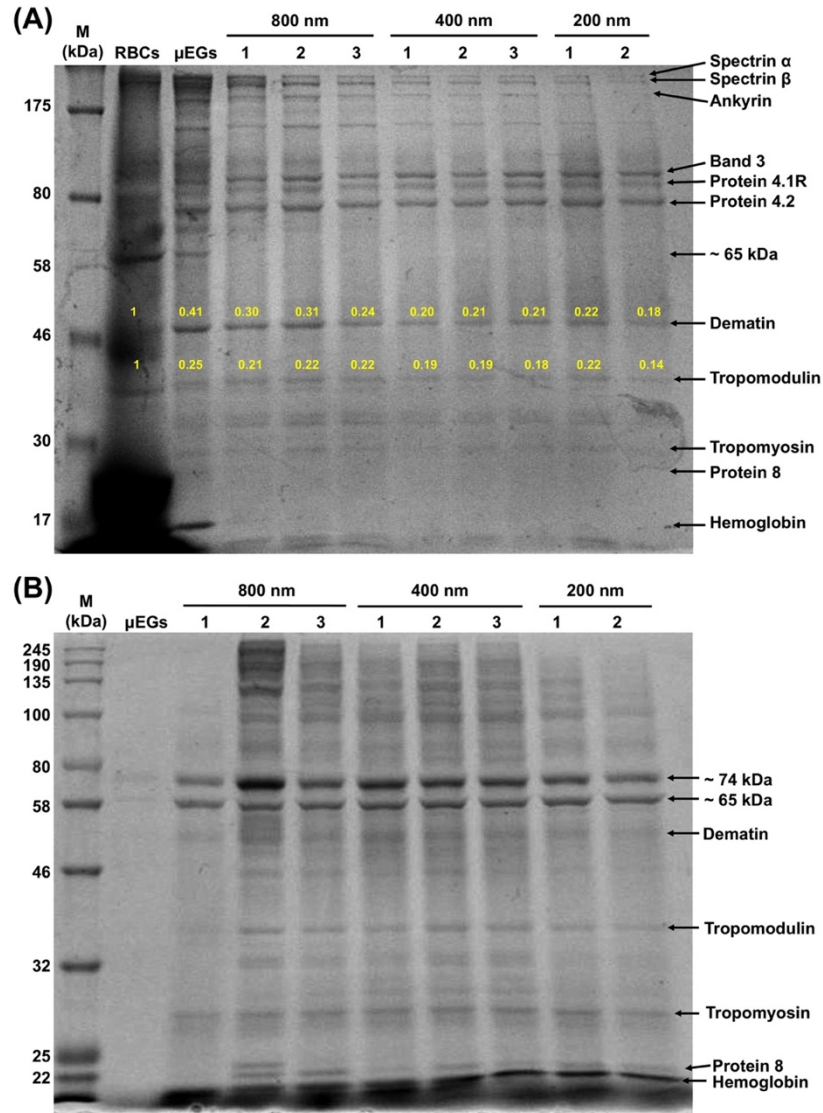


**Figure 2.4.** SDS-PAGE analysis of protein expressions following sequential extrusion of µEGs through 800, 400, and 200 nm pore diameters. Particles and supernatants were collected after each extrusion step for analysis. (A) Pellets, and (B) Supernatants. Numbers 1, 2, and 3 respectively refer to first, second, and third extrusion through each of the indicated pore diameters. The yellow numbers in (A) correspond to the relative expressions of the bands to that of RBCs as determined from the intensity analysis of the bands using ImageJ. M: Protein ladder.

The band associated with hemoglobin disappeared following the first extrusion through the 800 nm pore diameter (Figure 2.4A), concomitant with the emergence of a hemoglobin band in the supernatant (Figure 2.4B). Consistent with these results, the $Q_0$ and $Q_v$ peaks associated with oxyhemoglobin absorption were absent in the absorption spectrum of nEGs$^{+ICG}$, and there was minimal presence of the Soret band (Figure 2.3). These results indicate that while the hypotonic treatment of RBCs did not result in complete depletion of hemoglobin from human RBCs (Figure 2.3), extruding the RBC ghosts through 800 nm diameter pore was sufficient to eliminate the residual hemoglobin.

**2.4.2 Quantitative Analysis of RBC-derived Optical Particles by TMT-MS**

We performed TMT-MS to identify the proteins and quantify their relative abundances in RBCs, $\mu$EGs$^{+ICG}$, and nEGs$^{+ICG}$. In total, 884 proteins were detected in each sample. Of these, 710 proteins were quantifiable in RBCs, $\mu$EGs$^{+ICG}$, and nEGs$^{+ICG}$ in all three replicates (Supporting Information, Table S2.1). To determine if the abundance of each identified protein among RBCs, $\mu$EGs$^{+ICG}$, and nEGs$^{+ICG}$ showed statistical significance, we conducted t-test analysis on the remaining 710 proteins. Of these, 363 proteins had sufficient data (abundance values above detectable threshold from all three TMT channels in the triplicate samples) to perform t-test analysis (see Table S2.2 in Supporting Information for proteins without sufficient data). Using these criteria, we present volcano plots to show the statistical significance of differences in the relative protein expressions for $\mu$EGs$^{+ICG}$ vs RBCs (Figure 2.5A), nEGs$^{+ICG}$ vs. RBCs (Figure 2.5B), and $\mu$EGs$^{+ICG}$ vs nEGs$^{+ICG}$ (Figure 2.5C). In these plots, the -$\log_{10}$ of $p$-value is plotted against the $\log_2$ ratio

of the relative protein abundance (fold changes)[74]. The more spread-out the volcano plot, the more differences there are in the protein abundances between two samples.

The protein profile of μEGs[+ICG] is more similar to that of RBCs while nEGs[+ICG] present more differences in their proteomic composition as compared to both RBCs and μEGs[+ICG]. Specifically, our statistical analysis demonstrated that in comparison with RBCs, only 8 proteins (glutamate dehydrogenase 1, glutathione synthetase, kell blood group glycoprotein, calumenin, receptor expression-enhancing protein 5, non-secretory ribonuclease, monocarboxylate transporter 1, calpain-5) had significantly differentially relative abundance in μEGs[+ICG] (Table S2.3). However, 45 proteins in nEGs[+ICG] had significantly different abundance as compared to RBCs. Comparing nEGs[+ICG] to μEGs[+ICG], 230 proteins had statistically significant relative abundances (Table S2.3), accounting for ~ 63% of the total proteins identified in these two samples, suggesting that the extrusion processes induced substantial effects on the proteome of nEGs and nEGs[+ICG], compared to μEGs and μEGs[+ICG].
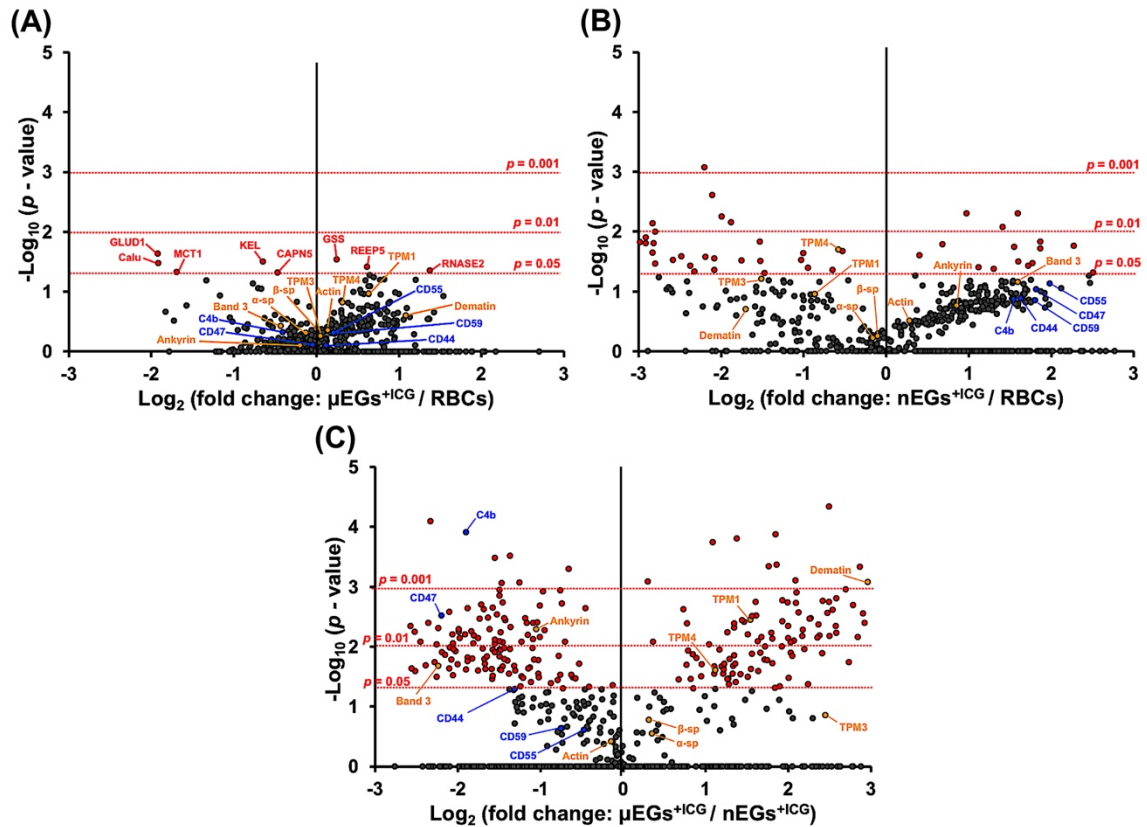
**Figure 2.5.** Volcano plots associated with proteomics analysis of (A) $\mu EGs^{+ICG}$ vs RBCs, (B) $nEGs^{+ICG}$ vs RBCs, and (C) $\mu EGs^{+ICG}$ vs $nEGs^{+ICG}$. Horizontal dotted lines correspond to $p = 0.05$, $0.01$ or $0.001$. Each dot represents a particular protein. The fold change is calculated by abundance value of protein identified in a given sample divided by abundance value of the same protein quantified in another sample. Three independent fabrications were used to generate triplicate experiments for each sample. C4b: Complement component 4b; TPM: Tropomyosin; $\alpha$-sp: $\alpha$-spectrin; $\beta$-sp: $\beta$-spectrin; GLUD1: Glutamate dehydrogenase 1; GSS: Glutathione synthetase; KEL: Kell blood group glycoprotein; Calu: Calumenin; REEP5: Receptor expression-enhancing protein 5; RNASE2: Non-secretory ribonuclease; MCT1: Monocarboxylate transporter 1; CAPN5: Calpain-5.

The biodistribution and circulation time of RBC-based particles is influenced by proteins that provide mechanical stability as well as those that mediate evasion from the immune cells. We provide a partial listing of these mechano- and immune-modulatory proteins in Table 2.1. Through our proteomics analysis, we have estimated that the relative

abundance levels of ankyrin, band 3, and protein 4.2 are, respectively, reduced by about 12.8, 25.8, and 36.5% in μEGs[+ICG] as compared to RBCs (reduction percentages are calculated from the abundance rations provided in Table S2.1, Supporting Information). However, other proteins that participate in the actin-junctional complex showed increased expression levels in μEGs[+ICG] as compared to RBCs. These proteins included actin with increased expression of 10%, tropomodulin (36.8%), α-/β-adducin (96.8 and 56.6%, respectively), tropomyosin (76.8%), and dematin (112.4%). Combined with reductions in ankyrin, band 3, and protein 4.2, these changes may be sufficient to alter the membrane mechanical properties of μEGs[+ICG] and weaken the adhesion between the membrane and the cytoskeleton[15].

**Table 2.1.** Quantitative comparisons of mechano- and immuno-modulatory proteins.

| Accession | Protein | MW (kDa) | Abundance Ratio (µEGs+ICG) / (RBCs) | Abundance Ratio p-value (µEGs+ICG) / (RBC) | Abundance Ratio (nEGs+ICG) / (RBC) | Abundance Ratio p-value (nEGs+ICG) / (RBC) | Abundance Ratio (µEGs+ICG) / (nEGs+ICG) | Abundance Ratio p-value (µEGs+ICG) / (nEGs+ICG) |
|---|---|---|---|---|---|---|---|---|
| | **Mechano-modulatory Proteins** | | | | | | | |
| P02549 | Spectrin alpha chain | 279.8 | 0.915 | 0.490 | 0.894 | 0.606 | 1.278 | 0.283 |
| P11277 | Spectrin beta chain | 246.3 | 0.999 | 0.430 | 0.931 | 0.556 | 1.243 | 0.167 |
| P16157 | Ankyrin | 206.1 | 0.872 | 0.802 | 1.807 | 0.172 | 0.482 | 0.005 |
| P35611 | Alpha-adducin | 80.9 | 1.968 | 0.306 | 0.552 | 0.742 | 2.317 | 0.029 |
| P35612 | Beta-adducin | 80.8 | 1.566 | 0.255 | 0.395 | 0.750 | 3.503 | 0.007 |
| P02730 | Band 3 anion transport protein | 101.7 | 0.742 | 0.379 | 3.022 | 0.070 | 0.212 | 0.021 |
| A0A2R8Y6D0 | Protein 4.1 | 61.4 | 0.851 | 0.658 | 2.045 | 0.110 | 0.451 | 0.006 |
| P16452 | Erythrocyte membrane protein band 4.2 | 77 | 0.635 | 0.454 | 2.635 | 0.066 | 0.212 | 0.005 |
| Q08495 | Dematin | 45.5 | 2.124 | 0.252 | 0.308 | 0.198 | 7.803 | 0.001 |
| Q00013 | 55 kDa erythrocyte membrane protein (p55) | 52.3 | 0.877 | 0.563 | 1.449 | 0.230 | 0.600 | 0.002 |
| P60709 | Actin | 41.7 | 1.1 | 0.444 | 1.217 | 0.312 | 0.904 | 0.386 |
| P28289 | Tropomodulin-1 | 40.5 | 1.368 | 0.277 | 0.565 | 0.616 | 3.102 | 0.008 |
| H7BYY1 | Tropomyosin 1 (TPM 1) | 28.7 | 1.55 | 0.108 | 0.551 | 0.112 | 2.910 | 0.004 |
| J3KN67 | Tropomyosin alpha-3 chain (TPM 3) | 33.2 | 1.043 | 0.616 | 0.352 | 0.062 | 5.459 | 0.140 |
| A0A2R8Y5V9 | Tropomyosin alpha-4 chain (TPM 4) | 28.6 | 1.244 | 0.151 | 0.669 | 0.020 | 2.166 | 0.025 |
| | **Immuno-modulatory Membrane Proteins** | | | | | | | |
| Q08722 | Leukocyte surface antigen CD47 | 35.2 | 0.97 | 0.778 | 3.523 | 0.093 | 0.218 | 0.003 |
| H7BY55 | Complement decay-accelerating factor (CD55) | 58.9 | 1.158 | 0.492 | 3.963 | 0.074 | 0.720 | 0.244 |
| P13987 | CD59 glycoprotein | 14.2 | 1.194 | 0.483 | 3.495 | 0.141 | 0.593 | 0.233 |
| P16070 | CD44 antigen | 81.5 | 1.086 | 0.792 | 3.091 | 0.132 | 0.403 | 0.051 |
| A0A140TA29 | Complement C4-B (C4B) | 187.5 | 0.755 | 0.482 | 2.926 | 0.136 | 0.268 | 0.000 |

Consistent with our SDS-PAGE analysis (Figure 2.4), the proteomic profiles obtained from TMT-MS showed relatively lower abundance levels of dematin (69.2%), tropomodulin (43.5%) and tropomyosin (33.1%~64.8%) in nEGs[+ICG] as compared to normal RBCs. In addition, the actin junctional complex related proteins α- and β-adducin in nEGs[+ICG] also showed lower relative abundance levels of about 44.8% and 60.5%, respectively, as compared to RBCs.

Other studies have indicated that the rigidity of the nanoparticles plays a part in their effectiveness as drug delivery vehicles where shorter circulation times are associated with nanoparticles that have higher Young's moduli[63-64, 75]. These findings may be attributed to faster uptake rates of more rigid nanoparticles by the immune cells[72, 76]. Therefore, changes in the expression levels of the aforementioned structural proteins in nEGs[+ICG] may influence the mechanical characteristics of these nanoparticles, and ultimately their circulation pharmacokinetics.

Another contributing factor to of the circulation time of RBC-based carriers relates to specific membrane proteins involved in regulating the interaction with the immune system. Specifically, the decay accelerating factor (CD55) and MAC-inhibitory protein (CD59) provide protection against complement activation by binding to C3b and C4b proteins to prevent the formation of MACs[77]. CD47 serves as a "self-marker" on RBCs that impedes phagocytosis through interaction with the inhibitory phagocytic receptor, SIRPα expressed on macrophages[13, 78-79]. Our proteomic analysis indicates that the relative abundance of the aforementioned immune markers on both μEGs[+ICG] and nEGs[+ICG] were not significantly different from RBCs (Figures 2.5A,B and Table 2.1). These results are

consistent with our previous study where using fluorescence immunostaining we showed by that CD47 is retained on µEGs[+ICG] and nEGs[+ICG14]. Nevertheless, we point out that the extrusion process may induce conformational changes to CD47, possibly switching its role to activate phagocytosis[80]. Such a switch would be consistent with our in vivo fluorescence imaging of C3H mice microvasculature where the half-life of in bloodstream was reduced from ~ 49 minutes for µEGs[+ICG] to ~ 15 minutes for nEGs[+ICG]. [45] Since CD47 resides within the ankyrin-based complex, it is possible that conformational changes to CD47 in µEGs[+ICG] may occur as a result of disruptions in the vertical linkages in the complex[81].

Additionally, CD44, a multi-functional transmembrane glycoprotein expressed on RBCs and leukocytes, is involved in regulation of hyaluronic acid, mediating the adhesion of leukocytes, and triggering phagocytosis[82-84]. Increased relative abundance of CD44 on nEGs[+ICG] (Figure 2.5B, Table 2.1) may also play a role in activating their phagocytic removal, and reducing the circulation time of these nanoparticles.

**2.4.3 Categorization of Identified Proteins with Significantly Different Abundances**

To further understand the characteristic of the identified proteins with significantly different abundances, we categorized those proteins according to gene ontology (molecular functions, biological processes, and protein class) based on the PANTHER classification system[52, 85]. (Figure 2.6). The detailed list of all proteins with significantly different relative abundances is provided in Table S2.3 of Supplementary Information.

When categorized by molecular function, comparing µEGs[+ICG] with RBCs, the largest fraction of proteins with significantly different relative abundances were those related to enzymatic activity (62.5% of the proteins, corresponding to 5 proteins) (Figure

2.6A). In this category, when comparing nEGs$^{+ICG}$ vs RBCs, and μEGs$^{+ICG}$ vs nEGs$^{+ICG}$, the largest fractions were those associated with binding with approximate values of 38.6% (17 proteins) and 40% (90 proteins), respectively (Figures 2.6B,C).

When comparing μEGs$^{+ICG}$ vs RBCs by biological function, the greatest fraction of proteins (37.5% of the proteins, corresponding to 3 proteins) were those involved in metabolic processes including catabolism and macromolecular processes such as protein synthesis and degradation (Figure 2.6D). When comparing nEGs$^{+ICG}$ vs RBCs, and nEGs$^{+ICG}$ vs μEGs$^{+ICG}$, the majority of proteins with significantly different abundances were related with cellular processes, defined as any process that occurs at the cellular level such as cellular developmental, protein folding, and transmembrane transport. Specifically, 54.5% of the proteins (corresponding to 24 proteins) when comparing nEGs$^{+ICG}$ vs μEGs$^{+ICG}$ (Figure 2.6E), and 62.7% of the proteins (corresponding to 141 proteins) when comparing nEGs$^{+ICG}$ vs RBCs (Figure 2.6F) were involved in such processes.

When comparing μEGs$^{+ICG}$ vs RBCs by protein class, metabolite interconversion enzymes such as transferases, ligases and lyases, and protein modifying enzymes such as proteases and protein phosphatases each accounted for 25% of the proteins (corresponding to total of 4 proteins) (Figure 2.6G). Metabolite conversion enzymes also comprised the largest fraction when comparing nEGs$^{+ICG}$ vs RBCs (9.1%, corresponding to 4 proteins) (Figure 2.6H), and μEGs$^{+ICG}$ vs RBCs (14.7%, corresponding to 33 proteins) (Figure 2.6I). When comparing μEGs$^{+ICG}$ vs RBCs, six classes of proteins accounted for the proteomic differences (Figure 2.6G); however, comparing nEGs$^{+ICG}$ vs RBCs (Figure 2.6H) and

nEGs$^{+ICG}$ vs μEGs$^{+ICG}$ (Figure 2.6I), the number of protein classes increased to 14 and 19, respectively.
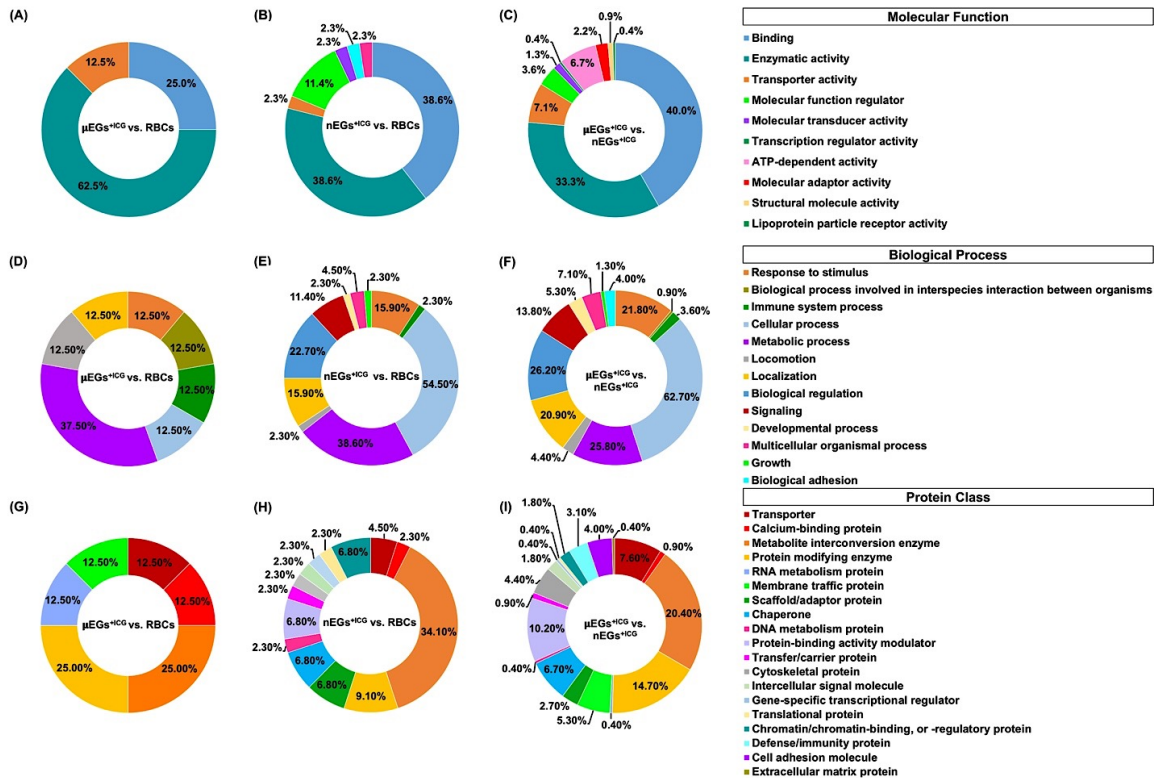


**Figure 2.6.** Categorization of identified proteins with significantly different relative abundances among RBCs, μEGs$^{+ICG}$, and nEGs$^{+ICG}$ according to gene ontology by PANTHER classification system. Categorization by (A-C) molecular function, (D-F) biological process, and (G-I) protein class.

## 2.5 Conclusion

We have studied the proteomic profiles of μEGs$^{+ICG}$, nEGs$^{+ICG}$ and RBCs by SDS-PAGE analysis and quantitative TMT-MS. While the protein composition was generally retained in μEGs$^{+ICG}$, nEGs$^{+ICG}$, fabricated by mechanical extrusion of μEGs, showed greater differences in their protein composition as compared to RBCs and μEGs$^{+ICG}$. Specifically, only 8 proteins had significantly different relative abundance in μEGs$^{+ICG}$ while there were

27

45 proteins with significant differences in abundance in nEGs$^{+ICG}$ as compared to RBCs. Moreover, greater differences in the relative abundances of some of the mechano-modulatory proteins such as band 3 and dematin, and immune-modulatory proteins such as CD47, CD55, and CD44 were found in nEGs$^{+ICG}$ as compared to RBCs. The differences in the proteomes of nEGs$^{+ICG}$ vs RBCs may provide a mechanism for altered biodistribution dynamics and circulation times of nEGs$^{+ICG}$ as compared to μEGs$^{+ICG}$ and RBCs.

**Chapter 3: Membrane Cholesterol Enrichment of Red Blood Cell-Derived**

**Microparticles Results in Prolonged Circulation**

**3.1 Abstract**

Particles fabricated from red blood cells (RBCs) can serve as vehicles for delivery of various biomedical cargos. Flipping of phosphatidylserine (PS) from the inner to the outer membrane leaflet normally occurs during the fabrication of such particles. PS externalization is a signal for phagocytic removal of the particles from circulation. Herein, we demonstrate that membrane cholesterol enrichment mitigates the outward display of PS on microparticles engineered from RBCs. Our *in-vitro* results show that the phagocytic uptake of cholesterol-enriched particles by murine macrophages take place at a lowered rate, resulting in their reduced uptake as compared to RBC-derived particles without cholesterol enrichment. When administered via tail vein injection into healthy mice, the percent of injected dose (ID) per gram of extracted blood for cholesterol-enriched particles were ~ 1.5 and 1.8 times higher than the particles without cholesterol enrichment at 4 and 24 hours, respectively. At 24 hours, ~ 43% ID/g of  theparticles without cholesterol enrichment were eliminated or metabolized while ~ 94% ID/g of the cholesterol-enriched particles was still retained in the body. These results indicate that membrane cholesterol enrichment is an effective method to reduce PS externalization on the surface of RBC-derived particles and increase their longevity in circulation.

**3.2 Introduction**

Particles fabricated from red blood cells (RBCs) provide a platform for the delivery of a variety of biomedical cargos[86], including chemotherapeutic drugs[87-89], photosensitizers[6, 88-

[89], and imaging contrast agents[2, 9, 89-91]. A key principle motivating the use of RBCs as delivery vehicles is the presence of specific membrane proteins including CD47, which prevents phagocytic uptake by macrophages, and CD55 and CD59, which protect the RBCs from complement damage and cell lysis[92]. These membrane proteins offer a mechanism for a prolonged circulation time of the cargo before the vehicles are ultimately eliminated by the immune system.

Common methods for encapsulation of various cargos into RBC-based platforms are based on biochemical treatment of RBCs in hypotonic buffers or by exposure of RBCs to electric field pulses (i.e., electroporation)[93-98]. Phospholipids in the membrane bilayer of RBCs and other eukaryotic cells have an asymmetrical distribution where phosphatidylserine (PS) and phosphatidylethanolamine are confined to the inner (cytosolic facing) leaflet and phosphatidylcholine and sphingomyelin are predominantly in the outer (extracellular facing) leaflet[99-101]. Hypotonic treatment and electroporation can result in flipping of PS from the inner to the outer leaflet[45, 102-106]. Physiologically, flipping of PS is associated with RBC senescence, where it serves as an "eat-me" signal for phagocytosis by splenic macrophages that contain a PS receptor[107-108].

Transmembrane amino-phospholipid translocases (flippases) are involved in localization of PS by actively transferring it from the outer to the inner leaflet of the membrane in an ATP-dependent manner, with ATP11C identified as a major flippase in human RBCs[109]. In addition to flippases, transmembrane scramblases bidirectionally and non-selectively transport phospholipids in a $Ca2^+$-dependent but ATP-independent manner,

with phospholipid scramblase 1 (PLSCR1) considered as a key scramblase in human RBCs[101, 109-110].

It has been reported that cholesterol is an important regulator of PLSCR1 activity and PS localization to the inner leaflet of the membrane[109]. Specifically, decreasing the cholesterol content of RBCs has been shown to activate PS scrambling and externalization of PS to the outer membrane leaflet. van Zwieten et al. have also reported that cholesterol depletion led to increased PS flipping[111]. The exact mechanism for cholesterol-induced inhibition of PLSCR1 remains to be elucidated, but it is thought to involve a cholesterol-binding motif in PLSCR1[112].

In relation to microparticle delivery systems derived from RBCs, the inhibitory effects of cholesterol on PS flipping and the subsequent phagocytic outcomes have not been studied. Herein, we demonstrate for the first time that enrichment of the membrane cholesterol of microparticles fabricated from RBCs can be used to reduce PS externalization to the outer leaflet of these particles and, subsequently, decrease the uptake of the particles by murine model macrophages in vitro and increase the circulation time concomitant with lowered distributions in the reticuloendothelial system (RES) of mice.

In this study, we have used indocyanine green (ICG), a near-infrared (NIR) sensitive molecule, approved by the FDA for specific clinical indications[33, 113-114] and with extensive utility in clinical fluorescence imaging[115-119] as the cargo of choice for encapsulation. Additionally, ICG serves as an optical marker for quantitative assessment of the biodistribution of RBC derived particles. We refer to these particles as micro-sized NIR erythrocyte-derived transducers (μNETs) as they can transduce NIR light to emit

fluorescence, generate heat, or produce reactive oxygen species[6, 45]. We have previously investigated the use of µNETs for real-time intravascular fluorescence imaging and photothermal destruction of the microvasculature, similar to vascular malformations found in port wine stain lesions[45]. ICG-doped RBCs have been used to characterize microvascular vasomotion in humans[97-98]. We have used nanosized RBC-derived particles containing ICG for NIR fluorescence imaging and photodestruction of tumors in animal models[6, 120]. The present study is an important step towards the engineering of RBC-derived particles with appropriate biochemical characteristics, based on cholesterol incorporation, to enhance the bioavailability of the particles resulting from reduced clearance by the immune cells. Membrane cholesterol enrichment is also relevant to the fabrication of RBC-based particles containing not only optical materials but also other types of biomedical cargos[121-122].

## 3.3 Material and Methods

### 3.3.1 Fabrication of µNETs and µNETs with Cholesterol-Enriched Membranes

RBCs were isolated from 1 mL of whole human blood (Biological Specialty Corp.) by centrifugation twice in cold (4 °C) isotonic (~300 mOsm) phosphate-buffered saline (PBS) (referenced as 1× PBS). Isolated RBCs were then repeatedly washed in 1 mL of cold hypotonic PBS (0.25×, 15 min, 20,000g) to deplete the hemoglobin content of the cells. The resulting microsized erythrocyte ghosts (µEGs) were resuspended in 1 mL of 1× PBS. We designate the µEGs in 1 mL of solution as having a relative number concentration of 1 N.

To load ICG (MP Biochemicals) into µEGs, we added 1 mL of 300 µM ICG dissolved in water into the solution consisting of 1 mL of 1 N µEGs and 1 mL of 0.1 M Sørensen's buffer (Na2HPO4/NaH2PO4, ∼140 mOsm, pH ∼ 8), resulting in an ICG concentration of 100 µM in this loading buffer (∼147 mOsm). To form µNETs, µEGs were incubated in this solution for 30 min at 4 °C (Figure 3.1). The resulting µNETs were then washed twice in 1 mL of 1× PBS (15 min, 20,000g) and resuspended in 4 °C 1× PBS to a final volume of 1 mL and stored at 4 °C for no longer than 24 h before experiments.

Methyl-β-cyclodextrin (MβCD) is commonly used to generate cholesterol inclusion complexes that donate cholesterol to the membrane of cells.43,44 To form µNETs with enriched membrane cholesterol (referred to as C+-µNETs), isolated RBCs were incubated in hypotonic 0.25× PBS solution containing the cholesterol–MβCD complex (48 mg of cholesterol per gram of cholesterol–MβCD complex) (Sigma-Aldrich), followed by centrifugation (15 min, 20,000g, 4 °C) (Figure 3.1). In this study, the cholesterol concentration within the cholesterol–MβCD complex was 15 mM because we determined that this particular concentration resulted in the maximum level of cholesterol being imparted to the membrane of µEGs as compared to other concentrations experimented in the range of 5–30 mM (Figure S3.1). For all cholesterol-loading procedures, the molar ratio of MβCD to cholesterol in the complex was ∼5.8:1. The supernatant, containing hemoglobin and excess cholesterol–MβCD complex, was decanted, and 1 mL of fresh 0.25× PBS solution containing the cholesterol–MβCD complex was added. This process was repeated until the supernatant became colorless. The pellet, consisting of cholesterol-enriched µEGs, was then loaded with ICG using the same method

described above to form C⁺-µNETs. To account for slight differences in the loading efficiency[123] of ICG into µNETs (~37%) and C⁺-µNETs (~33%), we concentrated the suspension of C⁺-µNETs accordingly so that both µNET and C⁺-µNET solutions had the same absorbance value at 780 nm.
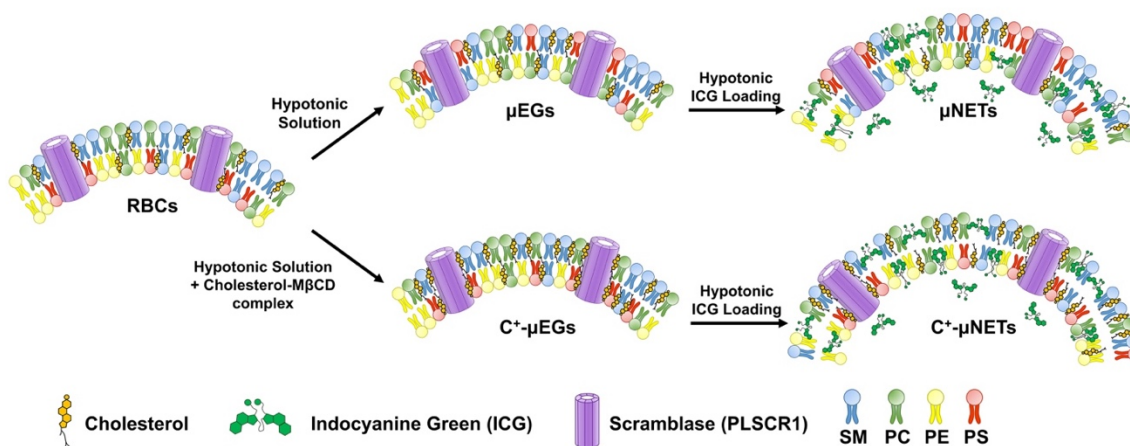


**Figure 3.1.** Schematic of the methods to form µNETs and C⁺-µNETs. For C⁺-µNETs, the cholesterol–MβCD complex was added in a hypotonic solution during simultaneous hemoglobin depletion and membrane enrichment with cholesterol prior to ICG loading.

### 3.3.2 Characterization of Particles

We measured the ζ potentials (Zetasizer Nano series, NanoZS90, Malvern Instruments) of the particles suspended in 1× PBS using folded capillary ζ cells. Five individual measurements were collected for each sample and averaged to determine the mean ζ potential ± standard deviation (SD). Absorption spectra of µNETs and C⁺-µNETs suspended in 1× PBS were recorded in the spectral range of 280 to 900 nm using a UV–visible spectrophotometer (Jasco V-670 UV–vis spectrophotometer, JASCO) with an optical path length of 1 cm. Fluorescence spectra of µNETs and C⁺-µNETs suspended in 1× PBS in response to photoexcitation at 780 ± 2.5 nm filtered from a 450 W xenon lamp

were obtained using a fluorometer (Fluorolog-3 spectrofluorometer, Edison). Normalized

fluorescence emission χ(λ) spectra were quantified as

$$\chi(\lambda) = \frac{F(\lambda)}{1-10^{-A(\lambda ex)}} \tag{2}$$

where F is the fluorescence emission intensity in response to the excitation wavelength ($\lambda_{ex}$)

and A($\lambda_{ex}$) is the absorbance of the sample at the excitation wavelength. Each NET solution

was diluted 10-fold in 1× PBS prior to absorption and fluorescence measurements.

We imaged the RBCs, μNETs, and C$^+$-μNETs by a quantitative phase imaging (QPI)

system and used the images to estimate their mean Feret diameters. Any abnormally shaped

RBCs or particles (e.g., nondiscoidal shapes in RBCs or noncircular μNETs/C$^+$-μNETs)

were excluded from the analysis. Details of the QPI system are described in previous

publications[124-125]. Briefly, samples were illuminated by a 100W halogen lamp source

through a condenser annulus and condenser lens. A 100× oil immersion objective (NA =

1.3) was used to collect the scattered and unscattered components of light passing through

the sample. The light after sample illumination was filtered to a center wavelength of 595

± 30 nm prior to exiting the microscope. A mirror

directed the scattered and unscattered light to a linear polarizer. The unscattered light

formed an image of the condenser annulus on a reflective spatial light modulator (SLM)

(Hamamatsu LCOS-SLM X- 10468). The SLM was used to introduce four phase shifts in

π/2 increments to the unscattered light. The unscattered components interfered with the

scattered light to form an image of the sample, which was focused onto an electron-

multiplying charge-coupled device (C9100-13, Hamamatsu). To accommodate full

rearrangement of the nematic liquid crystals in the SLM, field delays of 100 ms were used

between the phase modulations. We acquired 10 phase-shifted images every second to yield quantitative phase images at 2.5 frames per second. We designate the image intensity at a given pixel location $i, j$ resulting from the interference between the scattered light and unscattered light at four different phase modulations as $I_0$, $I_\pi$, $I_{\pi/2}$, and $I_{(3\pi)/2}$ respectively. Values of the phase difference ($\Delta\phi$) associated with each interference signal intensity are given as

$$\Delta\varphi\ (i,j) = \ \tan^{-1}\left(\frac{I_{\frac{3\pi}{2}} - I_{\frac{\pi}{2}}}{I_\pi - I_0}\right). \tag{3}$$

We subsequently obtained the resulting phase maps as:

$$\varphi\ (i,j) = \tan^{-1}\left(\frac{\beta \sin\Delta\varphi}{1 + \beta \cos\Delta\varphi}\right) \tag{4}$$

where $\beta$ is the ratio of the amplitude of scattered to un-scattered light intensity at a given pixel location.

We have previously carried out extensive characterizations of RBC derived optical microparticles doped with ICG[69, 123, 126-127]. These studies include ICG concentration-dependent characterizations of the $\zeta$ potential, absorption and emission spectra, excitation–emission maps, relative fluorescence quantum yield, and quantification of optical stability and ICG leakage dynamics and are not repeated here as they are not the subject of this particular study.

### 3.3.3 Cholesterol Quantification Assay

We quantified the membrane cholesterol content in RBCs (positive control), μNETs (negative control), and C⁺-μNETs using the Amplex Red Cholesterol Assay Kit (Invitrogen Molecular Probes). We performed the assay by following the manufacturer's instructions

using a 96-well plate (Corning, Inc.). Briefly, we oxidized the membrane-bound cholesterol using cholesterol oxidase to yield $H_2O_2$, which was then detected using the Amplex Red reagent (10-acetyl-3,7-dihydroxyphenoxazine) in the presence of horseradish peroxidase. Cholesterol oxidase contains a flavin adenine dinucleotide cofactor, which catalyzes the oxidation of cholesterol with $O_2$[128]. The reaction between the Amplex Red reagent and $H_2O_2$ produces resorufin, a highly fluorescent compound with respective absorption/emission maxima at 571 nm/ 585 nm in 50 mM sodium phosphate buffer (pH 7.4). We photoexcited the resorufin at 560 ± 2.0 nm, spectrally filtered from a xenon flash lamp, and obtained the emission recorded at 590 nm using a microplate reader (SpectraMax M3 microplate reader). We then compared the emission values to a cholesterol standard curve that related the fluorescence emission at the same wavelength to various concentrations of cholesterol in the reaction buffer, allowing us to quantify the amount of cholesterol in each sample.

### 3.3.4 Flow Cytometric Quantification of Externalized PS on Particles

We used annexin V-Alexa Fluor 488 conjugate (AVAF488) (Thermo Fisher Scientific) as a detection reagent to assay for PS externalization in μNETs and C+-μNETs[129-130]. Specifically, we added 0.5 μL of each sample to 500 μL of annexin binding buffer (10 mM HEPES, 140 mM NaCl, and 2.5 mM $CaCl_2$ dissolved in water) and 40 μL of AV-AF488 and incubated them for ~20 min at 22 °C before analyzing them by flow cytometry (LSR II, BD Biosciences). Our flow cytometric analysis of externalized PS on each sample was based on ICG fluorescence gating using the APC-Cy7 channel (633

nm excitation laser, 780 ± 30 nm emission filter). Out of the available excitation lasers and emission filters used in this flow cytometer instrument, these optical parameters yielded

maximal NIR fluorescence from the ICG-loaded particle variants. We considered all ICG-positive events to result from the presence of either μNETs or C+-μNETs. We determined the change in median fluorescence intensity (ΔMFI) of the AF488-labeled samples using the FITC/ Alexa 488 channel of the LSR II (excitation wavelength = 488 ± 2 nm, fluorescence emission filter = 530 ± 15 nm) and additionally obtained forward scattering area (FSC-A) versus side scattering area (SSC-A) plots.

### 3.3.5 In-Vitro Assessment of Particle Uptake by RAW 264.7 Macrophages

We used RAW 264.7 murine macrophages, stable at passage 11, to assess the uptake dynamics of μNETs and C+-μNETs[131]. Cells were seeded at a density of ~100,000 per well in a 96- well tissue culture plate and incubated in 100 μL of Dulbecco's modified Eagle's medium (DMEM) supplemented with 10% fetal bovine serum and 1% penicillin/streptomycin for 24 h at 37 °C in 5% $CO_2$. To assess the uptake of each particle type, serum-supplemented DMEM in each well was removed, followed by adding 50 μL of 1 N sample mixed with 50 μL of serum-free DMEM to each well. Cells were incubated with each particle type at 37 °C with 5% $CO_2$ for 30, 60, and 120 min. At each time point, the particles were removed by washing the cells with 1× PBS. The cells were then fixed with 4% paraformaldehyde for 5 min, permeabilized with 2% Tween 20 for 5 min, and stained with 300 nM 4′,6-diamidino-2-phenylindole (DAPI) for 5 min. Between each of these steps, the cells were rinsed with 100 μL of sterile 1× PBS and finally rinsed twice more with 100 μL 1×PBS prior to fluorescence microscopy imaging using an inverted microscope (Eclipse Ti, Nikon).

We used a NIR filter set containing $740 \pm 18$ nm for photoexcitation and a long-pass filter (>780 nm) (41037-Li-Cor IR800, Chroma Technology Corp.) to capture the emitted fluorescence light. Cells' nuclei were visualized using a DAPI filter set (DAPI-5060B-NTE, Semrock Inc.) with $377 \pm 25$ nm for photoexcitation and $447 \pm 30$ nm for emission. ImageJ was used to normalize the window/level of emission from ICG in the NIR channel in each image and stack both DAPI and ICG channels into a single composite RGB image.

To calculate the average NIR emission intensity per cell ($\bar{I}_{cell}$) after incubation with µNETs or C$^+$-µNETs for durations of 30, 60, and 120 min, we summed the NIR intensity values for all pixels in a given image, divided the total intensity by the number of cells in the image, and finally averaged among four images of the same batch of cells as follows

$$\bar{I}_{cell} = \frac{1}{4} \sum_{n=1}^{4} \frac{\sum_{x=1}^{512} \sum_{y=1}^{512} I(x,y)}{n_{cells}} \tag{4}$$

where $I(x, y)$ is the NIR emission intensity value at the pixel position $(x, y)$ in a given image and $n_{cells}$ is the number of cells in the image, obtained by counting the number of the cell nuclei in the DAPI channel using ImageJ[132].

### 3.3.6 In Vivo Assessment of µNET and C$^+$-µNET Biodistribution in Swiss Webster Mice

Healthy female Swiss Webster (SW) mice ($\sim$7–9 weeks old) were obtained from Taconic Biosciences. All animal studies were performed under a protocol approved by the University of California, Riverside Institutional Animal Care and Use Committee (protocol A-20200027). Animals were anesthetized by inhalation of 2% isoflurane gas in oxygen.

All animals were tail-vein injected with 100 μL of either μNETs or C$^+$-μNETs while under anesthesia. Mice were euthanized by inhalation of compressed $CO_2$ gas at 4 or 24 h postinjection of the particles. A total of 16 mice were used in this study with 4 mice per sample type (μNETs or C$^+$-μNETs) per euthanasia time point (4 or 24 h postinjection). Following euthanasia, we collected ~500 μL of blood from the heart by cardiac puncture and extracted the liver, lungs, spleen (organs associated with the RES), and the kidneys for ICG content quantification[133].

For measurement of ICG in blood samples, the blood was first weighed and then mixed with 1 mL of 5% sodium dodecyl sulfate (SDS) to lyse all cells and μNETs/C$^+$-μNETs, thereby releasing ICG. The samples were then incubated at 4 °C for 30 min, followed by centrifugation at 15,000g for 1 h at 4 °C. The supernatant was collected for fluorescence measurements. For organ analysis, samples were weighed and then incubated in 1 mL of 5% SDS for 30 min at room temperature (RT) in the dark. Next, the organs were homogenized using a tissue homogenizer (Omni TH 115, Omni International). We then added 3 mL of 5% SDS to the homogenate and incubated the samples for 30 min at RT in the dark. The crude homogenate was centrifuged at 14,000g for 45 min at 10 °C to separate the aqueous ICG-containing organ extract (supernatant). 1 mL of the supernatant was collected from each tube and used for ICG fluorescence recording. For both blood and homogenized organs, fluorescence emission in the range of 795–900 nm was recorded in response to 780 ± 2.5 nm photoexcitation using a Fluorolog-3 spectrofluorometer (Jobin Yvon Inc., Edison, NJ). We used Gaussian profiles to fit the spectral data points.

### 3.3.7 Analysis of ICG Content in Blood and Organs

The concentration of ICG in each sample of organ/blood was estimated by comparing the spectrally integrated fluorescence emission of the sample in the range of 795–900 nm to a calibration curve that related the concentration of ICG dissolved in 5% SDS to the spectrally integrated emission of ICG in the same band and as measured by the Fluorolog-3 spectrofluorometer. We present the percentage of ICG recovered from each organ or blood sample with respect to the initial injected dose per gram of organ. Statistical analysis of ICG content among various samples and time points was performed using a two-tailed Student's t-test with equal variances.

### 3.4 Results and Discussion

### 3.4.1 Characterizations

Values of the ζ-potentials measured in 1× PBS were similar among RBCs (−14.07 ± 0.76 mV), μNETs (−14.84 ± 1.01 mV), and C⁺-μNETs (−14.62 ± 0.71 mV). These results suggest that sialoglycoproteins, the primary negative charge-bearing components of the RBC membrane, were retained on μNETs and C⁺-μNETs. Furthermore, these results also suggest that the presence of the hydrophilic hydroxyl group of cholesterol facing the external aqueous environment was insufficient to induce a statistically significant difference in the mean ζ potential of C⁺-μNETs as compared to μNETs.

Illustrative absorption spectra of μNETs and C⁺-μNETs associated with samples that were injected into mice are shown in Figure 3.2A. Absorption at 280 nm is attributed to the amino acids (e.g., tyrosine, tryptophan, phenylalanine, and histidine) associated with aromatic rings[134-135]. We observed that the absorbance value at 280 nm was nearly the same

for μNETs and C$^+$-μNETs, suggesting that both samples contained approximately the same number of particles.

Absorption peaks at 412, 541, and 576 nm are the respective Soret peak and fundamental band ($Q_0$) and its vibronic tone ($Q_v$) for porphyrin $\pi \rightarrow \pi^*$ transitions associated with oxyhemoglobin. The higher absorbance values at these wavelengths for C$^+$-μNETs (compared to μNETs) indicates greater hemoglobin content in these particles. This is likely due to increased stability of the cholesterol-enriched RBC membrane during hypotonic treatment. Cholesterol is known to affect protein–protein interactions at the band 3 complex, which forms linkages with the underlying cytoskeletal network[136-137]. The increased presence of cholesterol may serve to stabilize the RBC membrane and reduce the amount of hemoglobin lost during hypotonic treatment of the cholesterol enriched RBCs.

Samples of μNETs and C$^+$-μNETs exhibited similar fluorescence emission characteristics as quantified by the normalized fluorescence intensities (Figure 3.2B) and the spectrally integrated emission intensities (Figure 3.2C). These results indicate that membrane cholesterol enrichment did not significantly alter the emission characteristics of the particles. We suggest that ICG and cholesterol either did not colocalize in the same membrane domains to allow interactions that may have altered the emission characteristics of ICG or if they colocalized, the ICG emission characteristics were not altered due to interactions with cholesterol. Our findings are consistent with a previous study where the emission of free ICG in aqueous solution containing cholesterol was not altered[138].
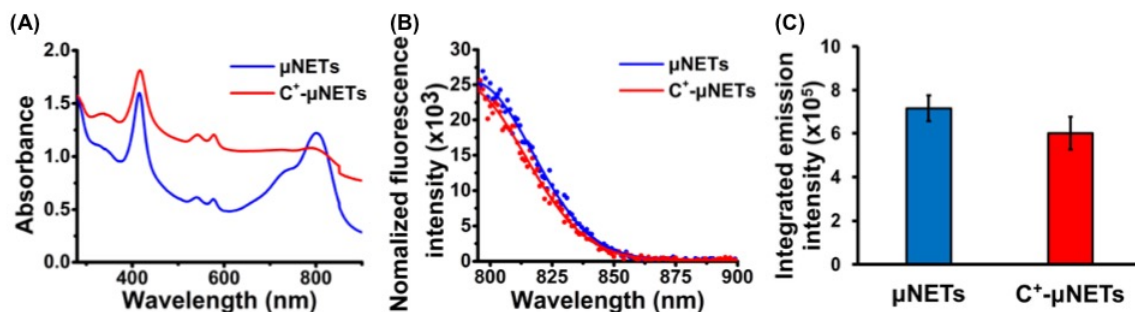
**Figure 3.2.** Optical characteristics of μNETs and C⁺-μNETs. (A) Absorption spectra corresponding to the average of three independent measurements for each sample. (B) Normalized fluorescence emission spectra in response to $780 \pm 2.5$ nm photoexcitation. Data points correspond to the average of three measurements. Solid traces are the Gaussian fits to the averaged data. (C) Emission intensities integrated over the 795–900 spectral band. Each bar is an average of three independent measurements with error bars representing the SDs (n = 3).

### 3.4.2 Reduced Externalization of PS on μNETs via Membrane Cholesterol Enrichment

There was a small (~12%), but statistically significant ($p < 0.05$), reduction in the membrane cholesterol content of μNETs as compared to RBCs (Figure 3.3A). A possible reason for this relatively small reduction is that the lower numbers of particles may have been assayed in the μNET sample as compared to RBCs while performing the cholesterol quantification assay. There was nearly a sixfold increase in membrane cholesterol content of C⁺-μNETs as compared to RBCs ($p < 0.001$) (Figure 3.3A), indicating a large capacity for enrichment of the membrane with cholesterol. We found that a concentration of 15 mM cholesterol in the cholesterol–MβCD solution was sufficient to saturate the membranes (Figure S3.1).
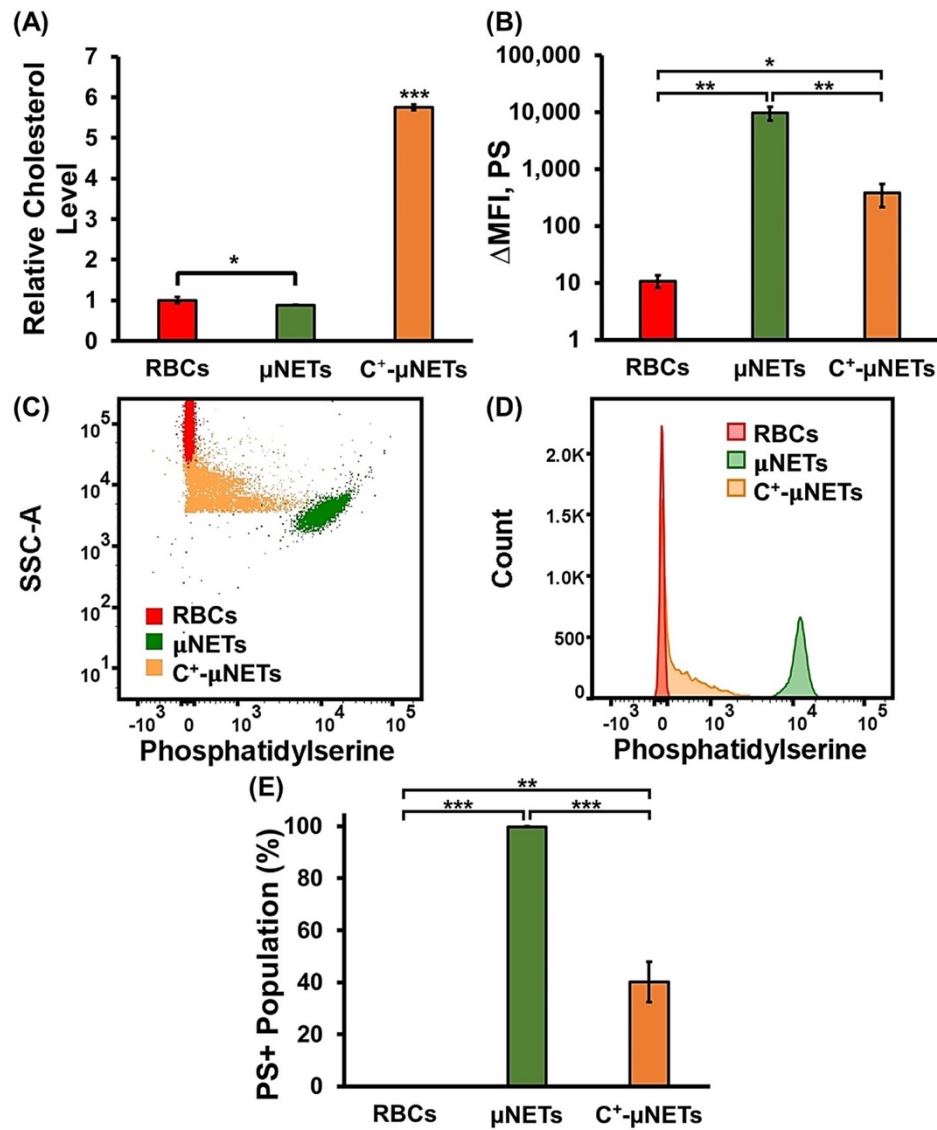
**Figure 3.3.** Quantification of cholesterol content and detection of externalized PS. (A) Relative average membrane cholesterol level of RBCs, $\mu$NETs, and C+-μNETs. Each bar is an average of four independent measurements (n = 4). (B) ΔMFI for RBCs, $\mu$NETs, and C+-μNETs conjugated with Alexa Fluor 488 -labeled Annexin V for PS detection. Each bar represents the average of three independent measurements. (C) Representative dot plots of SSC-A versus fluorescently detected PS for RBCs, $\mu$NETs, and C+-μNETs. (D) Representative counts of RBCs, μNETs, and C+-μNETs fluorescently detected for PS. (E) Mean fractions of PS-positive RBCs, μNETs, and C+-μNETs associated with three measurements. Error bars in panels (A), (B), and (E) represent standard deviations. Asterisks *, **, and ***, respectively, correspond to statistically significant differences with $p < 0.05$, $p < 0.01$, and $p < 0.001$.

As evidenced by the flow cytometry results, the ΔMFI associated with AF488-labeled annexin V for μNETs was about 1000 times higher than that of RBCs ($p < 0.01$) (Figure 3.3B), indicating that μNETs had higher levels of PS externalization. Membrane cholesterol enrichment resulted in approximately ~26-fold reduction in ΔMFI for C$^+$-μNETs as compared to that of μNETs ($p < 0.01$) (Figure 3B), indicating the effectiveness of cholesterol in lowering PS externalization, albeit not to the level associated with RBCs.

Values of SSC-A, which are proportional to the intracellular content of the cells or particles, were highest for RBCs as compared to those of μNETs and C$^+$-μNETs (Figure 3.3C), consistent with highest level of hemoglobin in RBCs. Similarly, minimal fluorescence emission due to PS surface expression was detected from RBCs. In general, μNETs exhibited the lowest values of SSC-A and fluorescence emission, indicative of their least amount of hemoglobin and highest PS externalization. The range of SSC-A values for C$^+$-μNETs was higher than the range for μNETs, consistent with the higher residual hemoglobin in these particles as compared to μNETs (Figure 3.2A), but lower than the range for RBCs, indicative of the lower hemoglobin content in C$^+$-μNETs. The variation in SSC-A for C$^+$-μNETs can be attributed to intraparticle differences in the hemoglobin and ICG content of these particles. We assume the addition of membrane cholesterol competes with the depletion of the hemoglobin process during the hypotonic treatment[139], resulting in a mixture of microsized particles with different degrees of depleted hemoglobin level.

C$^+$-μNETs exhibited a relatively broad range for PS fluorescence (Figure 3.3C), suggesting that there was a nonuniformity in membrane cholesterol enrichment, which

resulted in a nonhomogeneous population of $C^+$-μNETs with varying degrees of PS externalization. Because the lower bound of the SSC-A value for $C^+$-μNETs was associated with particles with various levels of cholesterol, it appears that cholesterol enrichment does not make a significant contribution to the SSC-A values for $C^+$-μNETs. The number–count plot of particles as determined by flow cytometry provided further evidence that there were $C^+$-μNETs with various degrees of PS externalization (Figure 3.3D). We considered all particles with PS labeling greater than $10^2$ to be PS positive. Based on this threshold, only 0.11% of RBCs were PS positive, whereas ~99% of μNETs were PS positive (Figure 3.3E). The cholesterol-enriched $C^+$-μNETs had a significantly lower PS positivity fraction of ~40% (i.e., less than half as compared to μNETs).

### 3.4.3 Morphological Characteristics of Cholesterol-Enriched μNETs

While the SSC-A data provide information about the intracellular components, we also present the FSC-A data as an indication of the size of RBCs and the microparticles (Figure 3.4A). As expected, RBCs had the greatest FSC-A and SSC-A[140-141] due to their relatively large size and presence of hemoglobin and other intracellular components. μNETs, however, had the lowest FSC-A values (Figure 3.4A), indicating their smallest size as compared to RBCs and $C^+$-μNETs, with the latter having intermediate values of FSC-A. Our analysis based on QPI indicated that the respective mean ± SD diameters of RBCs, μNETs, and $C^+$-μNETs were $8.3 \pm 0.6$, $6.7 \pm 0.9$, and $7.1 \pm 0.7$ μm (Figure 3.4B–D).

Using QPI, we could detect the normal biconcave discoid shape of RBCs (Figure 3.4B, red arrows). We also detected echinocytes (Figure 3.4B, blue arrows) and acanthocytes (Figure 3.4B, black arrows) among the RBC population.
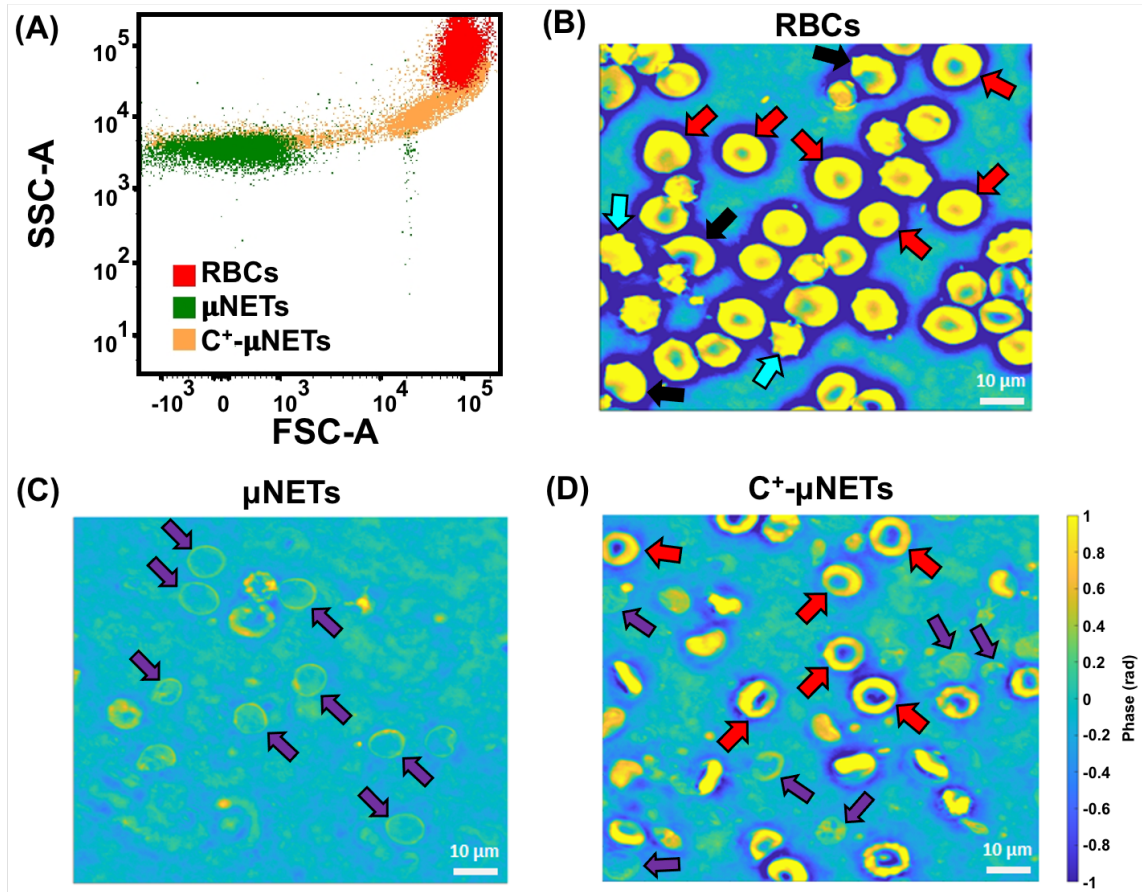
**Figure 3.4.** Morphological characteristics of RBCs, µNETs, and C⁺-µNETs. (A) Representative SSC-A vs FSC-A plots of RBCs, µNETs, and C⁺-µNETs obtained by flow cytometry. Representative falsely colored images of (B) RBCs, (C) µNETs, and (D) C⁺-µNETs obtained by QPI. In panel (B), examples of normal RBCs, echinocytes, and acanthocytes are pointed out by the red, blue, and black arrows, respectively. Purple arrows point to µNETs in panel (C). In panel (D), examples of C⁺-µNETs resembling RBCs or µNETs are pointed out by the respective red and purple arrows. The scale bar for the phase values applies to panels (B–D)

QPI of µNETs illustrated that these particles had a brighter rim (Figure 3.4C, purple arrows), evidenced by higher phase values, as compared to the central part of the particles, indicative of the localization of the residual hemoglobin near the membrane. Spatial variations in the phase values suggest the variabilities in hemoglobin localization and

content among the μNETs. The near-zero phase values in the center of μNETs confirm our spectroscopic findings that μNETs contained minimal hemoglobin.

Based on QPI, we observed two distinct subpopulations of $C^+$-μNETs (Figure 3.4D), consistent with the corresponding SSC-A versus FSC-A plots for these particles (Figure 3.4A). The subpopulation with lower FSC-A and SSC-A values was more similar to μNETs with corresponding phase shifts and morphology (Figure 3.4D, purple arrows). The other subpopulation appeared similar to RBCs (Figure 3.4D, red arrows) with higher FSC-A and SSC-A values, a biconcave discoid shape, central dimple, and large phase shifts due to increased hemoglobin content (Figure 3.4D, red arrows).

### 3.4.4 Cholesterol-Enriched NETs Show Reduced Uptake by RAW 264.7 Macrophages

Illustrative NIR fluorescence images of RAW 264.7 cells after 30–120 min of incubation with μNETs or $C^+$-μNETs are shown in Figure 3.5A. We observed higher NIR emission at 60 and 120 min from the cells incubated with μNETs, indicating that phagocytosis of μNETs occurred at a more rapid rate than phagocytosis of $C^+$- μNETs, resulting in greater uptake of μNETs at these time points.

At the 30 min time point, there was not a statistically significant difference in the mean fluorescence intensity of RAW 264.7 macrophages incubated with either μNETs or $C^+$-μNETs (Figure 3.5B). After 60 and 120 min of incubation, cells incubated with $C^+$-μNETs showed significantly lower mean fluorescence intensity compared to cells incubated with μNETs (Figure 3.5B). There was not a statistically significant difference between the mean fluorescence intensity of cells at 30 or 60 min of incubation with $C^+$-

μNETs ($p > 0.1$); however, at 120 min of incubation with C$^+$-μNETs, the mean intensity became significantly larger as compared to the value at 60 min ($p = 0.03$). In comparison, the mean fluorescence intensity for cells incubated with μNETs continued to statistically increase from 30 to 120 min. These results indicate that membrane cholesterol enrichment was effective in delaying the phagocytosis of C$^+$-μNETs due to their reduced PS externalization as compared to μNETs.
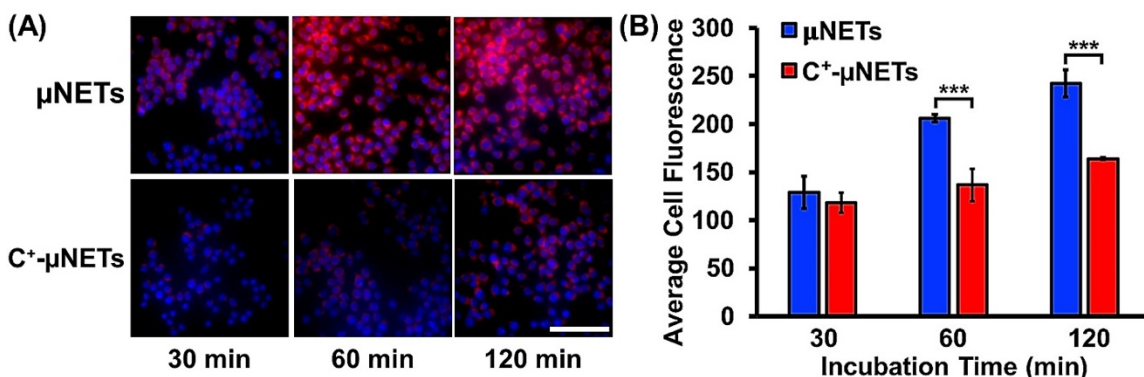


**Figure 3.5.** In-vitro uptake dynamics of μNETs and C$^+$-μNETs by RAW 264.7 murine macrophages. (A) Fluorescence images of RAW 264.7 macrophages after 30, 60, and 120 min of incubation with μNETs or C$^+$-μNETs. Scale bar = 50 μm and applies to all panels. (B) Average NIR fluorescence intensity of RAW 264.7 cells (estimated using eq 4) after incubation with μNETs or C$^+$-μNETs for 30, 60, and 120 min. Error bars are the SDs, and statistical significance is denoted with *** asterisks indicating $p < 0.001$.

### 3.4.5 In-Vivo Biodistribution

To evaluate the efficacy of cholesterol enrichment on prolonging the circulation of μNETs, we analyzed the biodistribution of μNETs and C$^+$-μNETs in healthy SW mice. We recorded fluorescence emission spectra (795–900 nm emission in response to 780 nm excitation) of blood and organs (liver, spleen, lungs, and kidneys) extracted from mice at 4 and 24 h following tail-vein injection of μNETs or C$^+$-μNETs. The liver, spleen, and lungs are the primary organs of the RES with an abundance of phagocytic cells that uptake

foreign materials[142]. The spleen is a blood filtration organ equipped with macrophages that recognize and uptake senescent RBCs expressing PS on their outer leaflets. The liver contains Kupffer cells, which are adherent macrophages on the endothelial lining of the liver sinusoids. The lungs also have a large population of alveolar macrophages that are capable of engulfing microparticles, as well as a dense network of capillaries that can effectively trap exogenous particles[143].

At 4 h postinjection, the Gaussian fits to the fluorescence emission intensity spectrum of blood from mice injected with μNETs were lower than that of mice injected with $C^+$-μNETs (Figure 3.6A). A similar trend was observed at 24 h postinjection. These results indicate that $C^+$-μNETs remained in the blood circulation longer than μNETs for at least up to 24 h after intravascular injection.

As a metric for quantifying μNET and $C^+$-μNET fluorescence in the blood and organs, we used the value of the integrated NIR fluorescence emission across 795–900 nm normalized by the mass of the organ/blood. We observed that the fluorescence signal per gram of extracted blood for $C^+$-μNETs was significantly greater than that of μNETs at both 4 and 24 h time points (~69 and 182% greater, respectively) (Figure 3.6B). Between these time points, the mass-normalized integrated fluorescence signal of μNETs in blood decreased by ~ 62%, while that of $C^+$-μNETs only decreased by about 37%, indicating prolonged circulation of $C^+$-μNETs compared to μNETs.

Analysis of the liver, lungs, kidneys, and spleen revealed that the mass-normalized integrated fluorescence of μNETs was significantly higher in these organs as compared to that of $C^+$-μNETs at 4 h (Figure 3.6B). These results suggest that the prolonged circulation

time of $C^+$-μNETs over the first few hours following tail-vein injection is concomitant with reduced accumulation of $C^+$-μNETs in the RES organs and kidneys. At 24 h, the mass-normalized integrated fluorescence of $C^+$-μNETs was significantly higher than that of μNETs in the lungs (also in the liver and spleen, but not significantly). These results are ostensibly due to clearance of the rapidly sequestered μNETs from these organs via alveolar, hepatic, and splenic phagocytosis pathways and the delayed accumulation of $C^+$-μNETs in these organs over 24 h.
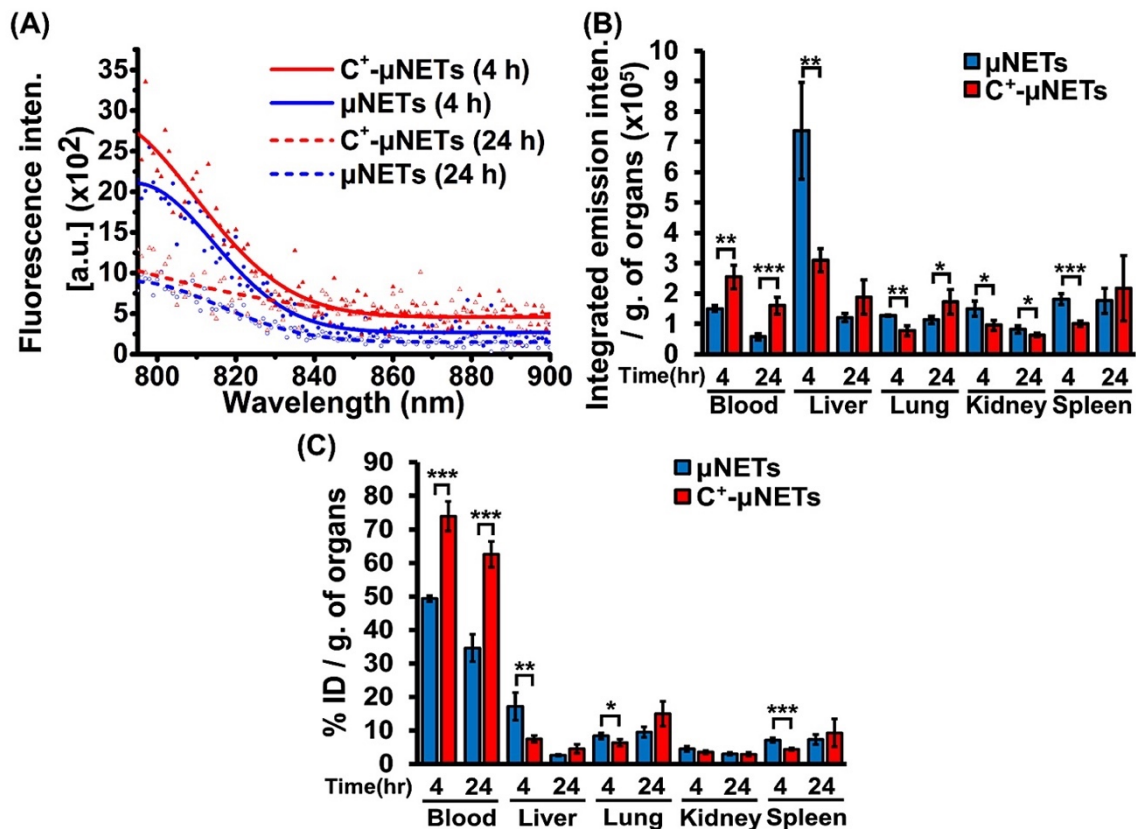
**Figure 3.6.** Biodistribution of μNETs and C⁺-μNETs. (A) Fluorescence emission spectra of blood collected from mice at 4 and 24 h following tail-vein injection of μNETs and C⁺-μNETs in response to $780 \pm 2.5$ nm photoexcitation. Solid traces are Gaussian fits to the data points (C⁺-μNETs at 4 h represented by filled triangles; μNETs at 4 h represented by filled circles; C⁺-μNETs at 24 h represented by unfilled triangles; and μNETs at 24 h represented by unfilled circles). (B) Spectrally integrated emission intensity of blood and homogenized organs normalized to the mass of the organ/blood. (C) Recovered percentage of the initial dose of ICG normalized to the mass of extracted organs and blood (% ID/g) at 4 and 24 h postinjection of μNETs and C⁺-μNETs. In each panel, the means of four independent measurements are presented. Error bars correspond to their SDs from the mean. Asterisks denote statistically significant differences (*, $p < 0.05$; **, $p < 0.01$; ***, $p < 0.001$) between the indicated pairs.

We also quantified the biodistribution of particles in the blood and the extracted organs by calculating the percent of the injected dose (ID) recovered in the organ, normalized by the organ mass (% ID/g) (Figure 3.6C). The mass-normalized fraction of the initial dose of C⁺-μNETs in the blood was significantly higher than that of μNETs at 4

h ($\sim$74 vs 49% ID/g; 1.5-fold increase) and 24 h ($\sim$63 vs 35% ID/g; 1.8-fold increase), indicating that the reduced PS externalization due to membrane cholesterol enrichment was effective in prolonging the circulation time of C[+]-μNETs compared to μNETs.

Hepatic removal of RBCs has been shown to positively correlate with the amount of externalized PS[144]. Consistent with this previous study, we found that for C[+]-μNETs only about 7.5% ID/g had accumulated in the liver as compared to 17.2% ID/g for μNETs at 4 h postinjection ($p < 0.01$) (Figure 3.6C). Similarly, at the 4 h time point, the mass-normalized fraction of μNETs in the spleen ($\sim$7.1% ID/g) was significantly higher than fraction of C[+]-μNETs ($\sim$4.4% ID/g) ($p < 0.001$) (Figure 3.6C), indicating the higher uptake of μNETs by the splenic macrophages. We attribute the greater accumulation of μNETs in the liver and spleen at 4 h to the greater degree of externalized PS on the surface of μNETs, causing them to be more readily recognized and engulfed by hepatocytes, and Kupffer cells[145-146] and splenic macrophages. At 24 h, the hepatic fraction of μNETs significantly decreased to $\sim$2.6% ID/g (Figure 3.6C and Table S3.1), indicating clearance via the hepatobiliary mechanism. At this time point, the hepatic fraction of C[+]-μNETs increased to $\sim$4.5% ID/g (Figure 3.6C and Table S3.1), indicating their slower rate of accumulation in the liver.

We also compared the recovered mass-normalized fractions of μNETs and C[+]-μNETs between the various organs (Table S3.2). At the 4 h time point, the liver was the primary site of accumulation for both μNETs and C[+]-μNETs. The exception was the lungs where the amount of C[+]-μNETs was not significantly different from the liver. At 24 h, the primary sites of accumulation for both μNETs and C[+]-μNETs were the lungs and spleen.

The total recovered mass-normalized percentages of μNETs and C$^+$-μNETs recovered from the blood, liver, lungs, kidneys, and spleen were ~87 and 96% ID/g at 4 h, respectively. At 24 h, the recovered fraction of μNETs was reduced to ~57% ID/g, whereas ~94% ID/g of C$^+$-μNETs was recovered from these compartments. The relatively high recovery of C$^+$-μNETs at 24 h indicates minimal hepatobiliary elimination, phagocytic removal, or urinary excretion of these particles, whereas nearly half of the initial dose per gram of organs for μNETs was eliminated from these compartments by that time.

## 3.5 Conclusion

Externalization of PS on the surface of RBC-derived particles, such as μNETs, can be reduced by membrane cholesterol enrichment. Our in-vitro results indicate that uptake of cholesterol-enriched μNETs (C$^+$-μNETs) by RAW 264.7 murine macrophages takes place at a lowered rate as compared to μNETs without cholesterol enrichment. When administered intravenously via tail-vein injection in healthy mice, the % ID/g of C$^+$-μNETs in blood at 4 and 24 h was ~1.5 and 1.8 times higher than that of μNETs. At 4 h postinjection, μNETs and C$^+$-μNETs that were removed from circulation had primarily accumulated in the liver with lungs as an additional accumulation site for C$^+$-μNETs. At 24 h postinjection, the % ID/g of μNETs and C$^+$-μNETs was greatest in blood, followed by the lungs and spleen. The total mass-normalized percentage of the initial C$^+$-μNETs dose at 24 h was 94% ID/g, but only 57% ID/g for μNETs. These results indicate that membrane cholesterol enrichment is an effective method to reduce PS externalization on the surface of RBC-derived particles and can prolong their circulation in the blood.

## 3.6 Supporting Information

### 3.6.1 Supporting Figure

We adjusted the concentration of cholesterol used to enrich the membranes of µEGs by treating them with various concentrations of cholesterol (between 0-30 mM) while keeping the MβCD concentration fixed at 10 mM (Figure S3.1). The µEGs were treated with cholesterol-MβCD for one hour at 37°C, and then separated by centrifugation and analyzed for cholesterol content as described in the main text.
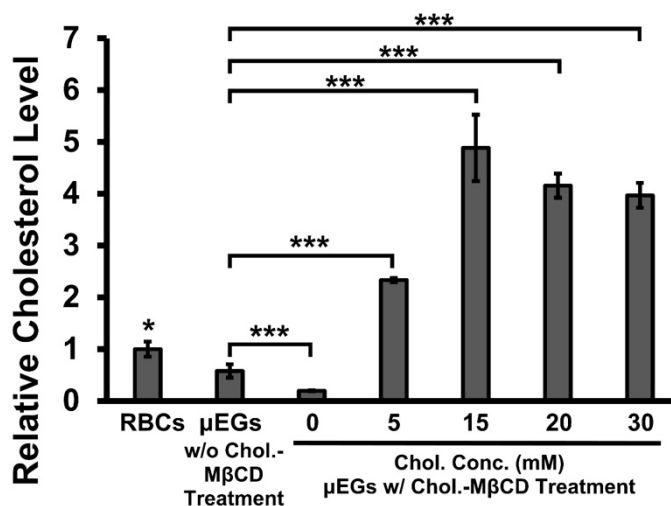


**Figure S3.1.** Quantification of cholesterol content in the membrane of RBCs and µEGs. Values are normalized to the cholesterol content of untreated normal RBCs and presented as averaged values with error bars representing standard deviations associated with three measurements. Asterisks *, **, and ***, respectively, correspond to statistically significant differences with $p < 0.05$, $p < 0.01$, and $p < 0.001$.

### 3.6.2 Supporting Tables

The in-vivo results presented in the main text (Figure 3.6C) are tabulated as Tables S3.1 and S3.2 for direct comparison here. Table S3.1 presents the percentage of initial dose per gram of tissue (%ID/g) in each organ as a comparison between 4- and 24-hours post-

administration of μNETs or C$^+$-μNETs. Table S3.2 presents the %ID/g found in each organ

as a comparison between each organ. The comparison in Table S3.2 provides insight into

the relative biodistribution of μNETs and C$^+$-μNETs across the different organs at 4- and

24-hours.

**Table S3.1**. Recovered percentage of the initial dose (ID) of ICG normalized to the mass of the extracted organs and blood at 4- and 24-hours post-injection of μNETs and C$^+$-μNETs.

| | | %ID/ g. of organs | |
|---|---|---|---|
| **Sample** | **Organs** | **4-hr vs. 24-hr** | ***p*-value Significance** |
| | Blood | 49.36 vs. 34.58 | 0.00084*** |
| | Liver | 17.17 vs. 2.63 | 0.00086*** |
| μNETs | Lung | 8.37 vs. 9.51 | 0.32 |
| | Kidney | 4.51 vs. 2.95 | 0.019* |
| | Spleen | 7.09 vs. 7.26 | 0.86 |
| | Blood | 73.92 vs. 62.56 | 0.015* |
| | Liver | 7.51 vs. 4.51 | 0.02* |
| C$^+$μNETs | Lung | 6.34 vs. 14.98 | 0.0076** |
| | Kidney | 3.50 vs. 2.89 | 0.21 |
| | Spleen | 4.39 vs. 9.27 | 0.091 |

Asterisks denote significant differences between two time points with *, **, and *** corresponding to $p < 0.05$, $p < 0.01$, and $p < 0.001$, respectively.

**Table S3.2**. Recovered percentage of the initial dose (ID) of ICG normalized to the mass of the extracted organs and blood at 4- or 24-hours post-injection of μNETs and C⁺-μNETs.

| Time Point | μNETs | C⁺-μNETs |
|---|---|---|
| **4-hr** | **%ID/ g. of organs (*p*-value)** | |
| Liver vs Blood | 17.17 vs. 49.36 (1.14E-05) | 7.51 vs. 73.92 (2.53E-07) |
| Liver vs Lung | 17.17 vs. 8.37 (1.1E-02) | 7.51 vs. 6.34 (2.03E-01) |
| Liver vs Kidney | 17.17 vs. 4.51 (1.91E-03) | 7.51 vs. 3.50 (7.41E-04) |
| Liver vs Spleen | 17.17 vs. 7.09 (5.64E-03) | 7.51 vs. 4.39 (1.97E-03) |
| Lung vs Kidney | 8.37 vs. 4.51 (1.36E-03) | 6.34 vs. 3.50 (5.89E-03) |
| Lung vs Spleen | 8.37 vs. 7.09 (9.12E-02) | 6.34 vs. 4.39 (2.34E-02) |
| Kidney vs Spleen | 4.51 vs. 7.09 (4.07E-03) | 3.50 vs. 4.39 (5.77E-02) |
| **24-hr** | **μNETs** | **C⁺-μNETs** |
| Liver vs Blood | 2.63 vs. 34.58 (9.87E-06) | 4.51 vs. 62.56 (2.79E-07) |
| Liver vs Lung | 2.63 vs. 9.51 (3.19E-04) | 4.51 vs. 14.98 (3.47E-03) |
| Liver vs Kidney | 2.63 vs. 2.95 (2.82E-01) | 4.51 vs. 2.89 (1.01E-01) |
| Liver vs Spleen | 2.63 vs. 7.26 (1.98E-03) | 4.51 vs. 9.27 (1.1E-01) |
| Lung vs Kidney | 9.51 vs. 2.95 (4.32E-04) | 14.98 vs. 2.98 (1.29E-03) |
| Lung vs Spleen | 9.51 vs. 7.26 (1.25E-01) | 14.98 vs. 9.27 (1.24E-01) |
| Kidney vs Spleen | 2.95 vs. 7.26 (2.96E-03) | 2.98 vs. 9.27 (3.93E-02) |

Statistically significant differences are indicated by the various colors. Red color: $p < 0.05$, orange color: $p < 0.01$, yellow color: $p < 0.001$.

**Chapter 4: Cholesterol-Enriched and Folate-Functionalized Erythrocyte-Derived Optical Nanoparticles for NIR Fluorescence Imaging of Intraperitoneal Ovarian Tumors in Mice**

**4.1 Abstract**

We have engineered nanoparticles derived from erythrocytes that contain the near-infrared (NIR) dye, indocyanine green. These particles can be functionalized with various biomolecules such as folate for targeted imaging of tumor cells. However, externalization of phosphatidylserine from the inner to the outer leaflet of erythrocyte-derived particles is a common problem occurred during the fabrication process, serving as a signal for phagocytic removal of the particles and reducing tumor targeting. Toward developing a new approach, we have engineered erythrocyte-derived nanoparticles enriched with membrane cholesterol and functionalized their surface with folate to target the folate receptor-alpha on ovarian tumor cells to further enhance the tumor accumulating ability. Our in vivo results indicate that cholesterol enriched nanoparticles showed prolonged circulation in blood and organs. Folate functionalized nanoparticles showed higher accumulation in intraperitoneal ovarian tumor in mice at 24 hr post-injection as compared to free ICG and non-modified nanoparticles. We further demonstrate that injection of dual cholesterol-enriched and folate-functionalized nanoparticles present significantly highest NIR fluorescence intensity from tumor than that of all other particle types. This results indicate that dual membrane cholesterol enrichment with folate functionalization is an effective approach to increase the efficacy of these particles for NIR fluorescence imaging of ovarian tumors.

**4.2 Introduction**

Nanoparticles (NPs) are widely employed for various purposes in tumor therapy including drug delivery, diagnosis or imaging[147]. NPs can be useful carriers due to their specific advantages such as smaller size, enhanced permeability and retention effect (EPR), and precise targeting ability[148]. Recently, erythrocyte-derived platforms are garnering increasing attention as delivery carrier for various therapeutic or imaging cargos[2, 6, 11, 45, 86, 89, 149]. A particular feature of using erythrocyte as carrier is their naturally long circulation time (~ 90-120 days) attributed to the presence of "self-marker" protein on membrane surface such as CD47, which signals with phagocyte receptor SIRPα to evade elimination by immune system[13, 92].

Common method to encapsulate various cargos into erythrocyte-based carrier constructs or to facilitate substrate coating on erythrocyte membrane is via hypotonic loading and extrusion, respectively. However, such methods can cause externalization of phosphatidylserine (PS), one of the major phospholipids which is confined to the inner leaflet in the membrane bilayer of red blood cells (RBC)[17], to the outer leaflet[45, 106, 150]. Under physiological circumstances, PS exposure occurs for RBC senescence or eryptosis, where it serves as a recognition signal for phagocytic removal by splenic macrophages[151-153]. As such, RBC-based carriers with surface-exposed PS are susceptible to be cleared, resulting in poor therapeutic efficacy.

Previously, we have reported the membrane cholesterol enrichment on RBC-derived microparticles that contain NIR dye, indocyanine green (ICG), as an effective method to reduce PS exposure on the surface of the particles as well as prolong their

longevity in vivo[150]. NIR fluorophore has been extensively explored for cancer imaging and therapy[154-156]. Of all, ICG remains the only FDA-approved NIR dye for clinical applications ranging from hepatic function monitoring, ophthalmic angiography, sentinel lymph node mapping to cardiac output determination[33, 114, 157-158]. We have engineered the erythrocyte-derived nanoparticles doped with ICG, which we refer to these constructs as NIR erythrocyte-derived transducer (NETs)[9]. Once photoexcited by NIR light, ICG can transduce the absorbed light energy to emit fluorescence, generate heat, or mediate the production of reactive oxygen species[6]. We have previously used these nano-sized NETs (nNETs) for NIR fluorescence imaging and photodestruction of tumors in animal models[6, 11, 120]. Since NPs functionalizing with appropriate biomolecules on surface can further facilitate the selective targeting of tumor cells[159-161]. We have also reported the effectiveness of antibody-functionalized NETs in targeted imaging of ovarian cancer cells[14] and tissue plasminogen activator conjugated NETs for NIR fluorescence imaging and thrombolysis of blood clots in vitro[162]. In this study, one potential targeting option is folate receptor-$\alpha$ (FR$\alpha$), which is overexpressed on the tumors in majority of patients with ovarian cancers and deficient on normal cells[163-165].

Toward developing an approach to improve the therapeutic efficacy of nNETs, we demonstrated here the engineering of nNETs with membrane cholesterol enrichment, folate-functionalization, or dual membrane cholesterol enrichment and folate-functionalization. Further, we evaluated the effectiveness of such membrane cholesterol enriched nNETs (C+nNETs), folate-functionalized nNETs (F-nNETs), and membrane cholesterol enriched with folate-functionalized nNETs (F-C+nNETs) on biodistribution of

60

these nanoparticles in organs and tumors of immunodeficient mice implanted with intraperitoneal ovarian cancer cells.

## 4.3 Material and Methods

### 4.3.1 Fabrication of Nanoparticles

A schematic of nNETs variants fabrication process is presented in figure 4.1. RBCs were isolated from whole human blood (Biological Specialty Corp., Colmar, PA, USA) by centrifugation twice in cold (4°C) isotonic phosphate-buffered saline (defined as 1× PBS; ~310 mOsm). Isolated RBCs were subjected to hypotonic 0.25× PBS (~ 80 mOsm) treatment to remove hemoglobin content of the cell, followed by centrifugation (20,000 ×g, 20 min, 4°C) with the supernatant discarded after each wash. The supernatant containing hemoglobin was discarded, and the hypotonic treatment was repeated until the opaque white pellet was obtained, indicating the formation of micron-sized erythrocyte ghosts (μEGs) with completely or partially removed hemoglobin.

To form the nano-sized EGs (nEGs), μEGs were mechanically extruded sequentially through 800-, 400-, and 200-nm polycarbonate porous membranes (Sterlitech Corp., Kent, WA, USA) using a 10mL LIPEX® extruder (TRANSFERRA Nanosciences Inc., Burnaby, B.C., Canada) with at least three times passing through each membrane until the nEGs were <200 nm in diameter. These nEGs were then incubated in a loading solution containing equal volume ratio of nEGs in 1× PBS, 0.1 M Sørenson's buffer ( $Na_2HPO_4/NaH_2PO_4$, ~140 mOsm, pH~7.4), and ICG solution. The final concentration of ICG in the loading buffer was 15μM. The solution was then centrifuged (100,000×g, 1 hr, 4°C) and washed twice in 1× PBS to remove any excess ICG. The resulting pellets were

suspended in 1× PBS and referred as nNETs.  To form nNETs enriched with membrane cholesterol (referred to as Cholesterol-enriched nNETs; abbr. C+nNETs), μEGs were incubated in a solution containing cholesterol-Methyl-β-cyclodextrin(MβCD) complex with a final concentration of 15mM cholesterol (Sigma-Aldrich) at 37°C for 1hr before and after the extrusion process. Particles were then washed twice to remove any excess cholesterol and then incubated in the loading buffer containing 15μM ICG (as mentioned above). To functionalize the nanoparticles with folate, we proceeded as follow. Specifically, we mixed 1 mg/mL of DSPE-PEG (2000Da)-folate (Nanosoft Polymers, Winston-Salem, NC, USA) with μEGs (as prepared above) prior to extrusion process. After the extrusion, the nanoparticles were then incubated with ICG solution (final concentration of 15μM) to from folate-functionalized nNETs (F-nNETs). To fabricate the folate-functionalized cholesterol-enriched nNETs (F-C+nNETs), μEGs were incubated with both DSPE-PEG (2000Da)-folate(1mg/mL) and cholesterol-MβCD complex (final concentration of cholesterol as 15mM) at 37°C for 1hr before extrusion process. After the extrusion, the particles were incubated with cholesterol-MβCD complex again, followed by washed twice in 1×PBS and centrifuged (100,000×g, 1hr, 4°C). Lastly, particles were loaded with ICG using the same process above to from F-C+nNETs.
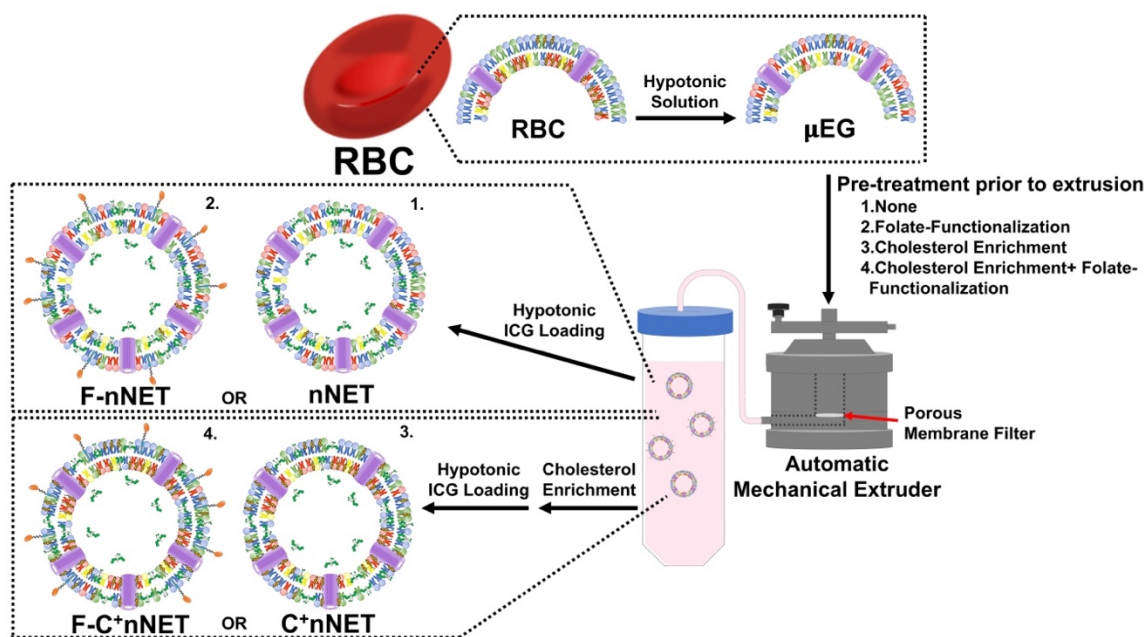
**Figure 4.1.** Schematic of the methodology to fabricate nNETs variants. First, μEGs were formed by treated with hypotonic solution to deplete hemoglobin. nNETs variants were formed by 4 different methods. (1) μEGs were extruded to nano-size (< 200 nm) followed by hypotonic ICG loading to form nNETs. (2) μEGs were functionalized with DSPE-PEG-Folate prior to extrusion process. (3) Cholesterol enrichment was performed both before and after extrusion process to form C⁺nNETs. (4) μEGs were functionalized with DSPE-PEG-Folate and enriched with membrane cholesterol prior to extrusion process. After extrusion process, nanoparticles were then incubated with cholesterol-MβCD complex again, followed by hypotonic ICG loading to form F-C⁺nNETs.

### 4.3.2 Physical and Optical Characterization of Nanoparticles

The zeta potentials and hydrodynamic diameters of the nanoparticles suspended in 1×PBS were measured by dynamic light scattering (DLS) (Zetasizer Nanoseries, NanoZS90, Malvern Instruments). Absorption spectra were recorded using a UV-Vis spectrophotometer (Jasco-V670 UV-Vis spectrometer, JASCO) with optical path length of 1cm. Fluorescence emission spectra of the nanoparticles in response to photoexcitation at $720 \pm 2.5$ nm with a 450-W xenon lamp were acquired using a fluorometer (Fluorolog-3

spectrofluorometer, Edison). Fluorescence emission from folate in response to photoexcitation at $350 \pm 2.5$ nm was recorded in the spectral range of $365 - 900$ nm. We normalized the fluorescence emission $\chi(\lambda)$ spectra using the same equation in our published literatures[9, 123].

### 4.3.3 Cell Culture

SKOV3 ovarian cancer cells (ATCC, Manassas, VA, USA) were used for tumor implantation in Nu/J female nude mice. Cells were cultured in Roswell Park Memorial Institute (RPMI) 1640 medium (Mediatech Inc., Manassass, VA, USA) containing 10% fetal bovine serum (FBS) and 1% penicillin/streptomycin (Corning Inc., Corning, NY, USA) at 37°C in 5% humidified $CO_2$ incubator.

### 4.3.4 Animal Studies

Healthy female Nu/J mice (20-25 g, 6-8 weeks) were purchased from Jackson Laboratory (Bar Harbor, Maine, USA). All animal studies were performed under a protocol approved by the University of California, Riverside Institutional Animal Care and Use Committee (protocol A- 20200027). Animals were anesthetized by inhalation of 2% isoflurane in oxygen. Each mouse was injected with $\sim 2 \times 10^7$ SKOV3 cancer cells intraperitoneally. Mice were monitored until the tumor grows as expected (~18 days).

Tumor-bearing mice were randomly divided into five groups with three animals in each group. Each group was tail-vein injected with 100µL volume of either free ICG (15 µM) or various types of nNETs particles while the animal was anesthetized. The injected dosage of ICG in our studies were estimated to be ~58 and $22.6 - 28.5$ µg/kg weight of the mouse (~20 g) for free ICG and nNETs variants, respectively. We noted that these dosages

are much lower than the LD50 values of ~62 mg/kg in mice[166]and 2 mg/kg in humans recommended by FDA. Mice were euthanized by inhalation of compressed CO2 gas at 24 hr post-injection of the agents. Following the euthanasia, we collected ~500 µL of blood by cardiac puncture and extracted the liver, spleen, kidney, lung, heart, intestine, and tumors for fluorescent images and ICG content quantification[133].

### 4.3.5 Fluorescence Imaging of Extracted Organs

All the extracted organs were imaged in a luminescence dark box as our published literature[127]. Briefly, NIR fluorescence emission from the organs in response to  $700 \pm 30$ nm excitation light from  the two light emitting diodes (LEDs) was captured by a charge-coupled device (CCD) camera (Pixis 1024B, Roper Scientific, Trenton, NJ, USA) with a long pass filter transmitting wavelength greater than 810 nm. The camera exposure time was set as 90 s. We analyzed the acquired images using Image J and present the mean intensity values ($\bar{I}$)  from the selected regions of interest (ROIs) for each organ using the equation as follows:

$$\bar{I} = \frac{\sum_{k=1}^{n}(\frac{1}{m_k})\sum_{j=1}^{p}\frac{I_j}{p}}{n}$$ 
(5)

Where $I_j$ is the pixel intensity at the $j^{th}$ pixel of a given image,  $n$ is the number of a given organ, $m$ is the mass of a given organ, and $p$ is the total number of pixels in the ROI.

### 4.3.6 Analysis of ICG Content in Blood and Organs

To measure the ICG in the blood samples, the blood was first weighed and then mixed with 700 µL of 5% sodium dodecyl sulfate (SDS) (Sigma Aldrich, St. Louis, MO, USA) to lyse all cells and nanoparticles, thus releasing the ICG. The samples were incubated at 4°C for

30 min, followed by centrifugation (15,000×g, 1hr, 4°C). The supernatant was then collected for fluorescence measurements. For organ analysis, each extracted organ was weighed and incubated in 1 mL of 5% SDS at room temperature (RT) for 30 min in the dark. The organs were then grinded using a tissue homogenizer (Omni TH115, Omni International Inc., Kennesaw, GA, USA). We added another 3 mL of 5% SDS to the homogenate and incubated them at RT for 30 min in the dark. After the incubation, the crude homogenate was centrifuged at 14,000×g for 45 min at 10 °C. Then we collected 1 mL of the supernatant containing ICG from each tube for fluorescence measurement. For both blood and homogenized organs, the fluorescence emission in the range of 735-900 nm in response to 720 ± nm photoexcitation wavelength was recorded using a Fluorolog-3 spectrofluorometer.

## 4.4 Results and Discussion

### 4.4.1 Characterizations

As determined by fitting the lognormal functions to the DLS-based measurements, the averaged hydrodynamic diameters ± SD of nNETs, F-nNETs, C⁺nNETs, and F-C⁺nNETs were 129.51 ± 0.76, 131.64 ± 0.18, 118.54 ± 0.59, and 219.2 ± 0.79 nm, respectively (Figure 4.2A). Values of mean zeta potentials ± SD for the particles were as follows: -12.8 ± 0.1 mV for nNETs, -10.27 ± 1.2 mV for F-nNETs, -10.77 ± 0.38 mV for C⁺nNETs, and -10.16 ± 0.32 mV for F-C⁺nNETs (Figure 4.2B). We suggest that the negative values of nanoparticles are attributed to the sialoglycoproteins, the primary negative charge-bearing components of the RBC membrane. nNETs had a significantly lower zeta potential than all the other particles, suggesting that folate functionalization and cholesterol enrichment of

the particles may result in a slight but statistical differences in their zeta potential as compared to nNETs.

The illustrative absorption spectra of nNETs, F-nNETs, C⁺nNETs, and F-C⁺nNETs suspensions in 1×PBS that were injected into mice are shown in figure 4.2C. All the nanoparticles present the spectral peak at ~802 nm which corresponds to the monomeric form of ICG[9, 123], indicating successful encapsulation of ICG in these constructs. Further, the fluorescence emission spectra of the nanoparticles in response to 720 ± 2.5 nm (figure 4.2D) and  350 ± 2.5 nm (figure 4.2E) demonstrate the successful encapsulation of ICG and functionalization of folate, respectively. We noticed the reduced NIR emission intensity of C⁺nNETs, followed by F-nNETs and F-C⁺nNETs as compared to nNETs. Additionally, in response to 350 ± 2.5 nm, there was a reduction in emission intensity of F-C⁺nNETs as compared to F-nNETs, which may be due to folate and cholesterol being in a competitive relationship during the simultaneous functionalization and enrichment process to insert into lipid bilayer.

Further, we validated the cholesterol levels of each particles as shown in figure 4. 2F. There is a statistically significant reduction in the membrane cholesterol content of nNETs as compared to native RBCs. F-nNETs results in significant reduction in membrane cholesterol content as compared to RBCs or nNETs, which may be due to insertion of folate into plasma membrane causing the instability of the membrane structure. There was nearly 1.5- and 2.6-fold increase in membrane cholesterol content of  C⁺nNETs, and F-C⁺nNETs as compared to nNETs, respectively ($p < 0.001$), indicating the successful enrichment of the membrane with cholesterol.
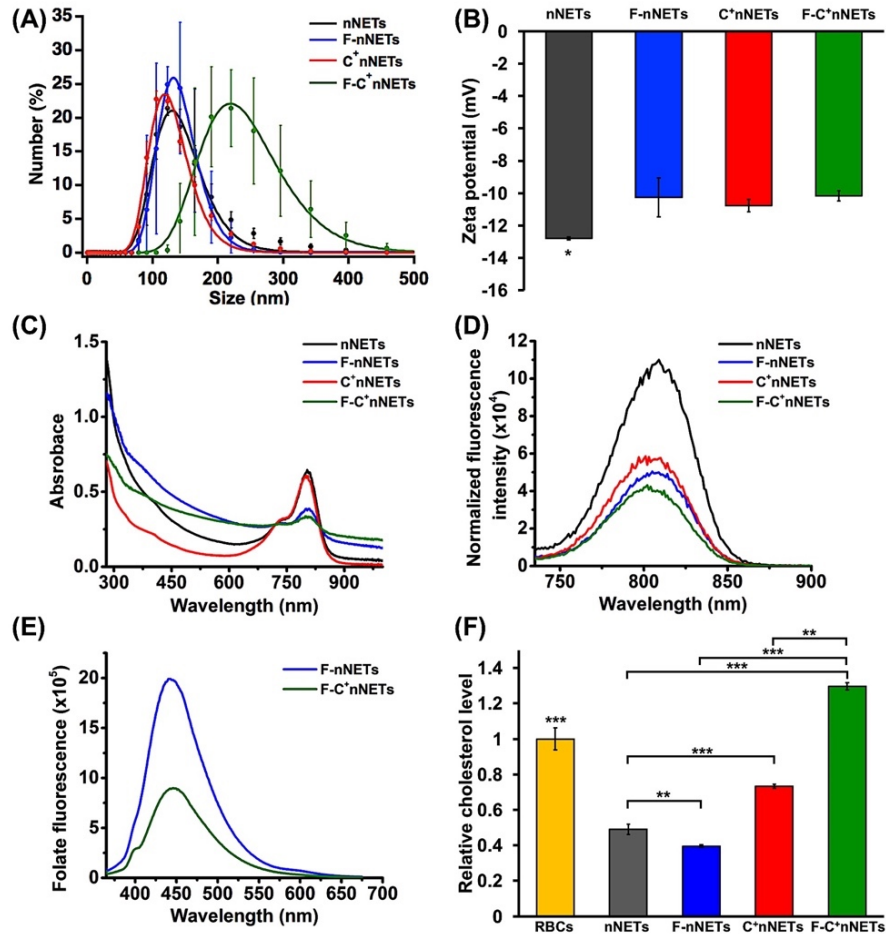
**Figure 4.2.** Characteristics of nNETs variants. (A) Hydrodynamic diameters and (B) zeta potentials of nNETs, F-nNETs, C$^+$nNETs and F-C$^+$nNETs suspensions. Three independent measurements were used to obtain the averaged value. (C) Absorption and (D) Normalized fluorescence emission spectra in response to $720 \pm 2.5$ nm. (E) Folate fluorescence spectra in response to $350 \pm 2.5$ nm of F-nNETs, and F-C$^+$nNETs. (F) Relative average membrane cholesterol level of nNETs variant. Each bar is an average of four independent measurements.

## 4.4.2 Quantitative Fluorescence Imaging of Extracted Organs

We preformed the in vivo experiment to evaluate the tumor accumulating ability of each particle types and their biodistribution on the SKOV3 ovarian xenograft tumors implanted in Nu/J nude mice. Representative fluorescence images and quantitative NIR fluorescence emissions from organs extracted from mice 24 hr post-injection of various particle types

are shown in figure 4.3. Our quantitative analysis of images suggested that NIR fluorescence emission intensity in tumors associated with administration of F-nNETs and C⁺nNETs, was higher than that of free ICG ($p < 0.05$) and nNETs ($p < 0.05$ and $p = 0.09$, respectively), indicating that higher amount of F-nNETs and C⁺nNETs had accumulated in tumors at 24 hr post-injection of particles while most of free ICG and nNETs had been accumulated in spleen and lung (figure 4.3C). Previously, we have reported the effectiveness of enriching membrane cholesterol on RBC-based particles which potentially prolongs the circulation times of the particles[150]. Here, we observed that NIR emission intensity of C⁺nNETs from tumor was greater than that of nNETs at 24 hr time point (54.1% greater). In addition, the NIR emission intensity associated with administration of F-C⁺nNETs was significantly higher than that of only cholesterol enriched or folate functionalized nNETs (179.4% and 139.8% increased, respectively), suggesting that when functionalizing the C⁺nNETs with folate, it further increases the accumulation of the particles in tumors on top of prolonging the circulation of particles by enriching them with membrane cholesterol.
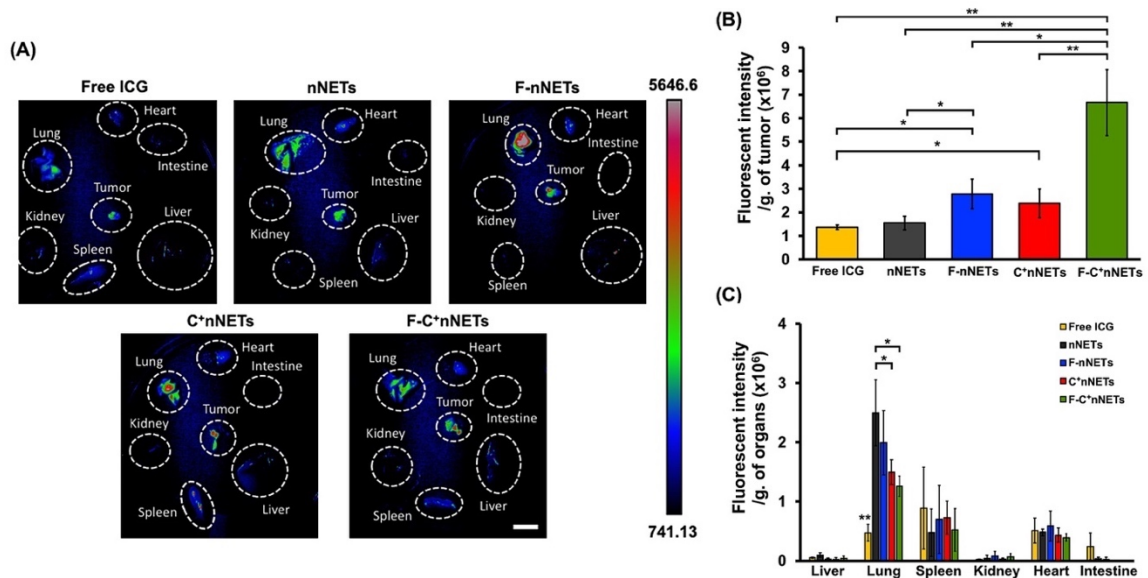
**Figure 4.3.** (A) Representative NIR fluorescence images of organs extracted at 24 hours post tail-vein injection of free ICG, nNETs, F-nNETs, C+nNETs, and F-C+nNETs from immunodeficient mice. Excitation wavelength = 700 ± 3 nm. Emission >800 nm was collected. Scale bar on the right represents the fluorescence emission intensity. Scale bar on the image equals 5 mm and applied to all images. Mean ± standard deviation in fluorescence intensity of (B) tumors and (C) extracted organs. n=3 per agent. Asterisks * and ** correspond to statistically significant differences with $p < 0.05$ and $p < 0.01$, respectively.

The liver, spleen and lungs, primary components of reticuloendothelial system (RES), act as immune defense to phagocytize foreign materials[146]. We observed that decreased levels of NIR emission signals associated with administration of free ICG from the liver and lung with increased signals from intestine at 24 hr post-injection suggest the elimination of most free ICG from the body at this time point. Lung is one of the sites acting as a natural filtration-pulmonary capillaries and with abundant alveolar macrophages located on the luminal surface of Alveolus[167] where particles are likely to be entrapped and cleared from the body. Administration of nNETs showed highest NIR signals from extracted lung and lower fluorescence from tumors at 24 hr post-injection as

compared to F-nNETs, $C^+$nNETs, and F-$C^+$nNETs (figure 4.3C), suggesting that majority of the nNETs has been trapped in lung while other particles mostly still circulate or accumulate in tumors. NIR fluorescence signals associated with F-$C^+$nNETs were lowest in lung, spleen, and heart at 24 hr post-injection, suggesting that most of F-$C^+$nNETs had accumulated in tumors at this time point as evidenced by highest NIR fluorescence signals detected in tumor (figure 4.3B&C).

**4.4.3 Quantification of ICG Content in Blood and Homogenized Organs**

To evaluate the efficacy of cholesterol enrichment and folate functionalization on enhancing the tumor accumulation ability and circulation of the particles, we analyzed and recorded fluorescence emission spectra (735-900 nm emission in response to 720 nm excitation) of blood and organs from mice at 24 hr post-tail vein injection of various particle types. The Gaussian fits to the fluorescence emission intensity spectrum of blood from mice injected with free ICG were the lowest among all other particles at 24 hr post-injection. $C^+$nNETs showed the highest fluorescence emission intensity as compared to all other particles (figure 4.4A), indicating that $C^+$nNETs remained in the blood circulation longer than all other particles at 24 hr following tail-vein injection of particles.

To quantify NIR fluorescence in the blood at 24 hr post-injection of each particle type, we used the value of the integrated NIR fluorescence emission across 735-900 nm normalized by the mass of the blood collected from mice (figure 4.4B). We observed that the integrated fluorescence per gram of extracted blood for $C^+$nNETs was significantly greater than that of other particle types at 24 hr time point (~902% greater than free ICG, ~101% greater than nNETs, ~136% greater than F-nNETs, and ~109% greater than F-

C$^+$nNETs). We also suggest that lower fluorescence signals associated with administration of F-nNETs and F-C$^+$nNETs as compared to nNETs can be attributed to most of those particles accumulated at higher quantities within tumor sites at this time point due to folate functionalization. These result indicates that cholesterol enrichment was effective in prolonging blood circulation of C$^+$nNETs as compared to free ICG and nNETs.
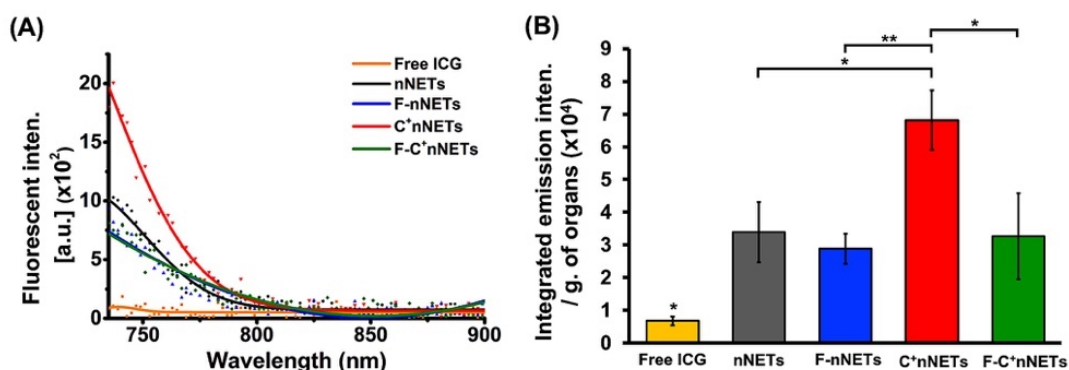


**Figure 4.4.** (A) Fluorescence emission spectra of blood collected from mice at 24 hours following tail-vein injection of free ICG or nNETs variants in response to $720 \pm 2.5$ nm photoexcitation. Solid traces are Gaussian fits to the data points. (B) Spectrally integrated emission intensity of blood normalized to the mass of the blood collected. Asterisks denote statistically significant differences between the indicated pairs (*, $p < 0.05$; **, $p < 0.01$; ***, $p < 0.001$).

Analysis of homogenized tumors revealed that the mass-normalized integrated fluorescence of C$^+$nNETs was significantly higher in tumors as compared to that of free ICG and nNETs ( ~75% and 72% higher, respectively) at 24 hr time point (figure 4.5A). Further, F-nNETs showed significantly higher mass-normalized integrated fluorescence than that of free ICG, nNETs ,and C$^+$nNETs due to folate functionalization. In addition, we observed that the mass-normalized integrated fluorescence in conjunction with administration of F-C$^+$nNETs was significantly increased by at least ~35 and ~103% as compared to F-nNETs and C$^+$nNETs, respectively. When comparing to free ICG and

nNETs, F-C$^+$nNETs further enhanced the mass-normalized integrated fluorescence in tumors by ~254 and ~250%, respectively. These results suggest that while only folate functionalization or cholesterol enrichment on nNETs showed increased fluorescence from tumors, combining both methods further significantly enhance in their quantities accumulated in tumor sites.

We also quantified the fluorescence of each particle types from the homogenized organs as shown in figure 4.5B. We observed that the mass-normalized integrated fluorescence of free ICG was significantly lowest in all organs as compared to that of all other particle types. This suggests that the low accumulation of ICG in RES organs, kidneys, heart, and intestine can be due to elimination of most free ICG via alveolar, hepatic, and splenic phagocytic clearance from the body within 24 hr post-injection. nNETs showed lower integrated fluorescence in most of organs than F-nNETs, C$^+$nNETs, and F-C$^+$nNETs except for lung and intestine. The mass-normalized integrated fluorescence associated with administration of C$^+$nNETs was higher in liver, spleen, kidney, and heart as compared to all other particle types. Consistent with our previous study, we found that cholesterol enrichment on nNETs increased the circulation time of the particles in those organs for up to 24 hr post-injection time point. Moreover, the lower accumulation of F-nNETs and F-C$^+$nNETs in liver, lung, spleen, and kidney as compared to C$^+$nNETs can be attributed to their relatively higher fluorescence signals in tumor site at 24 hr post-injection due to folate functionalization-induced active targeting ability of particles. These results suggest that cholesterol enrichment of nNETs prolongs the circulation times of particles which also showed higher accumulations in tumors than nNETs. However, when further combining

73

with functionalizing their membrane with folate, it significantly enhances their tumor accumulating ability in vivo.
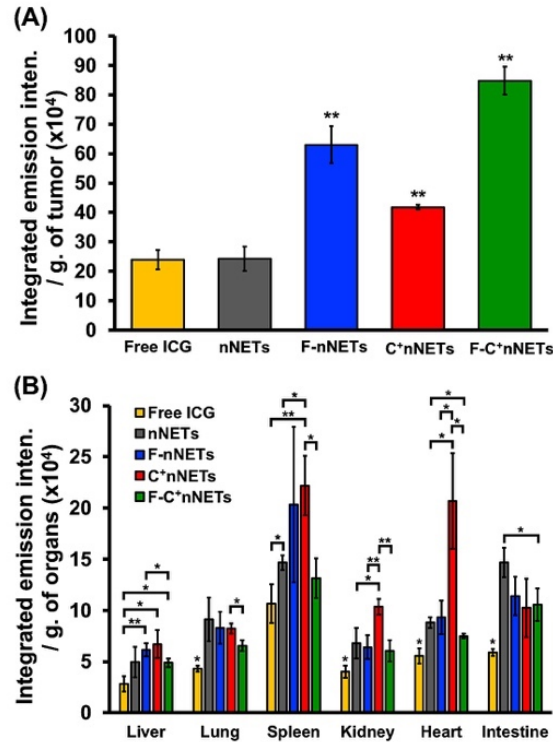


**Figure 4.5.** Spectrally integrated emission intensity of (A) tumors and (B) homogenized organs normalized to the mass of the tumor/blood collected. Asterisks denote statistically significant differences between the indicated pairs (*, $p < 0.05$; **, $p < 0.01$; ***, $p < 0.001$).

## 4.5 Conclusion

We have engineered erythrocyte-derived nanoparticles containing ICG with their membrane enriched with cholesterol, functionalized with folate, and both. Our in vivo study showed that cholesterol-enriched nNETs (C$^+$nNETs) and folate-functionalized nNETs (F-nNETs) results in significant increased accumulation of the particles in tumors of immunodeficient mice at 24 hr post-tail vein injection as compared to nNETs. Moreover, injection of F-C$^+$nNETs results in significantly greater integrated NIR fluorescence as

compared to other particles. These results indicates that cholesterol enrichment of nNETs in conjunction with folate targeting can results in a greater accumulation of particles in tumors which provides a potentially promising capability for enhanced NIR imaging of tumors.

**Chapter 5: Erythrocyte-Derived Optical Microparticles for NIR Photocoagulation of Cutaneous Vasculature**

**5.1 Abstract**

Pulsed dye laser (PDL) irradiation using visible wavelength range of 585-600nm remains as the golden standard treatment for port wine stains (PWSs). Unfortunately, complete and efficient clearance of PWS remains a major challenge due to insufficient penetration of light in skin and high epidermal melanin absorption at PDL wavelengths. Towards developing a more effective approach, we have engineered optical micro-particles, fabricated from red blood cells (RBCs) and doped with FDA-approved indocyanine green (ICG), as targets for pulsed near infrared (NIR) laser treatment at 755 nm. Herein, we evaluated the capability of these particles in mediating photothermal destruction of cutaneous vasculature in the rabbit earlobe as a model system for PWSs. We used laser speckle contrast (LSC) imaging to characterize the blood flow dynamics immediately and up to 24 hrs following laser irradiation. Our results indicate that NIR laser irradiation in conjunction with intravenous administration of the particles present immediate reduction in blood perfusion with complete cessation one day later. Histological evaluations confirmed that RBC-derived optical microparticles are effective in mediating photocoagulation of blood vessels when used in conjunction with pulsed 755 nm laser irradiation, and may ultimately provide a viable approach to treat PWSs.

**5.2 Introduction**

Port wine stains (PWSs) are congenital and progressive malformations of the dermal capillaries which is caused by differentiation-impaired endothelial cells in human skin[168].

These vascular birthmarks occur in an estimated three to five infants per 1000 live births with no gender or racial predilection[169-171]. Most of the lesions do not involute spontaneously, rather, they progressively inflated in size as the patient ages resulting in asymmetry, distortion, and hypertrophy of underlying bone and soft tissues which occurs in 65% of PWS patients[172-174].

The current golden standard treatment for PWSs is the pulsed dye laser (PDL) irradiation using visible wavelengths in the range of 585-600 nm to target the endogenous hemoglobin of the PWS vessels[175-176]. However, PDL treatment fails to achieve complete and efficient clearance of PWSs which also requires multiple therapeutic sessions. It is reported that ten PDL treatment sessions are required to achieve a clinical improvement of 60% in facial PWS[177] and less than 20% of PWS patients experience complete stain lightening[176, 178] with only 21% achieved >75% clearance[179].

This limited therapeutic efficacy is due to insufficient penetration of laser light in skin and high epidermal melanin absorption at PDL wavelengths. For example, with the various depth of PWS (100-1000μm), PDL treatment using therapeutic radiant exposure (fluences; $D_o$) on the order of 8-16 J/cm$^2$ and cryogen spray cooling still do not provide clinically desirable photo-thermolysis of the blood vessels located to at least greater than 500μm below skin surface[180-181]. Further, the current PDL treatment is particularly inefficient to patients with moderate to heavy skin pigmentation (Fitzpatrick skin type III-VI)[182]. Patients with darker skin types possess large numbers of widely distributed melanosome organelles where the melanin pigment is synthesized and stored within melanocytes, resided in the basal layer of epidermis and over the abnormal plexus of

dermal blood vessels[183]. Melanin pigment has a relatively high molar extinction coefficient in current PDL treatment wavelengths (Figure 5.1). As such, light intended to reach the dermal vasculature would be partially absorbed by melanin resulting in inefficient photo-destruction of the blood vessels and the frequent non-specific thermal injury to the epidermis.

To develop a more effective treatment for PWS, an alternative approach is to use an exogenous chromophore as the target that can be photo-activated to generate heat in response to pulsed near-infrared (NIR) laser irradiation. Key advantage of changing the PDL wavelength from 585 nm to NIR wavelength of 755 nm is the nearly threefold reduction in the absorption coefficient of a single melanosome at this NIR wavelength[184-187] (Figure 5.1). One potential candidate chromophore is indocyanine green (ICG), the FDA-approved NIR dye which is one of the least toxic agents administered in human for specific imaging applications[33, 37, 188-191]. Additionally, ICG as a photothermal agent for treating PWS has also been explored[39, 192].

Despite its wide applications, ICG still has limitations such as its short half-life in plasma (3-4 min) and non-specific binding to various plasma proteins[188, 193]. In recent years, much attention has been drawn to cell-mediated carriers such as erythrocytes to protect encapsulated cargos as therapeutic or imaging platforms[2, 9, 162, 194-195] due to their advantages of biodegradability, non-immunogenicity, and naturally long circulation time (~90-120 days)[121, 196-197]. As such, we have engineered erythrocyte-derived optical micro-particles doped with ICG[9] to overcome these limitations of ICG and to serve as the exogenous targets

for pulsed near infrared (NIR) laser treatment. We refer to these constructs as <u>N</u>IR <u>E</u>rythrocyte-derived <u>T</u>ransducers (NETs).

Previously, we have demonstrated the efficiency of these NETs in mediating photothermal injury to cells in vitro[9] and theoretically[10]. Further, we have also reported the potential of NETs functionalized with the ligand binding domain of the EphB1 receptor in targeting endothelial cells (ECs) which could be useful to target ephrin-B2 ligand on PWS ECs[198]. This work aims to evaluate the capability of NETs in mediating photothermal destruction of cutaneous vasculature in the rabbit earlobe as a model system for port wine stains. We chose the rabbit earlobe as a result of its handful of dermal vasculature, containing capillaries as small as 10 μm to blood vessels as large as 250 μm, which reflects the heterogeneity in size distribution shown in PWS. Herein, we used laser speckle contrast (LSC) imaging to characterize the blood flow dynamics following NIR laser irradiation at 755 nm in conjunction with intravenous administration of NETs into the rabbit earlobe vasculature. We also demonstrate the effectiveness of NETs in mediating photocoagulation of blood vessels by histological evaluation.
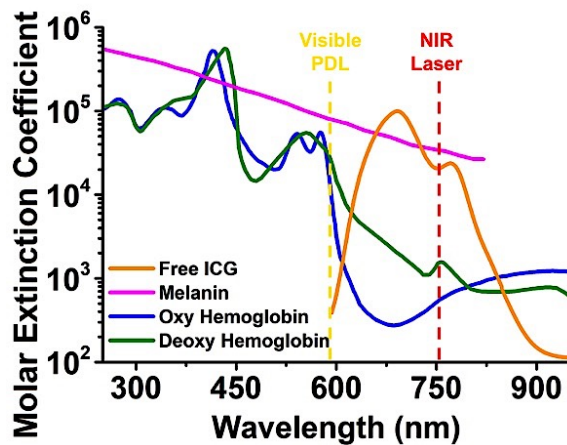
**Figure 5.1.** Molar extinction coefficients spectra for non-encapsulated ICG (2.58mM in water; our own recording), eumelanin monomers (scaled for 100 monomers), oxy- and deoxy-hemoglobin. Dashed vertical lines represent visible wavelengths used by current PDL treatment (585nm) and the NIR wavelength for NIR laser treatment (755nm). Spectra of eumelanin, oxy- and deoxy-hemoglobin were obtained from literature data[185-186].

## 5.3 Material and Methods

### 5.3.1 NETs Fabrication and Characterization

Erythrocytes were isolated from bovine whole blood (Rockland Immunochemicals Inc.) via centrifugation (1300g, 10 min, 4°C) twice in cold isotonic (~310 mOsm) phosphate-buffered saline (PBS) (defined as 1× PBS). Isolated erythrocytes were then washed in hypotonic 0.25×PBS (~80 mOsm) and centrifuged (20,000g, 20 min, 4°C) with supernatant discarded after each wash to remove inner hemoglobin. This step was performed repeatedly until an opaque pellet was obtained and the resulting micro-sized erythrocyte ghosts (μEGs) were suspended in 1X PBS and then loaded with ICG (MP Biochemicals) by incubating them in a hypotonic buffer containing equal volumes of 1X PBS, 0.1M Sørenson's buffer (Na2HPO4/NaH2PO4, ~140 mOsm, pH~8), and ICG solution (final concentration equals ~1.1mM). The solution was then centrifuged (20,000g, 20 min, 4°C) and washed in 1X

PBS twice. The resulting pellets, referred to as μNETs, were resuspended in cold 1X PBS and stored at 4°C for no longer than 24 hr before experiments.

To ensure the quality of the μNETs, absorption and fluorescence spectra were obtained. Briefly, absorption spectra of free ICG (2.58mM) and NETs suspended in 1X PBS were recorded in the spectral range of 280 to 950 nm using a UV-visible spectrophotometer (Jasco V-670 UV-vis spectrophotometer, JASCO) with an optical path length of 1cm. Suspensions of free ICG and μNETs were diluted to have the same absorbance values of ~1.4 at 755 nm. Fluorescence spectra of free ICG and μNETs suspended in 1X PBS in response to photoexcitation at 780 ± 2.5 nm filtered from a 450-W xenon lamp were acquired using a fluorometer (Fluorolog-3 spectrofluorometer, Edison). Normalized fluorescence emission $\chi(\lambda)$ were quantified as follows:

$$\chi(\lambda) = \frac{F(\lambda)}{1 - 10^{-A(\lambda ex)}} \tag{1}$$

Where F is the fluorescence emission intensity in response to photoexcitation wavelength $(\lambda_{ex})$, and $A(\lambda_{ex})$ is the absorbance of the sample at the excitation wavelength.

To validate the morphology of the μNETs, , epifluorescence image and the quantitative phase images (QPI) were obtained. For epifluorescence images , a NIR filter set consisting of 740 ± 18 nm for photoexcitation and a long-pass-filter (>780nm) (41037-Li-Cor IR800, Chroma Technology Corp.) and an electron multiplier gained CCD camera (Quant EM-CCD, C9100-14 Hamamatsu) were used to capture the emitted fluorescence light. Images were then generated using ImageJ where the emission of ICG in the NIR channel was falsely colored in red. For QPI system, the detail protocols are described in

our previous publications[15, 124-125]. The obtained images were used to estimate mean Feret diameters of the μNETs.

**5.3.2 Animals**

All experiments were performed under a protocol approved by the Institutional Animal Care and Use Committee, University of California, Irvine. Adult New Zealand white rabbits with a bodyweight of 3-5 kg were used in this experiment.

**5.3.3 Preparation of Animals**

Rabbits were observed for 3 to 5 days after delivery to allow the animals to settle down and to determine the animals' health. Thereafter, anesthesia of the rabbits was induced with a cocktail of ketamine HCL (37.5mg/kg) and xylazine (5 mg/kg) subcutaneously. After the animal demonstrated loss of consciousness (no voluntary head, limb or eye movement), the rabbit was placed in a supine position on a stage. Legs of the rabbit were supported with four posts, lightly wrapped with Velcro fasteners. Thereafter, isoflurane (3.0% with 1.5 L/min $O_2$) was given via facemask to maintain anesthesia. Depth of anesthesia was evaluated every 10 minutes and the hind limb pedal reflex (withdrawal of foot in response to external stimulus) must remain absent throughout the procedure. The rabbit was placed on a temperature-controlled circulating-water blanket and wrapped with a blanket to prevent hypothermia. During the procedure, the rabbit's body temperature, respiratory rate, heart rate, and the oxygen saturation levels were recorded every 10 minutes. Both ears of the rabbits were shaved, epilated and placed flatly on a Plexiglas plate for subsequent imaging. The dorsal surface of the ear was cleaned with three alternating scrubs of 70%

alcohol and betadine and an intravenous (IV) catheter was placed in the marginal vein of one ear for the administration of experimental agents and euthanasia drug.

### 5.3.4 Color and Laser Speckle Imaging

Digital color photos and laser speckle images of the ear were acquired prior to, shortly and each day after laser irradiation. Color images documented the irradiation site for any blister or burn induced by laser irradiation. Laser speckle imaging (LSI) was used to determine blood flow changes induced by laser irradiation in the blood vessels. During LSI, the ear was transilluminated with a diode laser with a wavelength of 809 nm to produce a speckle pattern. When blood flow is present, the speckle pattern varies with time; otherwise, the pattern is static. The speckle patterns were integrated over 10 ms with a CCD camera and processed with a sliding-window-based algorithm to visualize blood flow in the ear.

### 5.3.5 Fluorescence Imaging

Immediately following administration of the experimental agents, the rabbit ear was illuminated with a diode laser with a wavelength of 785 nm and a maximum intensity of 100 mW/cm$^2$. Resulting fluorescence emission from the vascular area was recorded with a high-sensitivity camera (QuantEM:512SC, Photometrics, Tucson AZ). Fluorescence images were collected at an interval of 1 s in the initial 5 minutes after NETs administration, 1 minute interval in the next 10 minutes and 5 minutes interval till the end of the experiment. Illumination light was blocked between image collection when the interval was 1 or 5 minutes.

### 5.3.6 Laser Irradiation

A laser with a wavelength of 755 nm (GentleLASE, Candela, Wayland MA) was used to irradiate the rabbit ear. Our choice of 755 nm is based on the relatively high absorbance of NETs at this wavelength, availability of biomedical lasers for dermatological applications at this wavelength, and prior use of this wavelength on PWS patients. Laser irradiation pulse duration was 3 ms and only one single pulse was delivered on each irradiated site. Our purpose is to determine the threshold radiant dosage that will result in photo-destruction to blood vessels by using experimental values of 38, 60, and 106 J/cm$^2$.

### 5.3.7 Animal Monitoring, Euthanasia and Tissue Collection

Rabbits were examined every 12 hours for two days. No discomfort, pain or allergic reaction was observed. The animals were euthanized two days after irradiation with an intravenous injection of 150 mg/kg of pentobarbital sodium and phenytoin sodium (Euthasol, Virbac, Westlake TX). Full-thickness ear in the irradiated area and normal control areas were collected immediately after euthanasia and fixed in freshly-prepared 10% neutral buffered formalin for at least 24 hours at room temperature.

### 5.3.8 Vascular Damage Assessment

Excised biopsies were fixed in 10% neutral buffered formalin, processed for histological sectioning, and then stained with hematoxylin and eosin (H&E; EMD Millipore Corp. and Sigma Aldrich Inc.). These H&E stained histological sections were then used to evaluate the photothermal injury to the blood vessels.

## 5.4 Results

### 5.4.1 Characterization of μNETs

Absorption spectra of free ICG and μNETs suspensions in 1X PBS are shown in figure 5.2A. Free ICG at 2 mg/ml in 1X PBS has a dominant H-like aggregate peak (~697 nm) whereas μNETs have a dominant monomer peak (~801 nm), which are consistent with our previous studies[9, 123, 126]. In response to 780 nm photoexcitation, the normalized fluorescence emission intensity values were somewhat higher for μNETs than for free ICG (Figure 5.2B), which can be attributed to the encapsulation of ICG into μEGs prevents the mobility of ICG molecules and thus hinders the fluorescence quenching[9]. An illustrative epifluorescence and QPI of μNETs suspended in 1X PBS and obtained immediately after the fabrication shows that particles are rounded and not aggregated (Figures 5.2C&D). Further, the mean diameter of μNETs based on QPI was $4.72 \pm 0.43$ μm (Figure 5.2D).
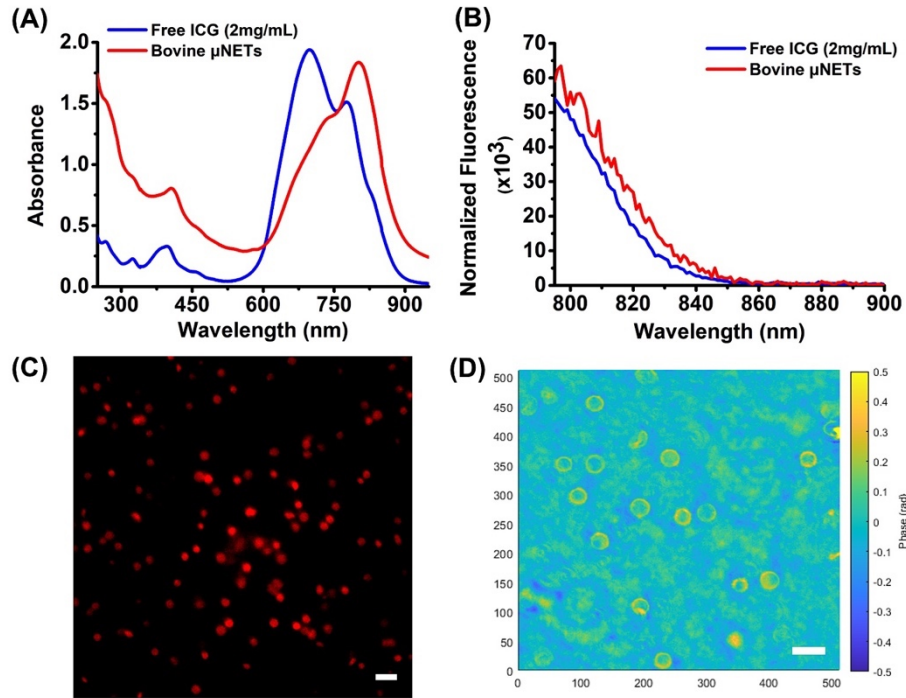
**Figure 5.2.** μNETs Characterization. (A) Absorption, and (B) normalized fluorescence emission spectra for NETs and free ICG in isotonic PBS in response to 780 ± 2.5 nm excitation. (C) Epifluorescence image of NETs. Scale bar = 10 μm. (D) Falsely colored image of NETs obtained by quantitative phase images (QPI). Scale bar = 10 μm.

## 5.4.2 Assessment of Laser-Induced Thermal Injury

We performed the in vivo experiments to evaluate the efficacy of NIR laser irradiation in conjunction with μNETs in mediating the photothermal destruction of blood vessels in rabbit earlobe. For comparison, the histological section of an intact dermal blood vessel from non-irradiated control site in a rabbit is shown in figure 5.3. Pulsed (3 ms) NIR laser irradiation at 755nm without administration of any agent (Figure 5.4), in conjunction with administration of free ICG (Figure 5.5), or μNETs (Figure 5.6) was done at $D_o$ = 38-106 J/cm$^2$. We quantitatively characterized the blood flow dynamics by integrating a laser

speckle contrast (LSC) imaging platform (632.8 nm He Ne laser, 30 mW) with laser irradiation system[199-200].
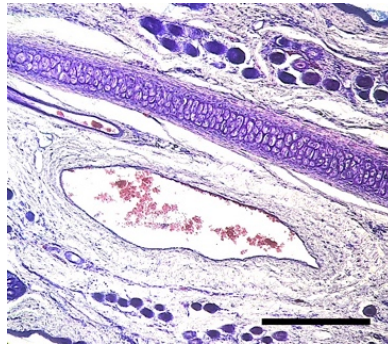


**Figure 5.3**. Non-irradiated dermal blood vessel in a rabbit ear. Scale bar = 50μm.

Our result showed that laser irradiation alone at the highest $D_o$ (106 J/cm$^2$) only resulted in increased blood perfusion (Figures 5.4A-C), indicative of insufficient energy to induce the photothermolysis and the hindrance of coagulation in blood vessels as evidenced by histological analysis (Figure 5.4D). Laser irradiation in conjunction with free ICG injection resulted in reduced blood perfusion immediately after irradiation (Figure 5.5A-C), but with restored blood perfusion one day (24hr) later (Figures 5.5A-D), indicating that the photocoagulation was ultimately not achieved. We also examined the histological section which also showed no signs of coagulation in vasculature (Figure 5.5E). These results suggest that laser irradiation alone or with injection of free ICG performing at the highest radiant exposure ($D_o$=108 J/cm$^2$) still could not induce the photothermal destruction of blood vessels in rabbit ear, which could be associated with fast elimination of free ICG from the circulation.
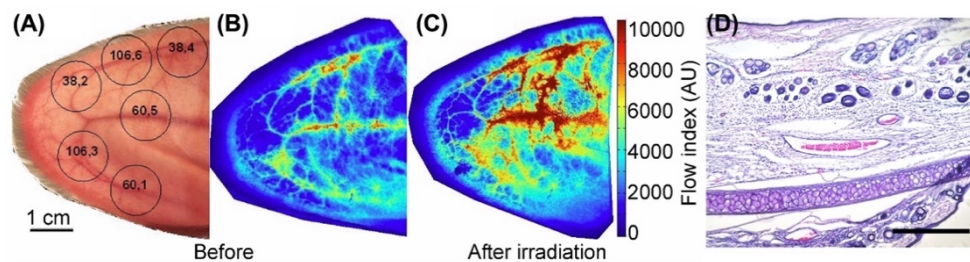
**Figure 5.4.** Color and LSC images of a rabbit earlobe before (A&B), and immediately after (C) 755 nm pulsed (3 ms) laser irradiation without injection of any agent. The first number on each circle in (A) represent the value of $D_o$ in J/cm$^2$ and the second number is the sequence of irradiation. (D) H&E stained section of rabbit earlobe at the highest $D_o$ (106 J/cm$^2$, site 3). Scale bar = 50 μm.
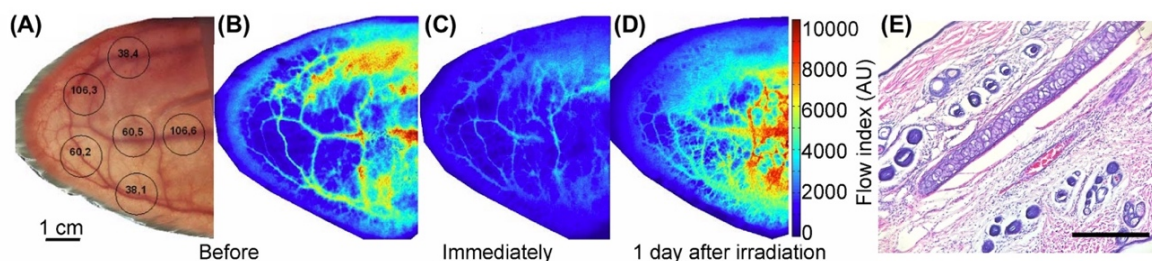


**Figure 5.5.** Color and LSC images of a rabbit earlobe before (A&B), immediately after (C), and one day (24hr) after (D) 755 nm pulsed (3 ms) laser irradiation in conjunction with 2 mg/mL free ICG. The first number on each circles in (A) represent the value of $D_o$ in J /cm$^2$ and the second number is the sequence of irradiation. Site 1-3 were irradiated at the time of maximum fluorescence emission intensity (~30s after ICG injection) and site 4-6 were irradiated 30 mins later. (E) representative H&E stained section of rabbit earlobe at the highest $D_o$ (106 J /cm$^2$, site 3). Scale bar = 50 μm.

Further, laser irradiation at lower $D_o$ =80 J/cm2 in conjunction with μNETs was accompanied by reduced blood perfusion immediately after irradiation (Figure 5.6A-D), and a complete cessation in blood flow on most of the irradiated sites one day later (Figures 5.6A-F). Evaluation of thermal injury is based on previous publications[201-202]. Our histology shows agglutination of individual RBCs (Figure 5.6G-I, yellow arrows) and breakage of basement membrane (Figure 5.6H-I, green arrows) upon laser irradiation in conjunction

with μNETs injection. As the complete photocoagulation of blood vessels, for example, the cessation of blood flow by formation of an occlusive coagulum is an indication of good clinical outcomes (i.e., lesional blanching)[203-204]. The formation of coagulum from our histological analysis and the complete halt in blood flow demonstrates a successful photothermal injuries induced by NIR laser irradiation at reduced radiant exposure ($D_o$ =80 J/cm2) in conjunction with μNETs administration.
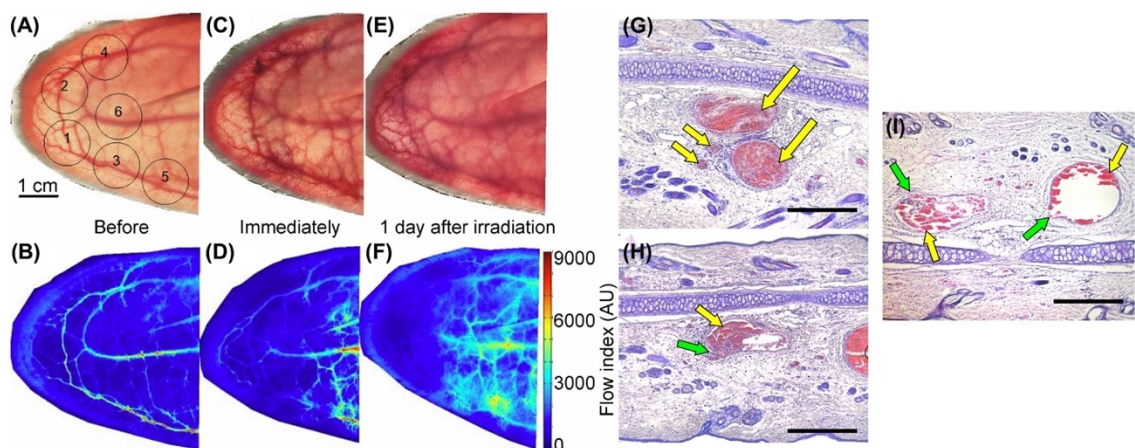


**Figure 5.6.** Color and LSC images of a rabbit earlobe before (A&B), immediately after (C&D), and one day (24hr) after (E&F) 755 nm pulsed (3 ms) laser irradiation with injection of μNETs. Site 1 was irradiated at the time of maximum fluorescence emission intensity (~30 s after injection of μNETs) and subsequent sites were irradiated every 5 mins. $D_o$ = 80 J /cm² for all sites. (G, F, I) representative H&E-stained sections of rabbit earlobe from site 1 and 2, respectively. Scale bar = 50 μm. Yellow arrow indicates agglutination of RBCs forming a coagulum and green arrow indicate the breakage of basement membrane.

## 5.5 Discussion

In this study, we have successfully demonstrated the effectiveness of erythrocyte-derived micro-particles contained with FDA-approved ICG as the photo-activated target to induce the photothermal destruction of blood vessels in rabbit earlobe upon pulsed 755 nm NIR laser irradiation at low radiant exposure ($D_o$ = 80 J/cm²). Additionally, the result is consistent with our previous study that administration of μNETs in combination with laser

irradiation (755nm) at lower fluence ($D_o$ = 20 and 30 J/cm$^2$) was sufficient to induce complete blood flow cessation and photocoagulation of mice microvasculature in the window chamber[45]. However, for the purpose of eventual translation from animal models to approved clinical applications[205], our study using rabbits as a larger animal model with vascular circulation dynamics more similar to humans than mice offers a more creditable evaluation of this approach.

Previously, Yaseen *et al* have demonstrated the effectiveness of photodynamic therapy (PDT) combining with photothermal therapy (PT) with ICG as a photosensitizer which yields greater amount of thermal damages to the blood vessels in rabbit earlobe than treated with either therapy alone[202]. As when without the pre-treatment of PDT, photothermal irradiation at 10 min post-injection of ICG did not produce sufficient heat to induce the thermal damages regardless of fluence due to ICG having fast clearance kinetics of ICG in rabbit. Not to mention that it has been reported that ICG has a disappearance rate of ~17.7-25.3 % per min from the bloodstream in humans[206-207], thus making it more challenging in clinical application of ICG with NIR laser irradiation as an effective PWS approach.

Nevertheless, in clinical settings, use of ICG with pulsed 808- and 810 nm NIR light for treating PWS patients has actually been reported[39, 192]. Despite the good clinical outcomes reported in these studies, introducing ICG-encapsulated erythrocyte-derived particles is advantageous than free ICG as it prolongs the circulation times of ICG which potentially extend the therapeutic window time during which laser irradiation is given. For example, red blood cell-membrane coated poly(lactic-co-glycolic acid) (PLGA)

nanoparticles showed elimination half-life to be 39.6 hr as compared to 15.8 hr for the PEG-coated particles[208]. Di *et al* have demonstrated the red blood cell camouflaged sodium microsensors present in the mice bloodstream for up to 2 weeks[209]. We previously reported that the emission half-life of the μNETs within the mice microvasculature to be ~49 min[45] and that μNETs were still detectable in mice blood 48 hr post-injection[127]. This long circulation time of erythrocyte-camouflaged particles can be ascribed to the natural protecting membrane proteins such as CD47, a glycoprotein that interacts with SIRPα on macrophages to suppress phagocytosis[210-211], thus preventing the elimination by immune cells[212] as we have also reported to be well-preserved on μNETs[14].

Additionally, our theoretical result also demonstrate the benefit of using μNETs with NIR laser irradiation including increased penetration of the light reaching to deeper blood vessels ( ~0.8-1mm below skin surface) and reduced risk of epidermal injury[10]. In conclusion, we have successfully demonstrated that pulsed 755 nm laser irradiation in conjunction with μNETs administration can induce photocoagulation of blood vessels accompanied with a complete blood flow cessation in rabbit earlobe vasculature at reduced fluence, which represents a potentially promising method for treatment of PWS. We are convinced that this potential approach is of great advantages such as longer circulation times of encapsulated ICG in bloodstream, deeper skin penetration and low melanin absorption at utilized NIR wavelength.

**Chapter 6: Optical Characteristics of Dual MRI and NIR dyes loaded Erythrocyte-derived Nanoparticles**

**6.1 Abstract**

Near-infrared (NIR) fluorescence image has gained increased popularity in biomedical applications. Indocyanine green (ICG) is presently the only FDA-approved NIR agent, however, studies on developing alternatives are still ongoing. For example, halogenated cyanine dyes, such as BrCy dyes, cyanine dyes with bromine incorporated into the aromatic component. Herein, we investigate the absorption and fluorescence characteristics of ICG and three brominated cyanine dyes including BrCy106-acid, BrCy111, and BrCy112 in free forms and evaluate the key optical properties once encapsulated into erythrocyte-derived nano-sized ghosts (nEGs). Our results indicate that when used at lower concentration of the dyes for encapsulation (100 μM), the spectrally integrated fluorescence emission for BrCy112-doped nEGs is ~3.6-4.7 times and ~40.8 times higher than that of BrCy106/111-nEGs and ICG-nEGs, respectively. Additionally, our results support efforts toward developing a novel carrier with dual-modality that can be used in NIR and magnetic resonance (MR) imaging. Thus, we further demonstrated the fabrication of erythrocyte-derived nanoparticles that were successfully doped with BrCy112 and gadolinium-based contrast dye (Gd) which showed stable NIR and MR signals up to 7 days. These findings provide a roadmap for the development of optical nanoparticles with enhanced NIR emission and that dual-BrCy112-Gd-nEGs may potentially be serve as effective material for dual-mode imaging applications.

**6.2 Introduction**

Fluorescence imaging using exogenous fluorescent materials has become a popular and fundamental tool to visualize cell or tissues for image-guided surgery and other biomedical applications[213-216]. In particular, when activated by near-infrared (NIR) light (~700-2500 nm), these materials provides relatively deeper optical penetration on the order of ~1-3 cm and higher resolution with the improved image contrast than visible light[188, 217-218]. These advantages are attributed to the diminished light absorption and scatterings by endogenous biomolecules as well as reduced autofluorescence within the NIR spectral bands[18, 188, 219]. One potential NIR fluorophore is indocyanine green (ICG), which remains as the only FDA approved NIR dye for utilization in humans in specific clinical applications such as ophthalmic angiography[220] and liver function assessment[221].

Despite ICG's usage in both clinical applications and investigative research[222-223], ICG still has down sides including its non-specificity, short half-life within plasma (~2-4 min) resulting in its elimination by hepatocytes, and relatively weak fluorescence emission as quantified by a low fluorescence quantum yield[224]. It is reported that the free form of ICG in water has relatively low fluorescence emission in response to 780 nm photoexcitation as quantified by a low fluorescence quantum yield (~2.58 ± 0.04% using 6.45μM of the dye)[225]. Hence, researchers are exploring into alternate or improved fluorophores for biological imaging[18, 226-228]. One such NIR chromophore is called brominated cyanine dyes, that were developed by introducing the halogen atoms such as Cl, Br, or I into the structure of the dye[229]. Previously, our lab has investigated the use of the BrCy106-NHS and reported the higher peak emission intensity values of free BrCy106-

NHS than that of free ICG (~27 times higher at the same concentration of 8 μg/mL)[230] due to the reduction in non-radiative relaxation pathways involving C-H vibrational modes which is caused by the presence of Br in place of aromatic structure. In this study, we further investigated characteristics of the three different brominated cyanine dyes, BrCy106 in acid form (referred to as BrCy106-acid), BrCy111, and BrCy112 (developed and manufactured by NanoQuantum Science) (structures of each dye are shown in figure 6.1).

Magnetic resonance imaging (MRI), another imaging modality, is widely utilized clinically for its great soft tissue contrast between normal tissues and lesions[19]. Particularly, gadobenate dimeglumine (Gd), a novel gadolinium-based contrast agent with greater relaxivity than other conventional gadolinium chelates[231], has been applied in evaluation of hepatic lesions[232], brain tumors[233-234], and central nervous system[235]. As such, combining the strengths of MRI and NIR imaging could potentially achieve the purpose of developing a great tool in obtaining the non-invasive image with high-contrast intrinsic properties of tumor lesions in clinical applications.

Besides, to address the issue related to non-specificity of free dyes, encapsulation into nanoparticles is an ideal solution as a protective shield to these dyes. We previously demonstrated the encapsulation of BrCy106-NHS or ICG into genome-depleted virus-mimicking nanoparticles, the tumor imaging capabilities of these particles[230] as well as functionalizing with human epidermal growth factor receptor 2 (HER2) for enhanced targeting to ovarian tumor[236]. Nevertheless, mammalian cells, particularly erythrocytes, are an emerging type of platforms with naturally long circulation capacity for the delivery of

94

therapeutic or imaging agents[1, 237-238]. Our lab has previously reported the first successful engineering of nano-sized particles derived from erythrocytes doped with ICG for fluorescence imaging and photothermal destruction of cells[9]. Hence, we applied the idea of encapsulating these dyes into erythrocyte-derived nanoparticles here.

Taken together, we aim to achieve three objectives in this study. First, we compare the optical characteristics of three BrCy dyes and ICG in non-encapsulated form for baseline information. Second, we extend these characterizations to BrCy or ICG encapsulated erythrocyte-derived nanoparticles. In particular, we investigated the effect of various dye concentrations used in fabrication of the dye encapsulated nanoparticles and the resulting absorption and fluorescence characteristics. Results of such characterizations provided the basis for selecting the candidate dye and an optimized concentration of the dye which equips with relative high fluorescence emission. Lastly, we demonstrated that both Gd and BrCy112 can be dually loaded into erythrocyte-derived nanoparticles which present both the NIR and MRI characteristics stably up to 7 days. To the best of our knowledge, we report for the first time the comparisons in optical properties of BrCy106-acid, BrCy111, and BrCy112 to ICG in their free and encapsulated forms and the demonstration of successfully fabricating the erythrocytes-derived nanoparticles incorporating both MR and NIR agents. Our findings in this study offer useful guidance toward developing erythrocyte-derived particles containing both MR and NIR agents which can be potentially utilized for dual mode imaging capability of tumors including ovarian intraperitoneal tumors in future.
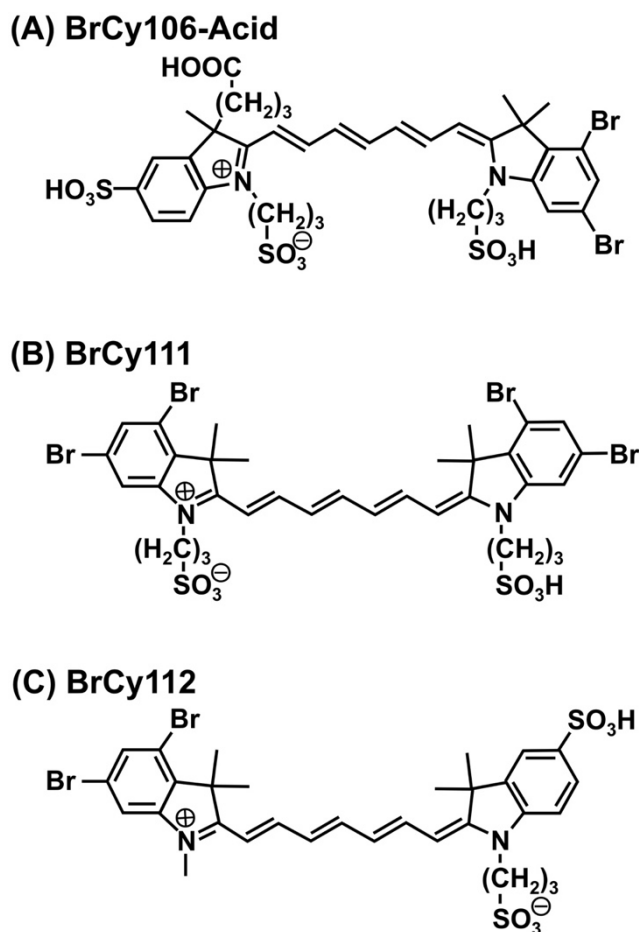
**Figure 6.1.** Molecular Structure of (A) BrCy106-Acid, (B) BrCy111, and (C) BrCy112

## 6.3 Material and Methods

### 6.3.1 Fabrication of Variant Brominated Cyanine Dyes-nEGs and ICG-nEGs

Erythrocytes were isolated from whole human blood (BioIVT, Westbury, NY) and washed three times in isotonic (~320 mOsm) phosphate-buffered saline (PBS; referred to as the 1X PBS solution, Fisher Scientific, Hampton, NH) at 1000$g$ for 10 mins at 4°C. Isolated erythrocytes were incubated with hypotonic PBS (~80 mOsm, 0.25X PBS) at 4°C for 1 hour, followed by centrifugation at 20,000$g$ for 20 mins at 4°C. The resulting micro-sized

erythrocyte ghosts (µEGs) were resuspended in 1X PBS. To obtain the nano-sized EGs (nEGs), µEGs were then diluted 1:10 in 1X PBS prior to extrusion process. The diluted µEGs were extruded three times individually through 800nm, 400nm and 200nm polycarbonate porous filters (Sterlitech Corp., Kent, WA) using a 10 mL automatic LIPEX® extruder (TRANSFERRA Nanosciences Inc., Burnaby, B.C., Canada). The resulting nEGs were then centrifuged at 100,000g for 1 hour at 4°C and resuspended in 1X PBS.

Three brominated cyanine dyes (BrCy106-Acid, BrCy111, BrCy112; NanoQuantum Sciences, Bellevue, WA) and a near-infrared dye (ICG; MP Biochemicals, Santa Ana, CA) were used to load into nEGs individually. Triplicate samples were prepared for each dye. We followed a 1:1:1 volume ratio of mixing nEGs, Sørensen's phosphate buffer ($Na_2HPO_4/NaH_2PO_4$, ~140 mOsm, pH ~ 8), and a known concentration of the chromophore. We applied three different final concentrations of each dye in the loading buffer (100, 750 1000 µM) and incubated nEGs with indicated loading buffer at 4°C for 30 mins to form BrCy106-nEGs, BrCy111-nEGs, BrCy112-nEG or ICG-nEGs. The resulting pellets were then washed twice in 1X PBS and centrifuged at 100,000g for 1 hour at 4°C to remove excess unencapsulated dyes.

### 6.3.2 Fabrication of Gd-BrCy112-nEGs

To dually load gadobenate dimeglumine (Gd; Bracco Diagnostics Inc., Princeton, NJ) and BrCy112 into the nEGs, we incubated the nEGs in hypotonic solution containing both agents using 1:1:1:1 volume ratio of nEGs, Sorensen's phosphate buffer, Gd (final concentration of 125mM) and BrCy112 (final concentration of 100µM). The solution was

then incubated for 30 min at 4°C, followed by washing in 1X PBS twice. The resulting pellets were resuspended in 1X PBS and defined as Gd-BrCy112-nEGs.

### 6.3.3 Characterization of Particles

The hydrodynamic diameters of all particles suspended in 1X PBS were measured by dynamic light scattering (DLS) (Zetasizer nanoseries, NanoZS90, Malvern, UK). Three individual measurements were collected for each sample and averaged to estimate the mean diameter and standard deviation (SD) by LogNormal fitting. The zeta potentials (Zetasizer nanoseries, NanoZS90, Malvern, UK) of all particles in 1X PBS were measured using folded capillary cells. Five measurements were collected for each sample and averaged to determine the mean zeta potential for each sample population.

Absorption spectra of all particles and free dyes in 1X PBS were recorded in the spectral range of 280-1000nm using a visible spectrophotometer (Jaco V-670 UV-vis spectrophotometer, JASCO) with an optical path length of 1 cm. Fluorescence emission spectra of all particles suspended in 1X PBS in response to photoexcitation at $750 \pm 2.5$ nm (for BrCy-loaded nEGs) and $780 \pm 2.5$ nm (for ICG-loaded nEGs) filtered from a 450 W xenon lamp were acquired using a fluorometer (Fluorolog-3 spectrofluorometer, Edison). Normalized fluorescence emission spectra $\chi(\lambda)$ were defined as follows

$$\chi(\lambda) = \frac{F(\lambda)}{1-10^{-A(\lambda ex)}} \tag{6}$$

Where F is the fluorescence emission intensity in response to the excitation wavelength ($\lambda_{ex}$) and A ($\lambda_{ex}$) is the absorbance of the sample at the excitation wavelength. To estimate the total fluorescence emission for each sample, we integrated the fluorescence

emission over a desired spectral bands in the range of 765-900 nm (for BrCy-loaded nEGs) and 795-900 nm (for ICG-nEGs).

## 6.3.4 Quantification of Gd and BrCy Dyes Loading Efficiency of nEGs

To quantify the loading efficiency of Gd, we obtained the MRI images of the particles and the supernatant collected upon completing the fabrication of Gd-BrCy112-nEGs. We created a phantom containing vials with different concentrations of the Gd and measured the T1 relaxation rate (R1) as a function of concentration. The slope of the T1 value vs concentration curve was used to estimate the concentration of the Gd in MRI images. For BrCy or ICG loading efficiency, we used a similar methodology as in our previously reported study[123] and are not repeating here.

## 6.3.5 Assessment of Dye Leakage From Gd-BrCy112-nEGs

Upon completion of fabricating the Gd-BrCy112-nEGs, the suspension containing the particles were stored at 4°C. At specific times (0, 2, 7 days), approximately 1.3 mL of particle suspension was centrifuged, and the pellet was resuspended in the original volume of 1X PBS. We recorded the absorption and fluorescence emission spectra of the resuspended pellet and supernatant to determine BrCy112 leakage. We measured the T1-values of samples to determine Gd leakage. Three measurements were obtained for each time point and averaged to determine the mean R1 value.

## 6.3.6 Magnetic Resonance Imaging

MRI imaging was performed on a 3T Siemens Prisma. The T1-values of the contrast agent were measured with a spin echo based inversion recovery experiment (repetition time = 5000 ms; echo time = 15 ms, field of view=210 mm x 72 mm, matrix size = 256 x 88).

Inversion times ($T_I$) of 30 ms, 100 ms, 400 ms, 1000 ms, 2000 ms, 3000 ms, 4000 ms, and 4900 ms. T1 values were calculated voxelwise by fitting the resulting signal curve with the following function

$$S(t) = A - Bexp(-T_I / T_1) \tag{7}$$

## 6.4 Results and Discussion

### 6.4.1 Absorption and Fluorescence Characteristics of Free Dyes

Absorption spectra of free BrCy dyes and ICG using three different concentrations (100, 750, and 1000 μM) dissolved in 1XPBS are shown in Figure 6.2. Absorption spectra of free BrCy106-Acid dissolved in 1XPBS showed a narrow distinct spectral peak at ~750 nm (Figure 6.2A) similar to that found in absorption spectra of free BrCy112 (Figure 6.2C) which could be associated with the monomeric form of the dye[230]. However, free BrCy111 dissolved in 1XPSB showed a broadened absorption range in addition to two distinct peaks at ~643 nm and 850 nm with increased concentrations from 100 to 1000 μM (Figure 6.2B), which suggests that this dye may be more prone to aggregation than BrCy106 and BrCy112. Absorption spectra of free ICG dissolved in 1XPBS showed bimodal spectral peaks at ~706 nm and 780 nm corresponding to the H-like aggregate and the monomeric forms of ICG, respectively[9, 123]. Particularly, the tendency of ICG molecules to aggregate at high concentrations is suggested by the increasing absorbance at 706 nm with greater ICG concentrations (Figure 6.2D)[239-240]. Overall, We observed that whereas BrCy106-Acid's absorption spectra are similar to those of BrCy112, BrCy106-Acid displayed higher absorbance at 750 nm than BrCy112 and BrCy111. All of the BrCy dyes exhibited spectral

peaks in the NIR range similar to ICG, but had increased absorbance at their spectral peak wavelengths.
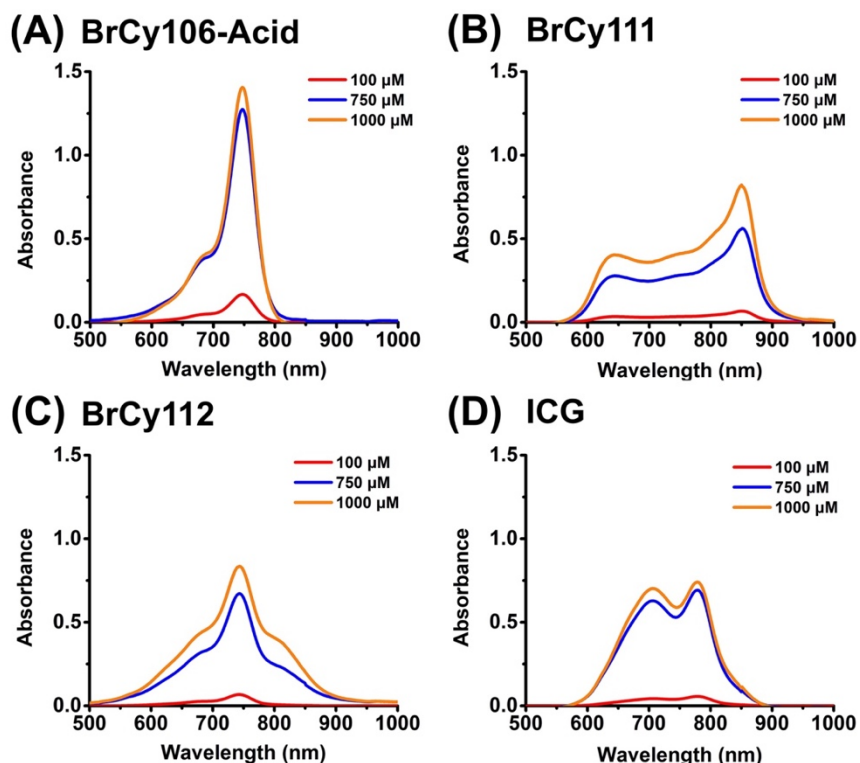


**Figure 6.2.** Concentration-dependent absorption spectra of (A) BrCy106-Acid, (B) BrCy111, (C) BrCy112, and (D) ICG in 1X PBS.

In response to photoexcitation of free BrCy dyes at 750 ± 2.5 nm and ICG at 780 ± 2.5 nm, free BrCy106-Acid and BrCy112 exhibited similar fluorescence emission characteristics as quantified by the normalized fluorescence intensities (Figure 6.3A&E) and produced greatest spectrally integrated emission when used at a concentration of 750 μM (Figure 6.3B&F). The fluorescence spectral analysis of free BrCy111 dissolved in 1XPBS showed that the greatest emissive energy (spectrally-integrated emission) is achieved when used at low concentrations of 100 μM (Figure 6.3C&D). The spectrally integrated emission of free ICG over 795-900 nm bands was also maximal at low

concentrations of 100 μM (Figure 6.3G&H). Particularly, we observed that both free BrCy111 and ICG displayed gradually decreased integrated emission as the concentration of free dye increased, suggesting the quenching of emission induced by aggregation of the free dyes at higher concentrations[224, 241-242].

In addition, at a low concentration of 100 μM, both free BrCy106 and BrCy1112 showed the highest integrated NIR emission than BrCy111 and ICG. The integrated emission of free BrCy106 at 100 μM was ~42 times and ~14 times higher than that of BrCy111 and ICG at the same concentrations, respectively, while the integrated emission of free BrCy112 at 100 μM was ~33 times and ~11 times higher. We observed that the free BrCy106 and BrCy112 have only 1.2-fold differences in their integrated NIR emission at low concentrations (Figure 6.3B&F). Therefore, we suggest that both dyes showed similar NIR emission characteristics at low concentrations and higher emissive energy than BrCy111 and ICG. The enhanced fluorescence emission of the BrCy106 and BrCy112 can be attributed to the presence of the bromine in the aromatic ring, which reduces non-radiative decay pathways involving C-H vibrational modes as described in previously published literature[230]. However, the lower fluorescence emission of free BrCy111 might be associated with aggregation-induced fluorescent quenching or the extra two bromine atoms induced a heavy atom effect that enhances the intersystem crossing in comparison to BrCy106 and BrCy112[243].
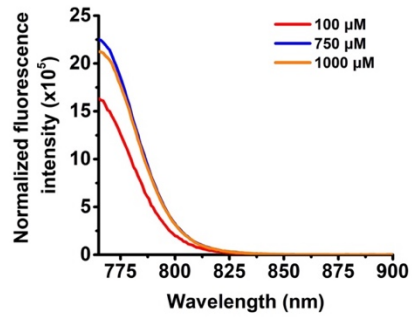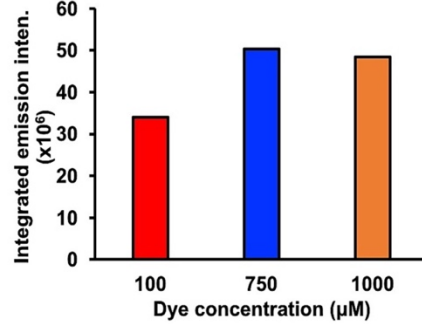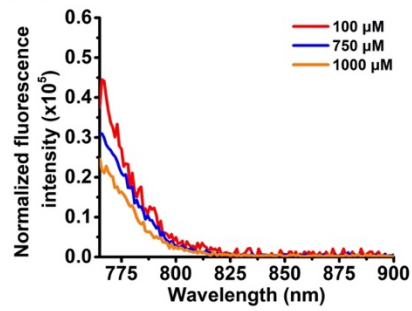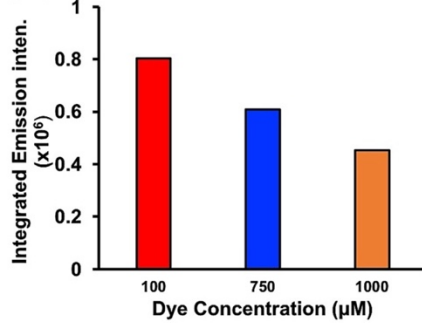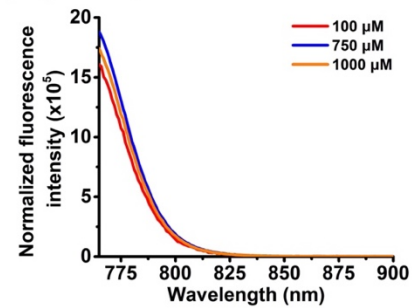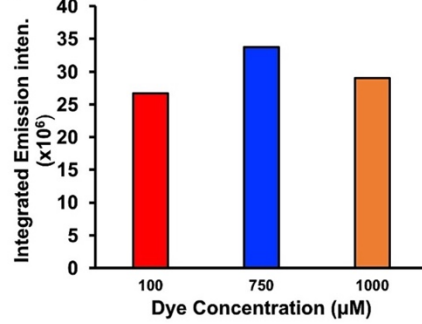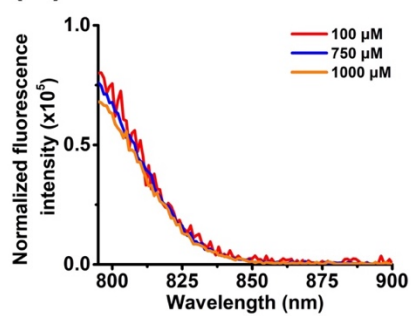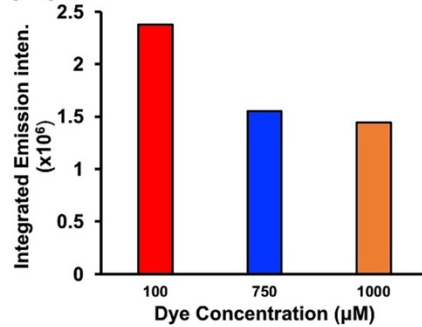
**Figure 6.3.** (A-D) Normalized fluorescence emission spectra of free BrCy106-Acid (A), BrCy111(B), BrCy112(C), and ICG(D) in 1X PBS in response to photoexcitation wavelengths of $750 \pm 2.5$ nm and $780 \pm 2.5$ nm. (E-H) Emission intensities integrated over the 765-900 spectral band for BrCy-variants (excited at 750 nm) and 795-900 spectral band for ICG (excited at 780 nm).

### 6.4.2 Optical Characteristics of BrCy or ICG-encapsulated Nanosized EGs

We used the same three concentrations (100, 750, 1000 μM) of each dyes to load into the nEGs. The physical characteristics of each construct were illustrated in the supplemental table. As determined by fitting lognormal distribution to DLS-based measurement, the averaged hydrodynamic diameter of the various constructs were in the range of approximately 85-137 nm. However, BrCy111-nEGs fabricated using 1000 μM showed increased mean diameters of $731 \pm 15.1$ nm, indicating that the dye is more likely to form aggregates at high concentrations. Zeta potentials of BrCy106-, BrCy112-, and ICG-loaded nEGs using three concentrations were in the range of -12.79 to -14.43 mV which were similar to that of non-encapsulated nEGs ($-13.68 \pm 0.28$ mV) or untreated RBCs ($-13.7 \pm 0.93$ mV). Except for BrCy111-nEGs fabricated using 100 μM of the dye, the respective zeta potentials of BrCy111-nEGs fabricated using 750 and 1000 μM of the dye were $-22.34 \pm 0.05$ and $-25.25 \pm 0.89$ mV which were significantly lower than those from other constructs, nEGs, and untreated RBCs. These results suggest that BrCy111 when used at higher concentrations, particularly over 750 μM, are not fully encapsulated within the nEGs and the negative regions contributing from the sulfur group of the dye may be protruding out of the membrane of the nEGs and exposed to the aqueous environment.

We also estimated the loading efficiency of each dye into nEGs using the same method as in previously published literature[123]. For BrCy111-, BrCy112-, and ICG-nEGs, there was an increase in loading efficiency as the concentration of the dye increased (Table S6.1). The averaged loading efficiency for BrCy106-, BrCy112-, and ICG-nEGs were ranged between ~47 to 70%. However, the highest loading efficiency of these three

constructs is still lower than that of BrCy111-nEGs even when a high concentration at 1000 µM was used. The loading efficiency of BrCy111 is in the range of ~79 to 95% which is higher than the other constructs when used in concentrations of 100-1000 µM. We suggest that it could be attributed to its being more hydrophobic than BrCy106 or BrCy112 while supposedly having similar optical performance. With our finding of much lower negative zeta potentials of this construct, our results here also imply that this dye might be densely packed and overcrowds the membrane of the nEGs, presumably leading to conformations where the negative sections are exposed.

Absorption spectra of nEGs doped with various dyes suspended in 1XPBS are shown in figure 6.4. Value of absorbance at 280 nm for all the constructs originated from the aromatic amino acids of the protein such as tyrosine and tryptophan[135, 244-245]. We observed that the absorbance at 280 nm was almost the same at ~1 for all constructs, indicating that each construct contained approximately the same number of particles for comparison. We noticed that all constructs exhibited the same trends in their absorption spectra as the non-encapsulated dyes (Figure 6.2). The absorption spectra of BrCy106-nEGs began to visibly show spectral peaks at 750 nm when used at a high concentration of 1000 µM (Figure 6.4A). However, BrCy112-nEGs showed a noticeable spectral peak at ~750 nm with gradually increased absorbance as the concentration of the dye used in fabrication increased. In addition, we found that the BrCy111-nEGs utilized with 100–1000 µM of the dye have a broadened absorption range with two distinct spectral peaks as found in that of free dye (Figure 6.4B), which indicates that a significant fraction of the dye may have been in aggregated form when encapsulated. As for ICG-nEGs, we observed

the red-shift of the peaks from 780 to 804 nm which is consistent with our previous studies[9, 14, 123, 126], indicative of the monomeric form of ICG.
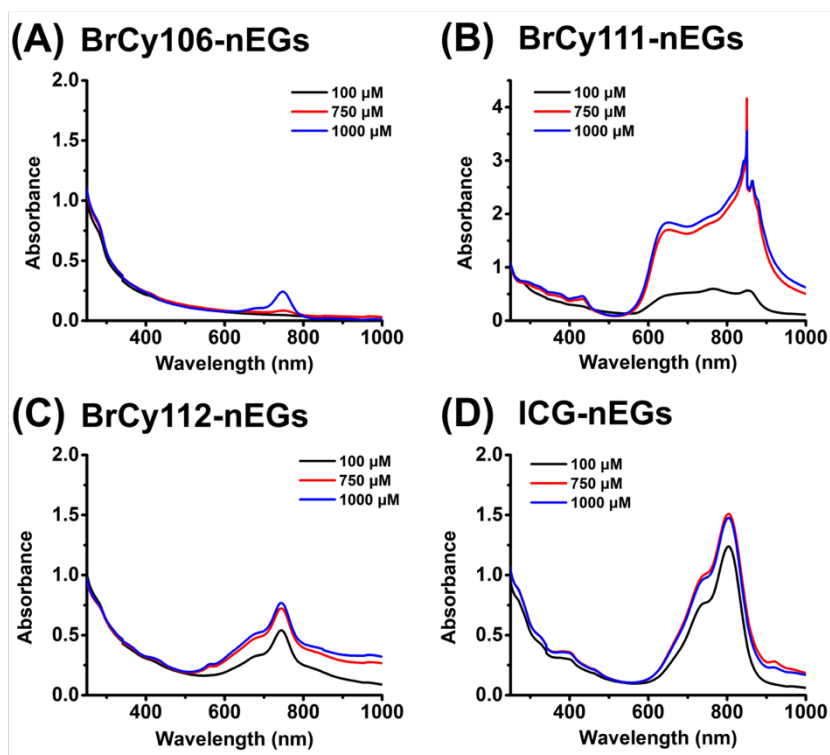


**Figure 6.4.** Absorption spectra of BrCy-variants and ICG loaded nEGs. Absorption spectra of: (A) BrCy106-nEGs, (B) BrCy111-nEGs, (C) BrCy112-nEGs, and (D) ICG-nEGs suspended in 1X PBS. Particles were encapsulated using various loading concentrations of the agent ranging from 100~1000 μM.

In response to photoexcitation at 750 ± 2.5 nm for BrCy-nEGs and 780 ± 2.5 nm for ICG-nEGs, we observed identical trends among BrCy111-nEGs, BrCy112-nEGs, and ICG-nEGs in their fluorescence emission (Figure 6.5A-D). For example, particles fabricated using the lowest concentration (100 μM) showed the highest normalized fluorescence and spectrally integrated emission. However, the emissive energy of BrCy111-nEGs and ICG-nEGs, which were fabricated using the lowest concentration of the dye (100 μM), was still ~1.3- and 11.2-fold lower than that of BrCy106-nEGs and ~4.7-

and 40.8-fold lower than that of BrCy112-nEGs, respectively (Figure 6.5E). Among the

three dye concentrations applied in encapsulation, BrCy106-nEGs fabricated using 1000

μM of the dye produced the most emissive fluorescence, whereas BrCy112-nEGs

fabricated using 100 μM of the dye exhibited the highest emissive fluorescence. However,

there is only ~1.2-fold difference in their emissive fluorescence. These results suggest that

high concentrations of BrCy106 (1000 μM) are needed to obtain high emissive energy, but

low concentrations of BrCy112 (100 μM) can reach a similar emissive energy. Therefore,

we decided to use BrCy112 with 100 μM to dually load with Gd.
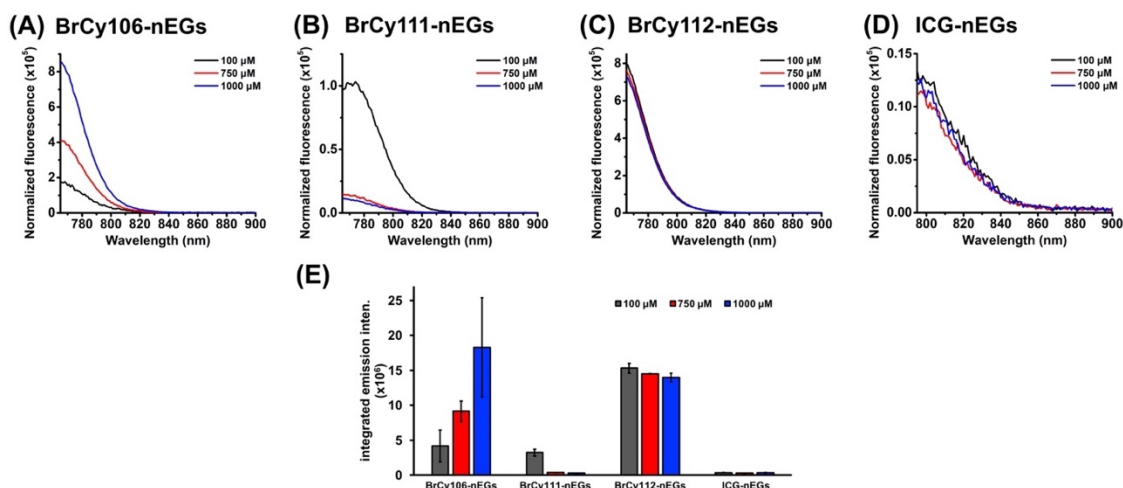


**Figure 6.5.** Normalized fluorescence emission spectra of BrCy-variant or ICG-loaded nEGs. (A-C) Normalized fluorescence emission spectra of BrCy106-nEGs, BrCy111-nEGs, and BrCy112-nEGs in response to photoexcitation at $750 \pm 2.5$ nm. (D) Normalized fluorescence emission spectra of ICG-nEGs in response of photoexcitation at $780 \pm 2.5$ nm. (E) Spectrally integrated fluorescence values in the range of 795-900 nm for BrCy-variant nEGs and 795-900 nm for ICG-nEGs. Each bar is an average of three independent measurements with SD values (error bar).

### 6.4.3 Dual-Encapsulation of NIR and MRI Agent

To combine the strengths of NIR and MRI, we demonstrated here the dually loaded human-

derived nEGs with both the BrCy112 and Gd. The hydrodynamic diameters of non-

encapsulated nEGs and Gd-BrCy112-nEGs were ~129 ± 0.68 and 131.42 ± 1.05 nm as determined by the DLS technique, respectively (Figure S6.1A). Zeta potential of Gd-BrCy112-nEGs was -16.03 ± 0.93 mV which is indistinguishable from the untreated nEGs (-14.53 ± 0.21mV) and RBCs (-15.17 ± 0.38mV) (Figure S6.1B). These results suggest that sialoglycoproteins, the primary components of the negative charge of the RBC membrane, are still preserved after encapsulating BrCy112 and Gd dyes into nEGs.

Illustrative optical characteristics of Gd-BrCy112-nEGs are shown in figure 6.6. We estimated the loading efficiency of each dye into nEGs as 95.15% for BrCy112 and 33.59% for Gd. We notice that the BrCy112 somehow had higher loading efficiency into nEGs when co-loaded with Gd than solely loaded into nEGs. In figure 6.6A, we present the absorption spectra of Gd-BrCy112-nEGs collected upon completion of fabrication (sample name shown as day 0). The NIR spectral peak at 750 nm was presented, suggesting the successful encapsulation of BrCy112. We also validated the NIR fluorescence in response to photoexcitation at 750 ± 2.5 nm (Figure 6.6B&C). Interestingly, we noticed that the absorbance at 750 nm and the spectrally integrated emission for Gd-BrCy112-nEGs is higher than those of BrCy112-nEGs fabricated using the same concentration of the dye (100 μM). We attribute it to the higher loading efficiency of the BrCy112 into nEGs when co-loaded with Gd in this case.

In figure 6.6D&E, we present the T1 relaxation rate (R1) and the contrast intensities of phantom images of Gd-BrCy112-nEGs obtained at three different time points with various dilution ratios. We estimated that ~42 mM of Gd was successfully loaded into nEGs.

**6.4.4 Stability of Gd-BrCy112-nEGs**

There is no agglomeration with no significant changes in size distribution (Figure S6.1A) and alteration of zeta potential of the particles over a week period (Figure S6.1B), suggesting that the particles are physically stable up to a week. After 2 days of storage at 4°C, an initial leak of BrCy112 was only 2.3% as compared to samples collected upon completion of fabrication (day 0), indicating that the leak from particles is nearly undetectable. Samples of Gd-BrCy112-nEGs collected at different time points also exhibited similar and not significantly different  fluorescence emission characteristics as quantified by the normalized fluorescence intensities (Figure 6.6B) and the spectrally integrated emission intensities (Figure 6.6C), further indicating that no leak of BrCy112 was seen. As for Gd, T1 relaxation rates of the particles after 7 days of storage at 4°C were similar to that of particles at day 0, indicating that there is no leak of Gd ($< 1\%$) up to a week (Figure 6.6D). The MR signals were consistent from day 0 to day 7, as evidenced by the contrast phantom pictures in figure 6.6E. These results suggest that the particles are stable for at least 7 days when stored at 4°C. This is consistent with our previous study that the RBC-derived nEGs doped with ICG showed fluorescently stable after 12 hours of storage at 4°C[123] and up to 8 days for micron-sized EGs doped with ICG[14]. However, further study of leakage at physiological temperature is needed to determine its in-vivo stability.
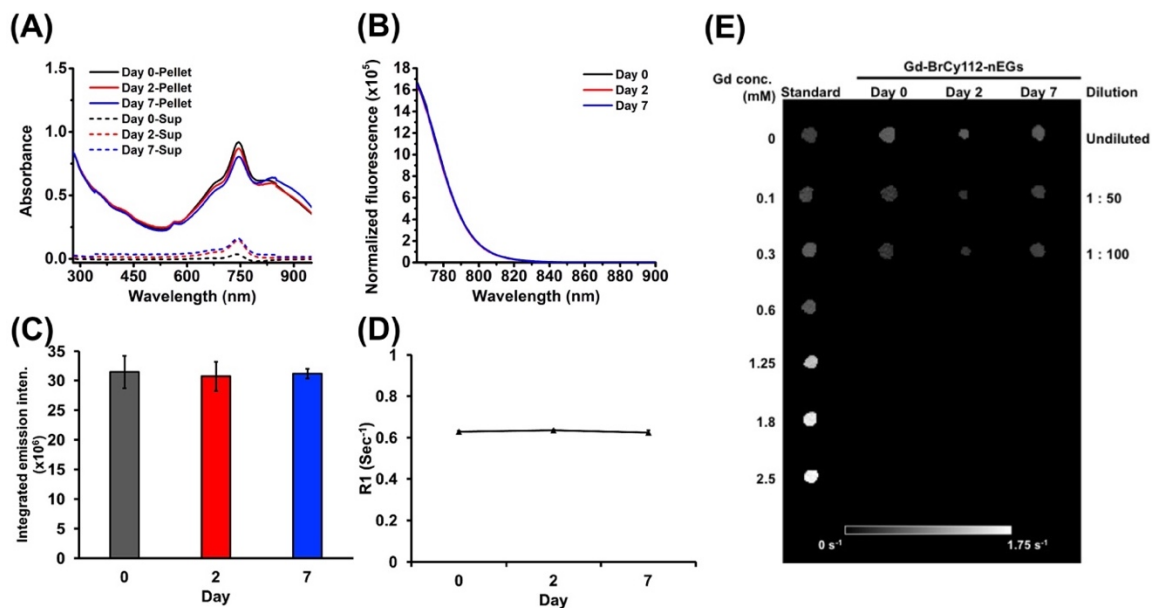
**Figure 6.6.** Characteristic and stability study of Gd-BrCy112-nEGs. (A) Time-dependent absorption spectra of Gd-BrCy112-nEGs and their corresponding supernatants. (B) Normalized fluorescence emission spectra and (C) Spectrally integrated fluorescence values over the 765-900 nm band in response to photoexcitation at $750 \pm 2.5$ nm. (D) $T_1$ relaxation rate (R1) of Gd-BrCy112-nEGs. Dilutions of samples from three different days were measured by MR imaging. Each data is an average of three independent measurements with SD values (error bars). (E) Representative phantom images of Gd-BrCy112-nEGs collected at day0, day2, and day7.

## 6.5 Conclusion

To the best of our knowledge, we have demonstrated for the first time the fabrication of erythrocyte-derived nanoparticles containing BrCy dyes, and dual encapsulation with MRI agent (Gadobenate dimeglumine) for future utilization in visualizing tumors via MR and NIR imaging. We have characterized the absorption and fluorescence properties of three BrCy dyes and ICG in free forms and after encapsulated in erythrocyte-derived nanoparticles. In free form and at the same concentration levels, BrCy dyes have overall greater emissive energy than ICG. After encapsulation, our results indicate that the spectrally integrated emission for BrCy106-nEGs and BrCy112-nEGs are greater than

those of BrCy111-nEGs or ICG-nEGs. We conclude that high concentration of BrCy106 is needed for encapsulation to obtain high emissive energy while BrCy112 only requires a low concentration to achieve efficient emissive energy. We also show that Gd and BrCy112 can be dually loaded into human RBC-derived nanoparticles successfully and that their NIR and MR characteristics remain stable at 4°C up to a week.

## 6.6 Supporting Information

### 6.6.1 Supporting Table

**Table S6.1.** Physical characteristics of various BrCy dye loaded nEGs collected upon completion of fabrication.

| Sample | Loaded dye concentration ($\mu$M) | Size (nm) | ZP (mV) | Loading Efficiency (%) |
|---|---|---|---|---|
| nEGs | - | 142.96 ± 0.527 | -13.68 ± 0.28 | - |
| BrCy106 | 100 | 136.58 ± 0.817 | -13.42 ± 0.42 | 50.19 ± 0.1 |
| | 750 | 122.71 ± 0.747 | -12.79 ± 0.75 | 46.75 ± 19.02 |
| | 1000 | 107.37 ± 0.542 | -13.33 ± 0.37 | 69.08 ± 2.06 |
| BrCy111 | 100 | 124.06 ± 0.717 | -14.50 ± 0.63 | 78.72 ± 4.82 |
| | 750 | 121.47 ± 1.78 | -22.34 ± 0.05*** | 95.35 ± 1.25 |
| | 1000 | 731.01 ± 15.1 | -25.25 ± 0.89*** | 95.38 ± 1.53 |
| BrCy112 | 100 | 97.944 ± 0.587 | -14.13 ± 0.25 | 41.82 ± 4.09 |
| | 750 | 84.363 ± 0.37 | -13.95 ± 0.46 | 55.54 ± 4.47 |
| | 1000 | 97.494 ± 0.55 | -14.23 ± 0.07 | 56.49 ± 4.77 |
| ICG | 100 | 124.03 ± 0.665 | -14.42 ± 0.38 | 53.53 ± 4.06 |
| | 750 | 123.24 ± 0.701 | -14.31 ± 0.41 | 54.27 ± 2.73 |
| | 1000 | 122.58 ± 0.565 | -14.00 ± 0.34 | 54.83 ± 4.51 |

Asterisks denote significant differences between sample and the untreated normal RBCs with *** corresponding to $p < 0.001$.

## 6.6.2 Supporting Figure
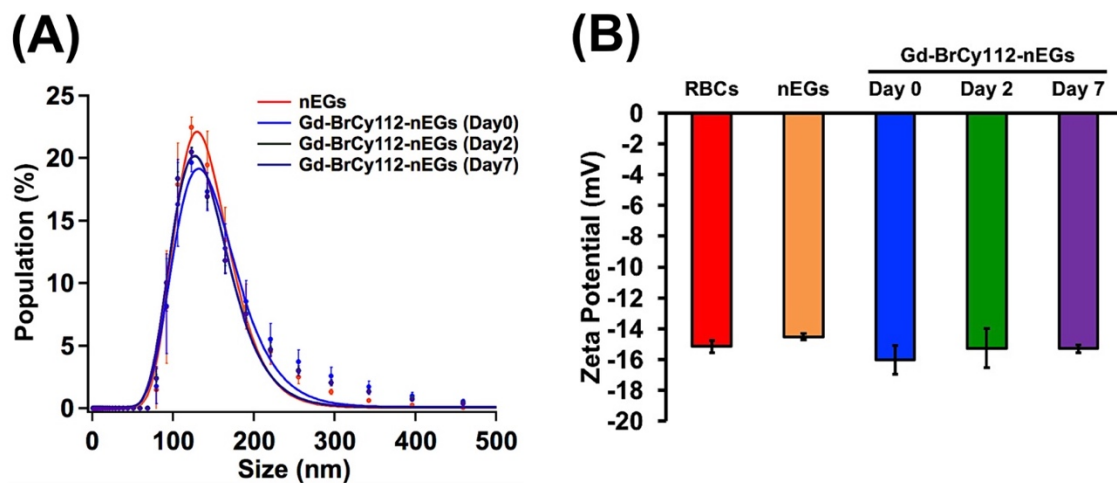


**Figure S6.1.** Physical characterization of RBCs, nEGs, and Gd-BrCy112-nEGs at 4°C (A) Hydrodynamic diameters and (B) Zeta potential of each particles. Suspensions were in 1XPBS and measurements were made by DLS. We present the average of three individual measurements on each of the samples with SD values (error bars). We fitted Lognormal function to the measured diameter distribution.

**Chapter 7: Conclusions**

The primary goal of this study aimed at optimizing the erythrocyte-derived carrier platforms and evaluating the capability of these carriers in biomedical applications. To design suitable RBC-derived carriers for clinical application, it is vital to comprehend their proteome, particularly the proteins involved in mediating the immune response and the mechanical properties of the carriers as they are relevant to the longevity of the particles. As such, we first analyzed the proteomes of μEGs$^{+ICG}$, nEGs$^{+ICG}$, and their native RBCs in chapter 2. We suggest that the protein compositions of μEGs$^{+ICG}$ was generally similar to that of RBCs, but there were still 8 proteins with significantly different relative abundance in μEGs$^{+ICG}$ as compared to RBCs. The proteomes of nEGs$^{+ICG}$, however, showed lower abundance levels of some structural proteins and additional differences in their protein compositions such as CD47, CD55, and CD44 as compared to μEGs$^{+ICG}$ and RBCs. Our findings highlight the importance of methods in engineering RBC-derived carrier systems with appropriate proteomes for clinical translation.

As we emphasized the importance of fabrication methods for these RBC-derived carriers from a proteomic standpoint, a common method for encapsulating different cargoes into RBC-derived platforms, such as hypotonic treatment of RBCs, results in PS exposure on the outer leaflet of the particles. This PS exposure serves as a signal for phagocytic removal of the particles from the circulation. In chapter 3, we demonstrated the effectiveness of enriching membrane cholesterol of RBC-derived microparticles in reducing the PS externalization and thus, phagocytic uptake by murine macrophages of these particles in vitro. When injected into healthy mice, we observed that ~94% ID/g of

C$^+$-μNETs were remained in the body while ~43% ID/g of μNETs were eliminated or metabolized at 24 hr post-injection. These results suggest that membrane cholesterol enrichment can be an effective method in prolonging the longevity of the particles in circulation.

In addition, we investigated the effectiveness of enriching the membrane cholesterol content of nano-sized NETs, and further functionalized with folate on biodistribution of these particles in organs and tumors of immunodeficient mice implanted with intraperitoneal SKOV3 ovarian cancer cells. At 24hr post-injection of particles, there was a greater NIR fluorescence emission intensity in tumors associated with administration of F-C$^+$nNETs as compared to other particles. This clearly illustrate that cholesterol enrichment of nNETs in combination with folate functionalization can result in greater accumulation in tumors, providing a potential capability for enhanced NIR imaging of tumors. While our attention has been on improving nNETs by enriching membrane cholesterol and functionalizing with folate to lower their risk of phagocytic clearance and to provide them with targeting abilities in vivo for fluorescent imaging of tumors, assessing the capability of nNETs in other application is needed to fully explore their potentials.

Hence, we evaluate the capability of NETs in mediating photothermal destruction of cutaneous vasculature in the rabbit earlobe as a model system for port wine stains(PWS) in chapter 5. Based on the LSC images, we observed that laser irradiation at reduced fluence ($D_o = 80$ J/cm$^2$) in conjunction with μNETs injection results in the reduced blood perfusion immediately after irradiation and a complete halt of blood flow on most of irradiate sites one day later. Further, our histological analysis also demonstrated the

photothermal damages including agglutination of RBCs and breakage of basement membranes upon laser irradiation with µNETs injection. Our results successfully demonstrated that pulsed 755 nm laser irradiation at reduced radiant exposure combining µNETs administration results in a complete blood flow cessation in rabbit earlobe vasculature, indicating a potentially promising method for treatment of PWS.

Finally, in the sixth chapter, we continue to explore the potential of RBC-derived platforms. We demonstrated the engineering and characterization of dual NIR (BrCy) and MRI (Gd) dyes loaded RBC-derived nanoparticles. Our optical measurements of various BrCy dyes and ICG in free form suggest that BrCy dyes has overall greater emissive energy than ICG. BrCy106-nEGs and BrCy112-nEGs have the greatest spectrally integrated emission than other particles. However, high concentration of BrCy106 is needed for encapsulation while BrCy112 only requires low concentration to achieve such efficient emissive energy. Furthermore, we also showed the successful dual loading of Gd and BrCy112 into RBC-derived nanoparticles as well as the stability of their NIR and MR characteristics at 4°C for up to a week.

Taken together, these findings underline the promise of improving and assessing the capabilities of RBC-derived carriers in imaging and therapeutic applications. Future studies on top of this work is essential to further optimize and greatly expand the potential of RBC-derived platforms in clinical applications.

**Reference:**

1.  Vincy, A.; Mazumder, S.; Banerjee, I.; Hwang, K. C.; Vankayala, R., Recent Progress in Red Blood Cells-Derived Particles as Novel Bioinspired Drug Delivery Systems: Challenges and Strategies for Clinical Translation. *Front Chem* **2022,** *10*.

2.  Hanley, T.; Vankayala, R.; Lee, C. H.; Tang, J. C.; Burns, J. M.; Anvari, B., Phototheranostics Using Erythrocyte-Based Particles. *Biomolecules* **2021,** *11* (5).

3.  Malhotra, S.; Dumoga, S.; Singh, N., Red blood cells membrane-derived nanoparticles: Applications and key challenges in their clinical translation. *Wiley Interdiscip Rev Nanomed Nanobiotechnol* **2022,** *14* (3), e1776.

4.  Flower, R.; Peiretti, E.; Magnani, M.; Rossi, L.; Serafini, S.; Gryczynski, Z.; Gryczynski, I., Observation of erythrocyte dynamics in the retinal capillaries and choriocapillaris using ICG-loaded erythrocyte ghost cells. *Invest Ophthalmol Vis Sci* **2008,** *49* (12), 5510-6.

5.  Jiang, Q.; Luo, Z.; Men, Y.; Yang, P.; Peng, H.; Guo, R.; Tian, Y.; Pang, Z.; Yang, W., Red blood cell membrane-camouflaged melanin nanoparticles for enhanced photothermal therapy. *Biomaterials* **2017,** *143*, 29-45.

6.  Burns, J. M.; Vankayala, R.; Mac, J. T.; Anvari, B., Erythrocyte-Derived Theranostic Nanoplatforms for Near Infrared Fluorescence Imaging and Photodestruction of Tumors. *ACS Appl Mater Interfaces* **2018,** *10* (33), 27621-27630.

7.  Wang, F.; Zong, R.; Chen, G., Erythrocyte-enabled immunomodulation for vaccine delivery. *J Control Release* **2022,** *341*, 314-328.

8.  Han, X.; Shen, S.; Fan, Q.; Chen, G.; Archibong, E.; Dotti, G.; Liu, Z.; Gu, Z.; Wang, C., Red blood cell-derived nanoerythrosome for antigen delivery with enhanced cancer immunotherapy. *Sci Adv* **2019,** *5* (10), eaaw6870.

9.  Bahmani, B.; Bacon, D.; Anvari, B., Erythrocyte-derived photo-theranostic agents: hybrid nano-vesicles containing indocyanine green for near infrared imaging and therapeutic applications. *Sci Rep* **2013,** *3*, 2180.

10. Burns, J. M.; Jia, W. C.; Nelson, J. S.; Majaron, B.; Anvari, B., Photothermal treatment of port-wine stains using erythrocyte-derived particles doped with indocyanine green: a theoretical study. *Journal of Biomedical Optics* **2018,** *23* (12).

11. Mac, J. T.; Vankayala, R.; Lee, C. H.; Anvari, B., Erythrocyte-Derived Nanoparticles with Folate Functionalization for Near Infrared Pulsed Laser-Mediated Photo-Chemotherapy of Tumors. *Int J Mol Sci* **2022,** *23* (18).

12. Zhang, W.; Zhao, M.; Gao, Y.; Cheng, X.; Liu, X.; Tang, S.; Peng, Y.; Wang, N.; Hu, D.; Peng, H.; Zhang, J.; Wang, Q., Biomimetic erythrocytes engineered drug delivery for cancer therapy. *Chemical Engineering Journal* **2022,** *433*, 133498.

13. Oldenborg, P. A.; Zheleznyak, A.; Fang, Y. F.; Lagenaur, C. F.; Gresham, H. D.; Lindberg, F. P., Role of CD47 as a marker of self on red blood cells. *Science* **2000,** *288* (5473), 2051-+.

14. Mac, J. T.; Nunez, V.; Burns, J. M.; Guerrero, Y. A.; Vullev, V. I.; Anvari, B., Erythrocyte-derived nano-probes functionalized with antibodies for targeted near infrared fluorescence imaging of cancer cells. *Biomed Opt Express* **2016,** *7* (4), 1311-22.

15. Lu, T.; Lee, C. H.; Anvari, B., Morphological Characteristics, Hemoglobin Content, and Membrane Mechanical Properties of Red Blood Cell Delivery Systems. *ACS Appl Mater Interfaces* **2022,** *14* (16), 18219-18232.

16. de Back, D. Z.; Kostova, E. B.; van Kraaij, M.; van den Berg, T. K.; van Bruggen, R., Of macrophages and red blood cells; a complex love story. *Front Physiol* **2014,** *5*, 9.

17. Arashiki, N.; Takakuwa, Y., Maintenance and regulation of asymmetric phospholipid distribution in human erythrocyte membranes: implications for erythrocyte functions. *Curr Opin Hematol* **2017,** *24* (3), 167-172.

18. Hong, G. S.; Antaris, A. L.; Dai, H. J., Near-infrared fluorophores for biomedical imaging. *Nat Biomed Eng* **2017,** *1* (1).

19. Kilcoyne, R. F.; Richardson, M. L.; Porter, B. A.; Olson, D. O.; Greenlee, T. K.; Lanzer, W., Magnetic resonance imaging of soft tissue masses. *Clin Orthop Relat Res* **1988,** (228), 13-9.

20. Hughes, P.; Miranda, R.; Doyle, A. J., MRI imaging of soft tissue tumours of the foot and ankle. *Insights Imaging* **2019,** *10* (1), 60.

21. Pierigè, F.; Serafini, S.; Rossi, L.; Magnani, M., Cell-based drug delivery. *Adv Drug Deliv Rev* **2008,** *60* (2), 286-95.

22. Gutierrez Millan, C.; Colino Gandarillas, C. I.; Sayalero Marinero, M. L.; Lanao, J. M., Cell-based drug-delivery platforms. *Ther Deliv* **2012,** *3* (1), 25-41.

23. Timin, A. S.; Litvak, M. M.; Gorin, D. A.; Atochina-Vasserman, E. N.; Atochin, D. N.; Sukhorukov, G. B., Cell-Based Drug Delivery and Use of Nano-and Microcarriers for Cell Functionalization. *Adv Healthc Mater* **2018,** *7* (3).

24. Yang, L.; Zang, G. C.; Li, J. W.; Li, X. Y.; Li, Y. Z.; Zhao, Y. P., Cell-derived biomimetic nanoparticles as a novel drug delivery system for atherosclerosis: predecessors and perspectives. *Regen Biomater* **2020,** *7* (4), 349-358.

25. Bush, L. M.; Healy, C. P.; Javdan, S. B.; Emmons, J. C.; Deans, T. L., Biological Cells as Therapeutic Delivery Vehicles. *Trends Pharmacol Sci* **2021,** *42* (2), 106-118.

26. Makrides, S. C., Therapeutic inhibition of the complement system. *Pharmacol Rev* **1998,** *50* (1), 59-87.

27. Chien, S., Red cell deformability and its relevance to blood flow. *Annu Rev Physiol* **1987,** *49*, 177-92.

28. Huisjes, R.; Bogdanova, A.; van Solinge, W. W.; Schiffelers, R. M.; Kaestner, L.; van Wijk, R., Squeezing for Life - Properties of Red Blood Cell Deformability. *Front Physiol* **2018,** *9*, 656.

29. Pivkin, I. V.; Peng, Z.; Karniadakis, G. E.; Buffet, P. A.; Dao, M.; Suresh, S., Biomechanics of red blood cells in human spleen and consequences for physiology and disease. *Proc Natl Acad Sci U S A* **2016,** *113* (28), 7804-9.

30. Safeukui, I.; Buffet, P. A.; Deplaine, G.; Perrot, S.; Brousse, V.; Sauvanet, A.; Aussilhou, B.; Dokmak, S.; Couvelard, A.; Cazals-Hatem, D.; Mercereau-Puijalon, O.; Milon, G.; David, P. H.; Mohandas, N., Sensing of red blood cells with decreased membrane deformability by the human spleen. *Blood Adv* **2018,** *2* (20), 2581-2587.

31. Kakhniashvili, D. G.; Bulla, L. A., Jr.; Goodman, S. R., The human erythrocyte proteome: analysis by ion trap mass spectrometry. *Mol Cell Proteomics* **2004,** *3* (5), 501-9.

32. Bryk, A. H.; Wisniewski, J. R., Quantitative Analysis of Human Red Blood Cell Proteome. *J Proteome Res* **2017,** *16* (8), 2752-2761.

33. Yannuzzi, L. A., Indocyanine Green Angiography: A Perspective on Use in the Clinical Setting. *Am J Ophthalmol* **2011,** *151* (5), 745-751.

34. Klufas, M. A.; Yannuzzi, N. A.; Pang, C. E.; Srinivas, S.; Sadda, S. R.; Freund, K. B.; Kiss, S., Feasibility and clinical utility of ultra-widefield indocyanine green angiography. *Retina* **2015,** *35* (3), 508-20.

35. Kitai, T.; Inomoto, T.; Miwa, M.; Shikayama, T., Fluorescence navigation with indocyanine green for detecting sentinel lymph nodes in breast cancer. *Breast Cancer* **2005,** *12* (3), 211-5.

36.    Onda, N.; Kimura, M.; Yoshida, T.; Shibutani, M., Preferential tumor cellular uptake and retention of indocyanine green for in vivo tumor imaging. *Int J Cancer* **2016,** *139* (3), 673-82.

37.    Teng, C. W.; Huang, V.; Arguelles, G. R.; Zhou, C.; Cho, S. S.; Harmsen, S.; Lee, J. Y. K., Applications of indocyanine green in brain tumor surgery: review of clinical evidence and emerging technologies. *Neurosurg Focus* **2021,** *50* (1), E4.

38.    An, F.; Yang, Z.; Zheng, M.; Mei, T.; Deng, G.; Guo, P.; Li, Y.; Sheng, R., Rationally assembled albumin/indocyanine green nanocomplex for enhanced tumor imaging to guide photothermal therapy. *J Nanobiotechnology* **2020,** *18* (1), 49.

39.    Klein, A.; Szeimies, R. M.; Baumler, W.; Zeman, F.; Schreml, S.; Hohenleutner, U.; Landthaler, M.; Koller, M.; Babilas, P., Indocyanine green-augmented diode laser treatment of port-wine stains: clinical and histological evidence for a new treatment option from a randomized controlled trial. *Br J Dermatol* **2012,** *167* (2), 333-42.

40.    Ren, X.; Zheng, R.; Fang, X.; Wang, X.; Zhang, X.; Yang, W.; Sha, X., Red blood cell membrane camouflaged magnetic nanoclusters for imaging-guided photothermal therapy. *Biomaterials* **2016,** *92*, 13-24.

41.    Liu, W.; Ruan, M.; Wang, Y.; Song, R.; Ji, X.; Xu, J.; Dai, J.; Xue, W., Light-Triggered Biomimetic Nanoerythrocyte for Tumor-Targeted Lung Metastatic Combination Therapy of Malignant Melanoma. *Small* **2018,** *14* (38), e1801754.

42.    Ye, S.; Wang, F.; Fan, Z.; Zhu, Q.; Tian, H.; Zhang, Y.; Jiang, B.; Hou, Z.; Li, Y.; Su, G., Light/pH-Triggered Biomimetic Red Blood Cell Membranes Camouflaged Small Molecular Drug Assemblies for Imaging-Guided Combinational Chemo-Photothermal Therapy. *ACS Appl Mater Interfaces* **2019,** *11* (17), 15262-15275.

43.    Wang, P.; Jiang, F.; Chen, B.; Tang, H.; Zeng, X.; Cai, D.; Zhu, M.; Long, R.; Yang, D.; Kankala, R. K.; Wang, S.; Liu, Y., Bioinspired red blood cell membrane-encapsulated biomimetic nanoconstructs for synergistic and efficacious chemo-photothermal therapy. *Colloids Surf B Biointerfaces* **2020,** *189*, 110842.

44.    Pan, Y.; He, Y.; Zhao, X.; Pan, Y.; Meng, X.; Lv, Z.; Hu, Z.; Mou, X.; Cai, Y., Engineered Red Blood Cell Membrane-Coating Salidroside/Indocyanine Green Nanovesicles for High-Efficiency Hypoxic Targeting Phototherapy of Triple-Negative Breast Cancer. *Adv Healthc Mater* **2022**, e2200962.

45.    Jia, W.; Burns, J. M.; Villantay, B.; Tang, J. C.; Vankayala, R.; Lertsakdadet, B.; Choi, B.; Nelson, J. S.; Anvari, B., Intravital Vascular Phototheranostics and Real-Time Circulation Dynamics of Micro- and Nanosized Erythrocyte-Derived Carriers. *ACS Appl Mater Interfaces* **2020,** *12* (1), 275-287.

46.     Garfin, D. E., One-dimensional gel electrophoresis. *Methods Enzymol* **1990,** *182*, 425-41.

47.     Walker, J. M., SDS Polyacrylamide Gel Electrophoresis of Proteins. *Springer Protoc Hand* **2009**, 177-185.

48.     Low, T. Y.; Seow, T. K.; Chung, M. C., Separation of human erythrocyte membrane associated proteins with one-dimensional and two-dimensional gel electrophoresis followed by identification with matrix-assisted laser desorption/ionization-time of flight mass spectrometry. *Proteomics* **2002,** *2* (9), 1229-39.

49.     Yawata, Y., *Cell Membrane: The Red Blood Cell as a Model*. Wiley: 2006.

50.     Cui, X.; Churchill, G. A., Statistical tests for differential expression in cDNA microarray experiments. *Genome Biol* **2003,** *4* (4), 210.

51.     Aguilan, J. T.; Kulej, K.; Sidoli, S., Guide for protein fold change and p-value calculation for non-experts in proteomics. *Mol Omics* **2020,** *16* (6), 573-582.

52.     Mi, H.; Muruganujan, A.; Huang, X.; Ebert, D.; Mills, C.; Guo, X.; Thomas, P. D., Protocol Update for large-scale genome and gene function analysis with the PANTHER classification system (v.14.0). *Nat Protoc* **2019,** *14* (3), 703-721.

53.     Bathla, S.; Sindhu, A.; Kumar, S.; Dubey, S. K.; Pattnaik, S.; Rawat, P.; Chopra, A.; Dang, A.; Kaushik, J. K.; Mohanty, A. K., Tandem Mass Tag (TMT)-based quantitative proteomics reveals potential targets associated with onset of Sub-clinical Mastitis in cows. *Sci Rep* **2020,** *10* (1), 9321.

54.     Fairbanks, G.; Steck, T. L.; Wallach, D. F., Electrophoretic analysis of the major polypeptides of the human erythrocyte membrane. *Biochemistry* **1971,** *10* (13), 2606-17.

55.     Ballas, S. K.; Krasnow, S. H., Structure of erythrocyte membrane and its transport functions. *Ann Clin Lab Sci* **1980,** *10* (3), 209-19.

56.     Aoki, T., A Comprehensive Review of Our Current Understanding of Red Blood Cell (RBC) Glycoproteins. *Membranes (Basel)* **2017,** *7* (4).

57.     Matei, H.; Frentescu, L.; Benga, G., Comparative studies of the protein composition of red blood cell membranes from eight mammalian species. *J Cell Mol Med* **2000,** *4* (4), 270-276.

58.     Lux, S. E. t., Anatomy of the red cell membrane skeleton: unanswered questions. *Blood* **2016,** *127* (2), 187-99.

59.   Mohandas, N.; Gallagher, P. G., Red cell membrane: past, present, and future. *Blood* **2008,** *112* (10), 3939-48.

60.   Khanna, R.; Chang, S. H.; Andrabi, S.; Azam, M.; Kim, A.; Rivera, A.; Brugnara, C.; Low, P. S.; Liu, S. C.; Chishti, A. H., Headpiece domain of dematin is required for the stability of the erythrocyte membrane. *P Natl Acad Sci USA* **2002,** *99* (10), 6637-6642.

61.   Bennett, V., The spectrin-actin junction of erythrocyte membrane skeletons. *Biochim Biophys Acta* **1989,** *988* (1), 107-21.

62.   Bennett, V., Spectrin-Based Membrane Skeleton - a Multipotential Adapter between Plasma-Membrane and Cytoplasm. *Physiol Rev* **1990,** *70* (4), 1029-1065.

63.   Hui, Y.; Yi, X.; Hou, F.; Wibowo, D.; Zhang, F.; Zhao, D.; Gao, H.; Zhao, C. X., Role of Nanoparticle Mechanical Properties in Cancer Drug Delivery. *ACS Nano* **2019,** *13* (7), 7410-7424.

64.   Baranov, M. V.; Kumar, M.; Sacanna, S.; Thutupalli, S.; van den Bogaart, G., Modulation of Immune Responses by Particle Size and Shape. *Front Immunol* **2020,** *11*, 607945.

65.   Koshino, I.; Mohandas, N.; Takakuwa, Y., Identification of a novel role for dematin in regulating red cell membrane function by modulating spectrin-actin interaction. *J Biol Chem* **2012,** *287* (42), 35244-35250.

66.   An, X.; Lecomte, M. C.; Chasis, J. A.; Mohandas, N.; Gratzer, W., Shear-response of the spectrin dimer-tetramer equilibrium in the red blood cell membrane. *J Biol Chem* **2002,** *277* (35), 31796-800.

67.   Segawa, K.; Nagata, S., An Apoptotic 'Eat Me' Signal: Phosphatidylserine Exposure. *Trends Cell Biol* **2015,** *25* (11), 639-650.

68.   Wesseling, M. C.; Wagner-Britz, L.; Nguyen, D. B.; Asanidze, S.; Mutua, J.; Mohamed, N.; Hanf, B.; Ghashghaeinia, M.; Kaestner, L.; Bernhardt, I., Novel Insights in the Regulation of Phosphatidylserine Exposure in Human Red Blood Cells. *Cell Physiol Biochem* **2016,** *39* (5), 1941-1954.

69.   Tang, J. C.; Vankayala, R.; Mac, J. T.; Anvari, B., RBC-Derived Optical Nanoparticles Remain Stable After a Freeze-Thaw Cycle. *Langmuir* **2020,** *36* (34), 10003-10011.

70.   Hunter, D. G.; Frisken, B. J., Effect of extrusion pressure and lipid properties on the size and polydispersity of lipid vesicles. *Biophys J* **1998,** *74* (6), 2996-3002.

71.  Sun, X.; Rossin, R.; Turner, J. L.; Becker, M. L.; Joralemon, M. J.; Welch, M. J.; Wooley, K. L., An assessment of the effects of shell cross-linked nanoparticle size, core composition, and surface PEGylation on in vivo biodistribution. *Biomacromolecules* **2005,** *6* (5), 2541-54.

72.  Anselmo, A. C.; Mitragotri, S., Impact of particle elasticity on particle-based drug delivery systems. *Adv Drug Deliv Rev* **2017,** *108*, 51-67.

73.  Guo, P.; Liu, D.; Subramanyam, K.; Wang, B.; Yang, J.; Huang, J.; Auguste, D. T.; Moses, M. A., Nanoparticle elasticity directs tumor uptake. *Nat Commun* **2018,** *9* (1), 130.

74.  Mirzaei, M.; Pascovici, D.; Wu, J. X.; Chick, J.; Wu, Y.; Cooke, B.; Haynes, P.; Molloy, M. P., TMT One-Stop Shop: From Reliable Sample Preparation to Computational Analysis Platform. *Methods Mol Biol* **2017,** *1549*, 45-66.

75.  Anselmo, A. C.; Zhang, M.; Kumar, S.; Vogus, D. R.; Menegatti, S.; Helgeson, M. E.; Mitragotri, S., Elasticity of nanoparticles influences their blood circulation, phagocytosis, endocytosis, and targeting. *ACS Nano* **2015,** *9* (3), 3169-77.

76.  Key, J.; Palange, A. L.; Gentile, F.; Aryal, S.; Stigliano, C.; Di Mascolo, D.; De Rosa, E.; Cho, M.; Lee, Y.; Singh, J.; Decuzzi, P., Soft Discoidal Polymeric Nanoconstructs Resist Macrophage Uptake and Enhance Vascular Targeting in Tumors. *ACS Nano* **2015,** *9* (12), 11628-41.

77.  Ruiz-Arguelles, A.; Llorente, L., The role of complement regulatory proteins (CD55 and CD59) in the pathogenesis of autoimmune hemocytopenias. *Autoimmun Rev* **2007,** *6* (3), 155-61.

78.  Lutz, H. U.; Bogdanova, A., Mechanisms tagging senescent red blood cells for clearance in healthy humans. *Front Physiol* **2013,** *4*, 387.

79.  Oronsky, B.; Carter, C.; Reid, T.; Brinkhaus, F.; Knox, S. J., Just eat it: A review of CD47 and SIRP-alpha antagonism. *Semin Oncol* **2020,** *47* (2-3), 117-124.

80.  van Bruggen, R., CD47 Functions as a Molecular Switch for Erythrocyte Phagocytosis. *Vox Sang* **2013,** *105*, 27-27.

81.  Mordue, K. E.; Hawley, B. R.; Satchwell, T. J.; Toye, A. M., CD47 surface stability is sensitive to actin disruption prior to inclusion within the band 3 macrocomplex. *Sci Rep-Uk* **2017,** *7*.

82.  Vachon, E.; Martin, R.; Kwok, V.; Cherepanov, V.; Chow, C. W.; Doerschuk, C. M.; Plumb, J.; Grinstein, S.; Downey, G. P., CD44-mediated phagocytosis induces

inside-out activation of complement receptor-3 in murine macrophages. *Blood* **2007,** *110* (13), 4492-502.

83. Aruffo, A.; Stamenkovic, I.; Melnick, M.; Underhill, C. B.; Seed, B., Cd44 Is the Principal Cell-Surface Receptor for Hyaluronate. *Cell* **1990,** *61* (7), 1303-1313.

84. Vachon, E.; Martin, R.; Plumb, J.; Kwok, V.; Vandivier, R. W.; Glogauer, M.; Kapus, A.; Wang, X. M.; Chow, C. W.; Grinstein, S.; Downey, G. P., CD44 is a phagocytic receptor. *Blood* **2006,** *107* (10), 4149-4158.

85. Mi, H.; Ebert, D.; Muruganujan, A.; Mills, C.; Albou, L. P.; Mushayamaha, T.; Thomas, P. D., PANTHER version 16: a revised family classification, tree-based classification tool, enhancer regions and extensive API. *Nucleic Acids Res* **2021,** *49* (D1), D394-D403.

86. Villa, C. H.; Anselmo, A. C.; Mitragotri, S.; Muzykantov, V., Red blood cells: Supercarriers for drugs, biologicals, and nanoparticles and inspiration for advanced delivery systems. *Adv Drug Deliv Rev* **2016,** *106* (Pt A), 88-103.

87. Zhao, Z.; Ukidve, A.; Gao, Y.; Kim, J.; Mitragotri, S., Erythrocyte leveraged chemotherapy (ELeCt): Nanoparticle assembly on erythrocyte surface to combat lung metastasis. *Sci Adv* **2019,** *5* (11), eaax9250.

88. Gao, M.; Hu, A. Y.; Sun, X. Q.; Wang, C.; Dong, Z. L.; Feng, L. Z.; Liu, Z., Photosensitizer Decorated Red Blood Cells as an Ultrasensitive Light Responsive Drug Delivery System. *Acs Appl Mater Inter* **2017,** *9* (7), 5855-5863.

89. Luo, L.; Zeng, F.; Xie, J.; Fan, J.; Xiao, S.; Wang, Z.; Xie, H.; Liu, B., A RBC membrane-camouflaged biomimetic nanoplatform for enhanced chemo-photothermal therapy of cervical cancer. *J Mater Chem B* **2020,** *8* (18), 4080-4092.

90. Sternberg, N.; Georgieva, R.; Duft, K.; Baumler, H., Surface-modified loaded human red blood cells for targeting and delivery of drugs. *J Microencapsul* **2012,** *29* (1), 9-20.

91. Aryal, S.; Nguyen, T. D. T.; Pitchaimani, A.; Shrestha, T. B.; Biller, D.; Troyer, D., Membrane Fusion-Mediated Gold Nanoplating of Red Blood Cell: A Bioengineered CT-Contrast Agent. *ACS Biomater Sci Eng* **2017,** *3* (1), 36-41.

92. Han, X.; Wang, C.; Liu, Z., Red blood cells as smart delivery systems. *Bioconjugate Chem* **2018,** *29* (4), 852-860.

93. Millan, C. G.; Marinero, M. L. S.; Castaneda, A. Z.; Lanao, J. M., Drug, enzyme and peptide delivery using erythrocytes as carriers. *Journal of Controlled Release* **2004,** *95* (1), 27-49.

94. Wang, P.; Wang, X.; Luo, Q.; Li, Y.; Lin, X.; Fan, L.; Zhang, Y.; Liu, J.; Liu, X., Fabrication of Red Blood Cell-Based Multimodal Theranostic Probes for Second Near-Infrared Window Fluorescence Imaging-Guided Tumor Surgery and Photodynamic Therapy. *Theranostics* **2019,** *9* (2), 369-380.

95. Rao, L.; Cai, B.; Bu, L. L.; Liao, Q. Q.; Guo, S. S.; Zhao, X. Z.; Dong, W. F.; Liu, W., Microfluidic Electroporation-Facilitated Synthesis of Erythrocyte Membrane-Coated Magnetic Nanoparticles for Enhanced Imaging-Guided Cancer Therapy. *Acs Nano* **2017,** *11* (4), 3496-3505.

96. Bustamante Lopez, S. C.; Meissner, K. E., Characterization of carrier erythrocytes for biosensing applications. *J Biomed Opt* **2017,** *22* (9), 91510.

97. Flower, R. W.; Kling, R., Observation and characterization of microvascular vasomotion using erythrocyte mediated ICG angiography (EM-ICG-A). *Microvasc Res* **2017,** *113*, 78-87.

98. Wang, D.; Haytham, A.; Mayo, L.; Tao, Y.; Saeedi, O., Automated retinal microvascular velocimetry based on erythrocyte mediated angiography. *Biomed Opt Express* **2019,** *10* (7), 3681-3697.

99. van Meer, G.; Voelker, D. R.; Feigenson, G. W., Membrane lipids: where they are and how they behave. *Nat Rev Mol Cell Bio* **2008,** *9* (2), 112-124.

100. Zachowski, A., Phospholipids in animal eukaryotic membranes: transverse asymmetry and movement. *Biochem J* **1993,** *294 ( Pt 1)*, 1-14.

101. Kodigepalli, K. M.; Bowers, K.; Sharp, A.; Nanjundan, M., Roles and regulation of phospholipid scramblases. *Febs Lett* **2015,** *589* (1), 3-14.

102. Schwarz, S.; Deuticke, B.; Haest, C. W. M., Passive transmembrane redistributions of phospholipids as a determinant of erythrocyte shape change. Studies on electroporated cells. *Mol Membr Biol* **1999,** *16* (3), 247-255.

103. Henszen, M. M. M.; Weske, M.; Schwarz, S.; Haest, C. W. M.; Deuticke, B., Electric field pulses induce reversible shape transformation of human erythrocytes. *Mol Membr Biol* **1997,** *14* (4), 195-204.

104. Haest, C. W.; Kamp, D.; Deuticke, B., Transbilayer reorientation of phospholipid probes in the human erythrocyte membrane. Lessons from studies on electroporated and resealed cells. *Biochim Biophys Acta* **1997,** *1325* (1), 17-33.

105. Dressler, V.; Schwister, K.; Haest, C. W.; Deuticke, B., Dielectric breakdown of the erythrocyte membrane enhances transbilayer mobility of phospholipids. *Biochim Biophys Acta* **1983,** *732* (1), 304-7.

106. Mambrini, G.; Mandolini, M.; Rossi, L.; Pierige, F.; Capogrossi, G.; Salvati, P.; Serafini, S.; Benatti, L.; Magnani, M., Ex vivo encapsulation of dexamethasone sodium phosphate into human autologous erythrocytes using fully automated biomedical equipment. *Int J Pharm* **2017,** *517* (1-2), 175-184.

107. Devitt, A.; Moffatt, O. D.; Raykundalia, C.; Capra, J. D.; Simmons, D. L.; Gregory, C. D., Human CD14 mediates recognition and phagocytosis of apoptotic cells. *Nature* **1998,** *392* (6675), 505-9.

108. Zwaal, R. F.; Comfurius, P.; Bevers, E. M., Surface exposure of phosphatidylserine in pathological cells. *Cell Mol Life Sci* **2005,** *62* (9), 971-88.

109. Arashiki, N.; Saito, M.; Koshino, I.; Kamata, K.; Hale, J.; Mohandas, N.; Manno, S.; Takakuwa, Y., An Unrecognized Function of Cholesterol: Regulating the Mechanism Controlling Membrane Phospholipid Asymmetry. *Biochemistry* **2016,** *55* (25), 3504-3513.

110. Zhou, Q. S.; Zhao, J.; Stout, J. G.; Luhm, R. A.; Wiedmer, T.; Sims, P. J., Molecular cloning of human plasma membrane phospholipid scramblase - A protein mediating transbilayer movement of plasma membrane phospholipids. *Journal of Biological Chemistry* **1997,** *272* (29), 18240-18244.

111. van Zwieten, R.; Bochem, A. E.; Hilarius, P. M.; van Bruggen, R.; Bergkamp, F.; Hovingh, G. K.; Verhoeven, A. J., The cholesterol content of the erythrocyte membrane is an important determinant of phosphatidylserine exposure. *Bba-Mol Cell Biol L* **2012,** *1821* (12), 1493-1500.

112. Posada, I. M.; Fantini, J.; Contreras, F. X.; Barrantes, F.; Alonso, A.; Goni, F. M., A cholesterol recognition motif in human phospholipid scramblase 1. *Biophys J* **2014,** *107* (6), 1383-92.

113. Hoekstra, L. T.; de Graaf, W.; Nibourg, G. A. A.; Heger, M.; Bennink, R. J.; Stieger, B.; van Gulik, T. M., Physiological and Biochemical Basis of Clinical Liver Function Tests A Review. *Ann Surg* **2013,** *257* (1), 27-36.

114. Maarek, J. M.; Holschneider, D. P.; Harimoto, J.; Yang, J.; Scremin, O. U.; Rubinstein, E. H., Measurement of cardiac output with indocyanine green transcutaneous fluorescence dilution technique. *Anesthesiology* **2004,** *100* (6), 1476-83.

115. Kim, T.; O'Brien, C.; Choi, H. S.; Jeong, M. Y., Fluorescence molecular imaging systems for intraoperative image-guided surgery. *Appl Spectrosc Rev* **2018,** *53* (2-4), 349-359.

116. AV, D. S.; Lin, H.; Henderson, E. R.; Samkoe, K. S.; Pogue, B. W., Review of fluorescence guided surgery systems: identification of key performance capabilities beyond indocyanine green imaging. *J Biomed Opt* **2016,** *21* (8), 80901.

117. Boni, L.; David, G.; Mangano, A.; Dionigi, G.; Rausei, S.; Spampatti, S.; Cassinotti, E.; Fingerhut, A., Clinical applications of indocyanine green (ICG) enhanced fluorescence in laparoscopic surgery. *Surg Endosc* **2015,** *29* (7), 2046-55.

118. Griffiths, M.; Chae, M. P.; Rozen, W. M., Indocyanine green-based fluorescent angiography in breast reconstruction. *Gland Surg* **2016,** *5* (2), 133-49.

119. Nowak, K.; Karampinis, I.; Gerken, A. L. H., Application of Fluorescent Dyes in Visceral Surgery: State of the Art and Future Perspectives. *Visc Med* **2020,** *36* (2), 80-87.

120. Burns, J. M.; Shafer, E.; Vankayala, R.; Kundra, V.; Anvari, B., Near Infrared Fluorescence Imaging of Intraperitoneal Ovarian Tumors in Mice Using Erythrocyte-Derived Optical Nanoparticles and Spatially-Modulated Illumination. *Cancers (Basel)* **2021,** *13* (11).

121. Koleva, L.; Bovt, E.; Ataullakhanov, F.; Sinauridze, E., Erythrocytes as Carriers: From Drug Delivery to Biosensors. *Pharmaceutics* **2020,** *12* (3).

122. Bax, B. E., Erythrocytes as Carriers of Therapeutic Enzymes. *Pharmaceutics* **2020,** *12* (5).

123. Tang, J. C.; Partono, A.; Anvari, B., Near-Infrared-Fluorescent Erythrocyte-Mimicking Particles: Physical and Optical Characteristics. *IEEE Trans Biomed Eng* **2019,** *66* (4), 1034-1044.

124. Sarshar, M.; Lu, T.; Anvari, B., Combined optical micromanipulation and interferometric topography (COMMIT). *Biomed. Opt. Express* **2016,** *7* (4), 1365-1374.

125. Lu, T.; Anvari, B., Characterization of the Viscoelastic Properties of Ovarian Cancer Cells Membranes by Optical Tweezers and Quantitative Phase Imaging. *Front Phys-Lausanne* **2020,** *8*.

126. Burns, J. M.; Saager, R.; Majaron, B.; Jia, W.; Anvari, B., Optical properties of biomimetic probes engineered from erythrocytes. *Nanotechnology* **2017,** *28* (3), 035101.

127. Vankayala, R.; Mac, J. T.; Burns, J. M.; Dunn, E.; Carroll, S.; Bahena, E. M.; Patel, D. K.; Griffey, S.; Anvari, B., Biodistribution and toxicological evaluation of micron-

and nano-sized erythrocyte-derived optical particles in healthy Swiss Webster mice. *Biomater Sci* **2019,** *7* (5), 2123-2133.

128. Vrielink, A.; Ghisla, S., Cholesterol oxidase: biochemistry and structural features. *FEBS J* **2009,** *276* (23), 6826-43.

129. Jemaa, M.; Fezai, M.; Bissinger, R.; Lang, F., Methods Employed in Cytofluorometric Assessment of Eryptosis, the Suicidal Erythrocyte Death. *Cell Physiol Biochem* **2017,** *43* (2), 431-444.

130. Kuypers, F. A.; Lewis, R. A.; Hua, M.; Schott, M. A.; Discher, D.; Ernst, J. D.; Lubin, B. H., Detection of altered membrane phospholipid asymmetry in subpopulations of human red blood cells using fluorescently labeled annexin V. *Blood* **1996,** *87* (3), 1179-1187.

131. Taciak, B.; Bialasek, M.; Braniewska, A.; Sas, Z.; Sawicka, P.; Kiraga, L.; Rygiel, T.; Krol, M., Evaluation of phenotypic and functional stability of RAW 264.7 cell line through serial passages. *Plos One* **2018,** *13* (6).

132. Schneider, C. A.; Rasband, W. S.; Eliceiri, K. W., NIH Image to ImageJ: 25 years of image analysis. *Nat Methods* **2012,** *9* (7), 671-5.

133. Wilhelm, S.; Tavares, A. J.; Dai, Q.; Ohta, S.; Audet, J.; Dvorak, H. F.; Chan, W. C. W., Analysis of nanoparticle delivery to tumours. *Nat Rev Mater* **2016,** *1* (5).

134. Layne, E., Spectrophotometric and Turbidimetric Methods for Measuring Proteins. *Method Enzymol* **1957,** *3*, 447-454.

135. Stoscheck, C. M., Quantitation of protein. *Methods Enzymol* **1990,** *182*, 50-68.

136. de Meyer, F. J.; Rodgers, J. M.; Willems, T. F.; Smit, B., Molecular simulation of the effect of cholesterol on lipid-mediated protein-protein interactions. *Biophys J* **2010,** *99* (11), 3629-38.

137. Pajic-Lijakovic, I., Erythrocytes under osmotic stress - modeling considerations. *Prog Biophys Mol Biol* **2015,** *117* (1), 113-24.

138. Yoneya, S.; Saito, T.; Komatsu, Y.; Koyama, I.; Takahashi, K.; Duvoll-Young, J., Binding properties of indocyanine green in human blood. *Invest Ophthalmol Vis Sci* **1998,** *39* (7), 1286-90.

139. Forsyth, A. M.; Braunmuller, S.; Wan, J.; Franke, T.; Stone, H. A., The effects of membrane cholesterol and simvastatin on red blood cell deformability and ATP release. *Microvasc Res* **2012,** *83* (3), 347-51.

140. Ensinck, M. A. B., M. E. L.; Borrás, S. E. G.; Cotorruelo, C. M.; Biondi, C. S., Erythrocyte Senescent Markers by Flow Cytometry. *Open J. Blood Dis.* **2019,** *09*, 47-59.

141. Canellini, G.; Rubin, O.; Delobel, J.; Crettaz, D.; Lion, N.; Tissot, J. D., Red blood cell microparticles and blood group antigens: an analysis by flow cytometry. *Blood Transfus* **2012,** *10 Suppl 2*, s39-45.

142. Alric, C.; Miladi, I.; Kryza, D.; Taleb, J.; Lux, F.; Bazzi, R.; Billotey, C.; Janier, M.; Perriat, P.; Roux, S.; Tillement, O., The biodistribution of gold nanoparticles designed for renal clearance. *Nanoscale* **2013,** *5* (13), 5930-9.

143. Blanco, E.; Shen, H.; Ferrari, M., Principles of nanoparticle design for overcoming biological barriers to drug delivery. *Nat Biotechnol* **2015,** *33* (9), 941-51.

144. Schroit, A. J.; Madsen, J. W.; Tanaka, Y., In vivo recognition and clearance of red blood cells containing phosphatidylserine in their plasma membranes. *J Biol Chem* **1985,** *260* (8), 5131-8.

145. Lee, S. J.; Park, S. Y.; Jung, M. Y.; Bae, S. M.; Kim, I. S., Mechanism for phosphatidylserine-dependent erythrophagocytosis in mouse liver. *Blood* **2011,** *117* (19), 5215-23.

146. Zhang, Y. N.; Poon, W.; Tavares, A. J.; McGilvray, I. D.; Chan, W. C. W., Nanoparticle-liver interactions: Cellular uptake and hepatobiliary elimination. *J Control Release* **2016,** *240*, 332-348.

147. Brigger, I.; Dubernet, C.; Couvreur, P., Nanoparticles in cancer therapy and diagnosis. *Adv Drug Deliv Rev* **2002,** *54* (5), 631-51.

148. Gavas, S.; Quazi, S.; Karpinski, T. M., Nanoparticles for Cancer Therapy: Current Progress and Challenges. *Nanoscale Res Lett* **2021,** *16* (1), 173.

149. Xia, Q.; Zhang, Y.; Li, Z.; Hou, X.; Feng, N., Red blood cell membrane-camouflaged nanoparticles: a novel drug delivery system for antitumor application. *Acta Pharm Sin B* **2019,** *9* (4), 675-689.

150. Tang, J. C.; Lee, C. H.; Lu, T.; Vankayala, R.; Hanley, T.; Azubuogu, C.; Li, J.; Nair, M. G.; Jia, W.; Anvari, B., Membrane Cholesterol Enrichment of Red Blood Cell-Derived Microparticles Results in Prolonged Circulation. *ACS Appl Bio Mater* **2022,** *5* (2), 650-660.

151. Kuypers, F. A.; de Jong, K., The role of phosphatidylserine in recognition and removal of erythrocytes. *Cell Mol Biol (Noisy-le-grand)* **2004,** *50* (2), 147-58.

152. Schroit, A. J.; Tanaka, Y.; Madsen, J.; Fidler, I. J., The recognition of red blood cells by macrophages: role of phosphatidylserine and possible implications of membrane phospholipid asymmetry. *Biol Cell* **1984,** *51* (2), 227-38.

153. Wesseling, M. C.; Wagner-Britz, L.; Huppert, H.; Hanf, B.; Hertz, L.; Nguyen, D. B.; Bernhardt, I., Phosphatidylserine Exposure in Human Red Blood Cells Depending on Cell Age. *Cell Physiol Biochem* **2016,** *38* (4), 1376-90.

154. Luo, S.; Zhang, E.; Su, Y.; Cheng, T.; Shi, C., A review of NIR dyes in cancer targeting and imaging. *Biomaterials* **2011,** *32* (29), 7127-38.

155. Zhao, J.; Zhong, D.; Zhou, S., NIR-I-to-NIR-II fluorescent nanomaterials for biomedical imaging and cancer therapy. *J Mater Chem B* **2018,** *6* (3), 349-365.

156. Dai, H.; Shen, Q.; Shao, J.; Wang, W.; Gao, F.; Dong, X., Small Molecular NIR-II Fluorophores for Cancer Phototheranostics. *Innovation (Camb)* **2021,** *2* (1), 100082.

157. Schaafsma, B. E.; Mieog, J. S. D.; Hutteman, M.; Van der Vorst, J. R.; Kuppen, P. J. K.; Lowik, C. W. G. M.; Frangioni, J. V.; Van de Velde, C. J. H.; Vahrmeijer, A. L., The Clinical Use of Indocyanine Green as a Near-Infrared Fluorescent Contrast Agent for Image-Guided Oncologic Surgery. *J Surg Oncol* **2011,** *104* (3), 323-332.

158. Levesque, E.; Martin, E.; Dudau, D.; Lim, C.; Dhonneur, G.; Azoulay, D., Current use and perspective of indocyanine green clearance in liver diseases. *Anaesth Crit Care Pa* **2016,** *35* (1), 49-57.

159. Overchuk, M.; Zheng, G., Overcoming obstacles in the tumor microenvironment: Recent advancements in nanoparticle delivery for cancer theranostics. *Biomaterials* **2018,** *156*, 217-237.

160. Sanita, G.; Carrese, B.; Lamberti, A., Nanoparticle Surface Functionalization: How to Improve Biocompatibility and Cellular Internalization. *Front Mol Biosci* **2020,** *7*.

161. Marques, A. C.; Costa, P. J.; Velho, S.; Amaral, M. H., Functionalizing nanoparticles with cancer-targeting antibodies: A comparison of strategies. *J Control Release* **2020,** *320*, 180-200.

162. Vankayala, R.; Corber, S. R.; Mac, J. T.; Rao, M. P.; Shafie, M.; Anvari, B., Erythrocyte-Derived Nanoparticles as a Theranostic Agent for Near-Infrared Fluorescence Imaging and Thrombolysis of Blood Clots. *Macromol Biosci* **2018,** *18* (4).

163. Parker, N.; Turk, M. J.; Westrick, E.; Lewis, J. D.; Low, P. S.; Leamon, C. P., Folate receptor expression in carcinomas and normal tissues determined by a quantitative radioligand binding assay. *Anal Biochem* **2005,** *338* (2), 284-93.

164. Cheung, A.; Bax, H. J.; Josephs, D. H.; Ilieva, K. M.; Pellizzari, G.; Opzoomer, J.; Bloomfield, J.; Fittall, M.; Grigoriadis, A.; Figini, M.; Canevari, S.; Spicer, J. F.; Tutt, A. N.; Karagiannis, S. N., Targeting folate receptor alpha for cancer treatment. *Oncotarget* **2016,** *7* (32), 52553-52574.

165. Liu, Y.; Chen, S.; Sun, J.; Zhu, S.; Chen, C.; Xie, W.; Zheng, J.; Zhu, Y.; Xiao, L.; Hao, L.; Wang, Z.; Chang, S., Folate-Targeted and Oxygen/Indocyanine Green Loaded Lipid Nanoparticles for Dual-Mode Imaging and Photo-Sonodynamic/Photothermal Therapy of Ovarian Cancer in Vitro and in Vivo. *Mol Pharm* **2020,** *17* (4), 1442-1443.

166. Ebert, B.; Riefke, B.; Sukowski, U.; Licha, K., Cyanine dyes as contrast agents for near-infrared imaging in vivo: acute tolerance, pharmacokinetics, and fluorescence imaging. *J Biomed Opt* **2011,** *16* (6), 066003.

167. Joshi, N.; Walter, J. M.; Misharin, A. V., Alveolar Macrophages. *Cell Immunol* **2018,** *330*, 86-90.

168. Tan, W.; Wang, J.; Zhou, F.; Gao, L.; Yin, R.; Liu, H.; Sukanthanag, A.; Wang, G.; Mihm, M. C., Jr.; Chen, D. B.; Nelson, J. S., Coexistence of Eph receptor B1 and ephrin B2 in port-wine stain endothelial progenitor cells contributes to clinicopathological vasculature dilatation. *Br J Dermatol* **2017,** *177* (6), 1601-1611.

169. Jacobs, A. H.; Walton, R. G., The incidence of birthmarks in the neonate. *Pediatrics* **1976,** *58* (2), 218-22.

170. Cordoro, K. M.; Speetzen, L. S.; Koerper, M. A.; Frieden, I. J., Physiologic changes in vascular birthmarks during early infancy: Mechanisms and clinical implications. *J Am Acad Dermatol* **2009,** *60* (4), 669-75.

171. Kanada, K. N.; Merin, M. R.; Munden, A.; Friedlander, S. F., A prospective study of cutaneous findings in newborns in the United States: correlation with race, ethnicity, and gestational status using updated classification and nomenclature. *J Pediatr* **2012,** *161* (2), 240-5.

172. Geronemus, R. G.; Ashinoff, R., The medical necessity of evaluation and treatment of port-wine stains. *J Dermatol Surg Oncol* **1991,** *17* (1), 76-9.

173. Minkis, K.; Geronemus, R. G.; Hale, E. K., Port wine stain progression: a potential consequence of delayed and inadequate treatment? *Lasers Surg Med* **2009,** *41* (6), 423-6.

174. Savas, J. A.; Ledon, J. A.; Franca, K.; Chacon, A.; Nouri, K., Pulsed dye laser-resistant port-wine stains: mechanisms of resistance and implications for treatment. *Br J Dermatol* **2013,** *168* (5), 941-53.

175. Garden, J. M.; Polla, L. L.; Tan, O. T., The treatment of port-wine stains by the pulsed dye laser. Analysis of pulse duration and long-term therapy. *Arch Dermatol* **1988,** *124* (6), 889-96.

176. Jasim, Z. F.; Handley, J. M., Treatment of pulsed dye laser-resistant port wine stain birthmarks. *J Am Acad Dermatol* **2007,** *57* (4), 677-82.

177. Wanitphakdeedecha, R.; Jantarakolica, T.; Ng, J. N. C.; Yan, C.; Nanchaipruek, Y.; Jantanapornchai, N.; Manuskiatti, W.; Sudhipongpracha, T., The Cost-Effectiveness of Pulsed-Dye Laser Therapy Among Thai Patients with Facial Port-Wine Stain: A Retrospective Study and Economic Evaluation. *Dermatol Ther (Heidelb)* **2021,** *11* (2), 465-473.

178. Woo, W. K.; Handley, J. M., Does fluence matter in the laser treatment of port-wine stains? *Clin Exp Dermatol* **2003,** *28* (5), 556-7.

179. van Raath, M. I.; Chohan, S.; Wolkerstorfer, A.; van der Horst, C.; Storm, G.; Heger, M., Port wine stain treatment outcomes have not improved over the past three decades. *J Eur Acad Dermatol Venereol* **2019,** *33* (7), 1369-1377.

180. Tunnell, J. W.; Wang, L. V.; Anvari, B., Optimum pulse duration and radiant exposure for vascular laser therapy of dark port-wine skin: a theoretical study. *Appl Opt* **2003,** *42* (7), 1367-78.

181. Kelly, K. M.; Choi, B.; McFarlane, S.; Motosue, A.; Jung, B.; Khan, M. H.; Ramirez-San-Juan, J. C.; Nelson, J. S., Description and analysis of treatments for port-wine stain birthmarks. *Arch Facial Plast Surg* **2005,** *7* (5), 287-94.

182. Ashinoff, R.; Geronemus, R. G., Treatment of a port-wine stain in a black patient with the pulsed dye laser. *J Dermatol Surg Oncol* **1992,** *18* (2), 147-8.

183. Cichorek, M.; Wachulska, M.; Stasiewicz, A.; Tyminska, A., Skin melanocytes: biology and development. *Postepy Dermatol Alergol* **2013,** *30* (1), 30-41.

184. Jacques, S. L., Optical properties of biological tissues: a review. *Phys Med Biol* **2013,** *58* (11), R37-61.

185. Jacques, S. L., Optical Absorption of Melanin.

186. Prahl, S., Optical Absorption of Hemoglobin.

187. Meredith, P.; Sarna, T., The physical and chemical properties of eumelanin. *Pigment Cell Res* **2006,** *19* (6), 572-94.

188. Frangioni, J. V., In vivo near-infrared fluorescence imaging. *Curr Opin Chem Biol* **2003,** *7* (5), 626-34.

189. Zhang, Y.; Yan, G. H.; Han, F. G.; Yang, L.; Shu, J.; Liu, L. T.; Zhang, W.; Shang, A.; Bai, J., Application of indocyanine green and near-infrared fluorescence imaging for the assessment of peritoneal dialysis-related complications. *Photodiagn Photodyn* **2022,** *39*.

190. Miwa, M.; Shikayama, T., ICG fluorescence imaging and its medical applications. *P Soc Photo-Opt Ins* **2009,** *7160*.

191. Sevick-Muraca, E. M., Translation of Near-Infrared Fluorescence Imaging Technologies: Emerging Clinical Applications. *Annu Rev Med* **2012,** *63*, 217-231.

192. Klein, A.; Baumler, W.; Buschmann, M.; Landthaler, M.; Babilas, P., A randomized controlled trial to optimize indocyanine green-augmented diode laser therapy of capillary malformations. *Lasers Surg Med* **2013,** *45* (4), 216-24.

193. De Gasperi, A.; Mazza, E.; Prosperi, M., Indocyanine green kinetics to assess liver function: Ready for a clinical dynamic assessment in major liver surgery? *World J Hepatol* **2016,** *8* (7), 355-67.

194. Ding, H.; Lv, Y.; Ni, D.; Wang, J.; Tian, Z.; Wei, W.; Ma, G., Erythrocyte membrane-coated NIR-triggered biomimetic nanovectors with programmed delivery for photodynamic therapy of cancer. *Nanoscale* **2015,** *7* (21), 9806-15.

195. Yu, B.; Xue, X.; Yin, Z. F.; Cao, L. H.; Li, M. M.; Huang, J. P., Engineered Cell Membrane-Derived Nanocarriers: The Enhanced Delivery System for Therapeutic Applications. *Front Cell Dev Biol* **2022,** *10*.

196. Hu, C. M.; Fang, R. H.; Zhang, L., Erythrocyte-inspired delivery systems. *Adv Healthc Mater* **2012,** *1* (5), 537-47.

197. Rani, N. N. I. M.; Alzubaidi, Z. M.; Azhari, H.; Mustapa, F.; Amin, M. C. I. M., Novel engineering: Biomimicking erythrocyte as a revolutionary platform for drugs and vaccines delivery. *Eur J Pharmacol* **2021,** *900*.

198. Hanley, T.; Yin, R.; Mac, J.; Tan, W.; Anvari, B., Functionalized erythrocyte-derived optical nanoparticles to target ephrin-B2 ligands. *J Biomed Opt* **2019,** *24* (8), 1-9.

199. Choi, B.; Tan, W.; Jia, W.; White, S. M.; Moy, W. J.; Yang, B. Y.; Zhu, J.; Chen, Z.; Kelly, K. M.; Nelson, J. S., The Role of Laser Speckle Imaging in Port-Wine Stain Research: Recent Advances and Opportunities. *IEEE J Sel Top Quantum Electron* **2016,** *2016* (3).

200. Choi, B.; Kang, N. M.; Nelson, J. S., Laser speckle imaging for monitoring blood flow dynamics in the in vivo rodent dorsal skin fold model. *Microvasc Res* **2004,** *68* (2), 143-6.

201. Dai, T.; Diagaradjane, P.; Yaseen, M. A.; Pikkula, B. M.; Thomsen, S.; Anvari, B., Laser-induced thermal injury to dermal blood vessels: analysis of wavelength (585 nm vs. 595 nm), cryogen spray cooling, and wound healing effects. *Lasers Surg Med* **2005,** *37* (3), 210-8.

202. Yaseen, M. A.; Diagaradjane, P.; Pikkula, B. M.; Yu, J.; Wong, M. S.; Anvaria, B., Photothermal and photochemical effects of laser light absorption by indocyanine green (ICG). *Proc Spie* **2005,** *5695*, 27-35.

203. van Raath, M. I.; van Amesfoort, J. E.; Hermann, M.; Ince, Y.; Zwart, M. J.; Echague, A. V.; Chen, Y.; Ding, B.; Huang, X.; Storm, G.; Heger, M., Site-specific pharmaco-laser therapy: A novel treatment modality for refractory port wine stains. *J Clin Transl Res* **2019,** *5* (1), 1-24.

204. Aguilar, G.; Choi, B.; Broekgaarden, M.; Yang, O.; Yang, B.; Ghasri, P.; Chen, J. K.; Bezemer, R.; Nelson, J. S.; van Drooge, A. M.; Wolkerstorfer, A.; Kelly, K. M.; Heger, M., An overview of three promising mechanical, optical, and biochemical engineering approaches to improve selective photothermolysis of refractory port wine stains. *Ann Biomed Eng* **2012,** *40* (2), 486-506.

205. Ribitsch, I.; Baptista, P. M.; Lange-Consiglio, A.; Melotti, L.; Patruno, M.; Jenner, F.; Schnabl-Feichter, E.; Dutton, L. C.; Connolly, D. J.; van Steenbeek, F. G.; Dudhia, J.; Penning, L. C., Large Animal Models in Regenerative Medicine and Tissue Engineering: To Do or Not to Do. *Front Bioeng Biotech* **2020,** *8*.

206. Schwarz, C.; Plass, I.; Fitschek, F.; Punzengruber, A.; Mittlbock, M.; Kampf, S.; Asenbaum, U.; Starlinger, P.; Stremitzer, S.; Bodingbauer, M.; Kaczirek, K., The value of indocyanine green clearance assessment to predict postoperative liver dysfunction in patients undergoing liver resection. *Sci Rep* **2019,** *9* (1), 8421.

207. Leevy, C. M.; Smith, F.; Longueville, J.; Paumgartner, G.; Howard, M. M., Indocyanine green clearance as a test for hepatic function. Evaluation by dichromatic ear densitometry. *JAMA* **1967,** *200* (3), 236-40.

208. Hu, C. M.; Zhang, L.; Aryal, S.; Cheung, C.; Fang, R. H.; Zhang, L., Erythrocyte membrane-camouflaged polymeric nanoparticles as a biomimetic delivery platform. *Proc Natl Acad Sci U S A* **2011,** *108* (27), 10980-5.

209. Di, W.; Tan, X.; Calderon, I. A. C.; Neal Reilly, A. E.; Niedre, M.; Clark, H. A., Real-time particle-by-particle detection of erythrocyte-camouflaged microsensor

with extended circulation time in the bloodstream. *Proc Natl Acad Sci U S A* **2020,** *117* (7), 3509-3517.

210. Morrissey, M. A.; Kern, N.; Vale, R. D., CD47 Ligation Repositions the Inhibitory Receptor SIRPA to Suppress Integrin Activation and Phagocytosis. *Immunity* **2020,** *53* (2), 290-302 e6.

211. Oldenborg, P. A., Role of CD47 in erythroid cells and in autoimmunity. *Leuk Lymphoma* **2004,** *45* (7), 1319-27.

212. Piao, J. G.; Wang, L. M.; Gao, F.; You, Y. Z.; Xiong, Y. J.; Yang, L. H., Erythrocyte Membrane Is an Alternative Coating to Polyethylene Glycol for Prolonging the Circulation Lifetime of Gold Nanocages for Photothermal Therapy. *Acs Nano* **2014,** *8* (10), 10414-10425.

213. Wang, C.; Wang, Z.; Zhao, T.; Li, Y.; Huang, G.; Sumer, B. D.; Gao, J., Optical molecular imaging for tumor detection and image-guided surgery. *Biomaterials* **2018,** *157*, 62-75.

214. Gotoh, K.; Yamada, T.; Ishikawa, O.; Takahashi, H.; Eguchi, H.; Yano, M.; Ohigashi, H.; Tomita, Y.; Miyamoto, Y.; Imaoka, S., A novel image-guided surgery of hepatocellular carcinoma by indocyanine green fluorescence imaging navigation. *J Surg Oncol* **2009,** *100* (1), 75-9.

215. Keereweer, S.; Sterenborg, H. J.; Kerrebijn, J. D.; Van Driel, P. B.; Baatenburg de Jong, R. J.; Lowik, C. W., Image-guided surgery in head and neck cancer: current practice and future directions of optical imaging. *Head Neck* **2012,** *34* (1), 120-6.

216. Refaat, A.; Yap, M. L.; Pietersz, G.; Walsh, A. P. G.; Zeller, J.; Del Rosal, B.; Wang, X.; Peter, K., In vivo fluorescence imaging: success in preclinical imaging paves the way for clinical applications. *J Nanobiotechnology* **2022,** *20* (1), 450.

217. Jo Bsis-Vandervliet, F. F., Discovery of the near-infrared window into the body and the early development of near-infrared spectroscopy. *J Biomed Opt* **1999,** *4* (4), 392-6.

218. Weissleder, R., A clearer vision for in vivo imaging. *Nat Biotechnol* **2001,** *19* (4), 316-317.

219. Hang, Y. J.; Boryczka, J.; Wu, N. Q., Visible-light and near-infrared fluorescence and surface-enhanced Raman scattering point-of-care sensing and bio-imaging: a review. *Chem Soc Rev* **2022,** *51* (1), 329-375.

220. Desmettre, T.; Devoisselle, J. M.; Mordon, S., Fluorescence properties and metabolic features of indocyanine green (ICG) as related to angiography. *Surv Ophthalmol* **2000,** *45* (1), 15-27.

221. Vos, J. J.; Wietasch, J. K.; Absalom, A. R.; Hendriks, H. G.; Scheeren, T. W., Green light for liver function monitoring using indocyanine green? An overview of current clinical applications. *Anaesthesia* **2014,** *69* (12), 1364-76.

222. Qi, C.; Zhang, H.; Chen, Y.; Su, S.; Wang, X.; Huang, X.; Fang, C.; Li, B.; Xia, X.; He, P., Effectiveness and safety of indocyanine green fluorescence imaging-guided hepatectomy for liver tumors: A systematic review and first meta-analysis. *Photodiagnosis Photodyn Ther* **2019,** *28*, 346-353.

223. Marino, M. V.; Podda, M.; Fernandez, C. C.; Ruiz, M. G.; Fleitas, M. G., The application of indocyanine green-fluorescence imaging during robotic-assisted liver resection for malignant tumors: a single-arm feasibility cohort study. *HPB (Oxford)* **2020,** *22* (3), 422-431.

224. Philip, R.; Penzkofer, A.; Baumler, W.; Szeimies, R. M.; Abels, C., Absorption and fluorescence spectroscopic investigation of indocyanine green. *J Photoch Photobio A* **1996,** *96* (1-3), 137-148.

225. Kirchherr, A. K.; Briel, A.; Mader, K., Stabilization of Indocyanine Green by Encapsulation within Micellar Systems. *Mol Pharmaceut* **2009,** *6* (2), 480-491.

226. Ding, F.; Zhan, Y.; Lu, X.; Sun, Y., Recent advances in near-infrared II fluorophores for multifunctional biomedical imaging. *Chem Sci* **2018,** *9* (19), 4370-4380.

227. Jiao, M. X.; Portniagin, A. S.; Luo, X. L.; Jing, L. H.; Han, B. X.; Rogach, A. L., Semiconductor Nanocrystals Emitting in the Second Near-Infrared Window: Optical Properties and Application in Biomedical Imaging. *Adv Opt Mater* **2022,** *10* (14).

228. Medeiros, N. G.; Braga, C. A.; Camara, V. S.; Duarte, R. C.; Rodembusch, F. S., Near-Infrared Fluorophores Based on Heptamethine Cyanine Dyes: From Their Synthesis and Photophysical Properties to Recent Optical Sensing and Bioimaging Applications. *Asian J Org Chem* **2022,** *11* (6).

229. Liu, H.; Yin, J. J.; Xing, E. Y.; Du, Y. Y.; Su, Y.; Feng, Y. Q.; Meng, S. X., Halogenated cyanine dyes for synergistic photodynamic and photothermal therapy. *Dyes Pigments* **2021,** *190*.

230. Guerrero, Y.; Singh, S. P.; Mai, T.; Murali, R. K.; Tanikella, L.; Zahedi, A.; Kundra, V.; Anvari, B., Optical Characteristics and Tumor Imaging Capabilities of Near Infrared Dyes in Free and Nano-Encapsulated Formulations Comprised of Viral Capsids. *ACS Appl Mater Interfaces* **2017,** *9* (23), 19601-19611.

231. Kirchin, M. A.; Pirovano, G. P.; Spinazzi, A., Gadobenate dimeglumine (Gd-BOPTA). An overview. *Invest Radiol* **1998,** *33* (11), 798-809.

232. Chavhan, G. B.; Mann, E.; Kamath, B. M.; Babyn, P. S., Gadobenate-dimeglumine-enhanced magnetic resonance imaging for hepatic lesions in children. *Pediatr Radiol* **2014,** *44* (10), 1266-74.

233. Knopp, M. V.; Runge, V. M.; Essig, M.; Hartman, M.; Jansen, O.; Kirchin, M. A.; Moeller, A.; Seeberg, A. H.; Lodemann, K. P., Primary and secondary brain tumors at MR imaging: Bicentric intraindividual crossover comparison of gadobenate dimeglumine and gadopentetate dimeglumine. *Radiology* **2004,** *230* (1), 55-64.

234. Clauser, P.; Helbich, T. H.; Kapetas, P.; Pinker, K.; Bernathova, M.; Woitek, R.; Kaneider, A.; Baltzer, P. A. T., Breast lesion detection and characterization with contrast-enhanced magnetic resonance imaging: Prospective randomized intraindividual comparison of gadoterate meglumine (0.15 mmol/kg) and gadobenate dimeglumine (0.075 mmol/kg) at 3T. *J Magn Reson Imaging* **2019,** *49* (4), 1157-1165.

235. Essig, M., Gadobenate dimeglumine (MultiHance) in MR imaging of the CNS: studies to assess the benefits of a high relaxivity contrast agent. *Acad Radiol* **2005,** *12 Suppl 1*, S23-7.

236. Vankayala, R.; Bahena, E.; Guerrero, Y.; Singh, S. P.; Ravoori, M. K.; Kundra, V.; Anvari, B., Virus-Mimicking Nanoparticles for Targeted Near Infrared Fluorescence Imaging of Intraperitoneal Ovarian Tumors in Mice. *Ann Biomed Eng* **2021,** *49* (2), 548-559.

237. Zhang, M.; Du, Y.; Wang, S.; Chen, B., A Review of Biomimetic Nanoparticle Drug Delivery Systems Based on Cell Membranes. *Drug Des Devel Ther* **2020,** *14*, 5495-5503.

238. Guido, C.; Maiorano, G.; Gutierrez-Millan, C.; Cortese, B.; Trapani, A.; D'Amone, S.; Gigli, G.; Palama, I. E., Erythrocytes and Nanoparticles: New Therapeutic Systems. *Appl Sci-Basel* **2021,** *11* (5).

239. Jung, B. S.; Vullev, V. I.; Anvari, B., Revisiting Indocyanine Green: Effects of Serum and Physiological Temperature on Absorption and Fluorescence Characteristics. *Ieee J Sel Top Quant* **2014,** *20* (2).

240. Starosolski, Z.; Bhavane, R.; Ghaghada, K. B.; Vasudevan, S. A.; Kaay, A.; Annapragada, A., Indocyanine green fluorescence in second near-infrared (NIR-II) window. *PLoS One* **2017,** *12* (11), e0187563.

241. Yuan, B.; Chen, N.; Zhu, Q., Emission and absorption properties of indocyanine green in Intralipid solution. *J Biomed Opt* **2004,** *9* (3), 497-503.

242. Gerega, A.; Zolek, N.; Soltysinski, T.; Milej, D.; Sawosz, P.; Toczylowska, B.; Liebert, A., Wavelength-resolved measurements of fluorescence lifetime of indocyanine green. *J Biomed Opt* **2011,** *16* (6), 067010.

243. Shao, Y.; Zhang, X. L.; Liang, K.; Wang, J.; Lin, Y. J.; Yang, S. G.; Zhang, W. B.; Zhu, M. F.; Sun, B., How does the interplay between bromine substitution at bay area and bulky substituents at imide position influence the photophysical properties of perylene diimides? *Rsc Adv* **2017,** *7* (26), 16155-16162.

244. Whitaker, J. R.; Granum, P. E., An absolute method for protein determination based on difference in absorbance at 235 and 280 nm. *Anal Biochem* **1980,** *109* (1), 156-9.

245. Noble, J. E., Quantification of Protein Concentration Using UV Absorbance and Coomassie Dyes. *Method Enzymol* **2014,** *536*, 17-26.